Kaon Production near Zero Transverse Momentum in Relativistic Heavy Ion Collisions

A Dissertation Presented

by

Byungsik Hong

to

The Graduate School

in Partial Fulfillment of the

Requirements

for the Degree of

Doctor of Philosophy

in

Physics

State University of New York

at Stony Brook

May 1995

State University of New York
at Stony Brook

The Graduate School

Byungsik Hong

We, the dissertation committee for the above candidate for the Doctor of Philosophy degree, hereby recommend acceptance of this dissertation.

Peter Braun-Munzinger
Professor of Physics

Gerald E. Brown
Professor of Physics

Michael Rijssenbeek
Professor of Physics

Edward O'Brien
Physicist, Brookhaven National Laboratory

This dissertation is accepted by the Graduate School.

Graduate School

Abstract of the Dissertation

Kaon Production near Zero Transverse Momentum in Relativistic Heavy Ion Collisions

by

Byungsik Hong

Doctor of Philosophy

in

Physics

State University of New York

at Stony Brook

1995

The forward spectrometer of experiment E814/E877 at the Brookhaven National Laboratory Alternate Gradient Synchrotron is well suited to measure transverse momentum spectra of produced particles down to zero transverse momentum. In addition to containing information on resonance decays, such spectra may also exhibit features due to collective potentials and density dependent masses.

To search for such effects, we have measured transverse momentum spec-

tra for central 14.6 A GeV ^{28}Si + Pb and 10.8 A GeV ^{197}Au + Au collisions. The analysis shows a steep increase near zero transverse momentum above the Boltzmann thermal distribution plus possible decay contribution for kaons in ^{28}Si + Pb collisions, although measured only with a small acceptance. The results for ^{197}Au + Au collisions, taken with much higher resolution and over a larger acceptance in transverse momentum, also shows a steep increase near zero transverse momentum. However, positively charged kaons show a hole at zero transverse momentum, while the negatively charged kaons show a continuous rise to zero transverse momentum within the present statistical errors. The pion spectra seem to show a similar effect.

We discuss the detailed analysis procedure and the implications of this data on the presence of collective effects during the high compression phase of the collision.

To My Wife, Heesuk,

for her love

Contents

List of Figures

List of Tables

Acknowledgements

First of all, I am grateful to Prof. Peter Braun-Munzinger, my thesis advisor, for leading me to this point. His advice and patience have been essential to complete this thesis. I have also been inspired very much by his understanding of physics as well as his way of guiding student in general.

Many of my special thanks go to Profs. Johanna Stachel and Thomas Hemmick for their encouragement and help, which were indispensable for this analysis.

I am grateful to Dr. Nu Xu for his stimulation. He encouraged me in the "oriental" way, which we could share easily. I have sometimes been relieved, and obtained strength to continue my job from his comments.

There are several friends of mine I wish to remember and make a record of here. Yingchao Zhang deserves my sincere gratitude. His kind introduction to the nuclear flow phenomenon has broaden my eyes into a different world of physics. All the discussions we had throughout our time at Stony Brook will be remembered as a joy. James Dee and Chuanming Zou also deserve many thanks for their work on the operation of the UNIX system and on RQMD respectively. All of us started our graduate studies about the same time and

I believe the parallels between us was great advantage for learning.

During my first hardware experience, I was indebted to Dr. Craig Woody, Sergey Panitkin and Dr. Moorthy Muthuswamy for their help in running beam telescope for the 1992 run. I have learned not only the beam logic, but also much of the electronics operation.

It was my cherished experience to have built the UV focal plane detector with Prof. Thomas Hemmick and Dr. Nu Xu in the fall of 1992. It was a part of R&D for a Ring Imaging Čerencov detector for the PHENIX collaboration in the Relativistic Heavy Ion Collider, BNL. I would like to thank them again.

I am grateful to Dr. Johannes Wessels, who spent the whole summer of 1993 with me in the cavern, the winding room at BNL, to build four MWPCs for the E877 collaboration.

I learned about the Monte - Carlo simulation technique using GEANT from Dr. Rene Bellwied in my early research time. His kind instruction was warm enough for me to be attracted to the field.

Dr. Gabor David was the first one who introduced me the data analysis program, STEP1. I am also indebted to him for his teaching about the FORTRAN and VAX system.

I am grateful to the collaborators at McGill University, Dr. Jean Barrette, Dr. Claude Pruneau, Dr. Marzia Rosati, Roger Lacasse and Gang Wang. They were in charge of the upstream time of flight wall for the 1992 and 1993 run. Without their deliberate efforts to install the detector in its place in time, it would have been much more difficult for me to finish this data analysis now.

My list of acknowledgement would not be completed without mentioning the following people in the collaboration: Dr. Simon Bennett, Wen-Chen Chang, Dr. Wilfred Cleland, Dr. Thomas Comier, Dr. Olacio Dietzsch, Gami Dadusc, Dr. Dan Fox, Dr. Joseph Germani, Sylvain Gilbert, Dr. Vicky Greene, Dr. Jerry Hall, Dr. Norbert Hermann, Richard Hutter, Dr. Kithiri Jayananda, Steve Johnson, Dr. David Kraus, Youngil Kwon, Dr. Shiva Kumar, Dr. David Lissauer, Dr. William Llope, Dr. Thomas Ludlam, Dr. Richard Majka, Dr. Tommy Mark, Rinarto Matheus, Dr. Sean McCorkle, Dr. Dariusz Miskowiec, Dr. Jeffrey Mitchell, Dr. Ed O'Brien, Timothy Piazza, Mark Pollack, Dr. Modula Rao, Dr. Frank Rotondo, Dr. Sergey Sedykh, Dr. Nelson daSilva, Dr. Johanne Simon-Gillo, Dr. Upul Sonnadara, Dr. Helio Takai, Dr. Marzia Takagui, Dr. Tom Throwe, Dr. Sergey Voloshin, Thongbay Vongpaseuth, Dr. Zhengzhi Zhang. Without all these people, a successful experiment would never be possible. Especially I am indebted to Tim Piazza, who corrected my incomplete English deliberately. Thank you all.

I am deeply grateful to my parents and sister, Byunghye, for their long-standing encouragement and love. I am also indebted to my mother-in-law who has taken care of my son, Jilly, during my study. I had only about half a year to take care of Jilly during my whole graduate term. I hope I can make up for this deficient role as a father later.

Finally, the deepest gratitude of mine should go to my wife, Heesuk. No word can express my appreciation and love to her. I hope I recompense her for her suffering due to my study in the near future.

Chapter 1

Introduction

1.1 Overview of Relativistic Heavy Ion Collisions

The elementary particles of the strong interaction, the quarks and gluons, are confined inside bags which balance the vacuum pressure outside, and form the hadrons [1, 2]. The effective interaction length among the constituents confines this bag size to about 1 fm radius. The quarks interact perturbatively with each other in the confining bag (asymptotic freedom) via an intermediating gauge boson, the gluon. The strength of interaction increases linearly as a function of the separation between the constituent quarks. If the quarks are pulled a sufficient distance apart, the energy stored in the field string will create a quark - antiquark pair. Because each of the created particles will form a bound state (bag) with one of the original quarks, it is impossible to make a quark free [3]. This confinement and asymptotic freedom characterize the fundamental aspects of the present standard theory of strong interactions, so called Quantum ChromoDynamics (QCD).

However, it is expected that a phase transition from normal nuclear matter to deconfined quark matter will take place at sufficiently high temperature and/or high baryon density [4, 5]. Beyond such a phase transition, the quarks in the matter can move freely over a large distance, and are no longer confined within individual hadrons. Since their perturbative interaction is via color charge, we call this state a quark gluon plasma (QGP) . We may try to understand the nuclear phase transition in terms of a bag model [6]. At high temperature or energy density, many hadrons, mostly pions, are formed and they effectively coalesce. These many hadron bags[1] are squeezed together and the valence quarks and antiquarks can hop across from one bag to another. A given quark will not experience any significant force from the other quarks far away from it due to the screening of the nearer quarks. On the other hand the nearby quarks are very close and produce a weak force due to the asymptotic freedom. Therefore the quarks are subjected to only a weak force and they can move almost freely; in this case we expect the QGP is formed.

In order to calculate the equation of state properly, we have to use the quark and gluon interactions of the QCD Lagrangian. However for the large scale distance regime, for which perturbation theory is not valid anymore, we presently have only one calculational method, namely lattice Quantum ChromoDynamics (LQCD) [7]. In this lattice gauge theory, one integrates the Lagrangian with a finite spacing l between points in space - time coordinates,

[1]There would be many baryon bags, considering high baryon number density environment.

and then attempts to recover the continuum theory by extrapolating the results for $l \to 0$. Since space-time has infinite volume, one ought to take, in principle, infinite number of lattice points, which requires infinite computing power. The results of lattice calculations, including only gluons, has shown that there is something close to a first order phase transition around the critical temperature of 200 MeV [8]. However more detailed studies including the low mass quark degrees of freedom, up and down, in addition to gluons have shown the transition is not simply first order, but is rather complicated [9, 10, 11].

The prediction of the QGP state is also of prime importance for astrophysics [12]. According to the Big Bang theory, the early universe was a dense ($\epsilon \geq 2.5$ GeV/fm^3) and hot ($T \geq 200$ MeV) plasma matter with deconfined quarks and gluons for the first $\sim 10^{-6}$ sec. After that period the energy density decreased, the plasma cooled and elementary constituents condensed into confined and colorless hadrons (hadronization) during the cosmological expansion.

The purpose of relativistic heavy ion experiments at Brookhaven National Laboratory's (BNL) Alternate Gradient Synchrotron (AGS) with 14.6 A GeV ^{28}Si and 10.8 A GeV ^{197}Au beams, and at CERN Super Proton Synchrotron (SPS) with 200 A GeV ^{32}S and 160 A GeV ^{82}Pb beams, and at, the currently under construction, Relativistic Heavy Ion Collider (RHIC) with 100 A GeV ^{197}Au beam, where A is the atomic number of ions, is to search for any signature of such an exotic state of matter in the laboratory.

The phase diagram of Fig. 1.1 represents the present understanding of the nuclear state as a function of temperature and baryon density. The proton rapidity distributions and transverse momentum spectra for 14.6 A GeV ^{28}Si + Al collisions show evidence of full stopping and the ensuing collective expansion [13, 14, 15]. This implies that we have already achieved a high baryon density state in such a light colliding system. The data from hadron transverse momentum spectra certainly show the collective behavior, *i.e.*, the temperature is higher for the heavier particles. Pion and delta resonance analysis show the temperature at freeze out is about 140 MeV at the AGS [16, 17]. From the above knowledge, we can expect the current AGS and SPS experiments would experience various medium effects due to high density and a possible deconfined state.

Another possible path to reach the phase transition, which will occure in the future RHIC experiments, may be considered at high temperature and low baryon density. The big bang in early universe is hoped to be described by future RHIC experiments.

1.2 Low Transverse Momentum Enhancement

Since there is a high probability of achieving high nuclear stopping power at AGS energies, it has been hoped to probe this high density state. Questions such as the medium effects on the masses of the hadrons, the widths of the masses and the branching ratios, etc. , at these high densities and/or temperatures have been studied extensively. The low transverse momentum (p_t) region of hadron spectra would be the best place to probe such a medium

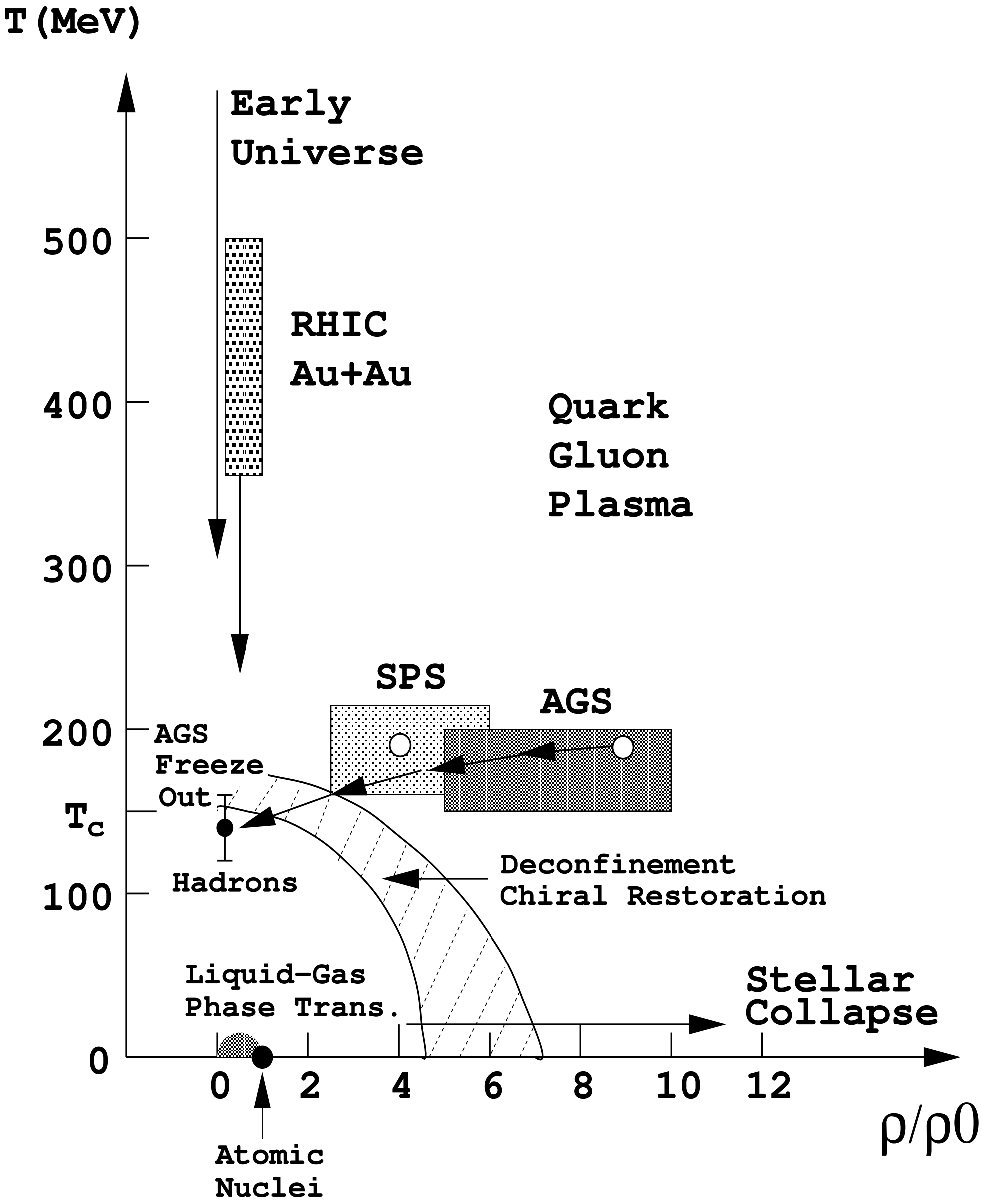

Figure 1.1: The current understanding of nuclear matter in the phase diagram, temperature (T) vs. baryon density (ρ) in the unit of normal nuclear matter density ($\rho_0 \sim 0.17/\mathrm{fm}^3$).

modification experimentally, as will be made clear below.

The restoration of chiral symmetry is one of the proposed characteristic. However for the effects on hadron masses, different methods make different predictions for the mass shifts [18][2]. Lattice QCD may help to resolve this problem in the future [9, 25].

Recently charged kaon condensation was driven primarily by symmetry breaking terms including the strange quark mass in the Hamiltonian [26, 27, 28, 29]. These studies showed a substantial amount of strange quark - anti-quark pair condensates when nuclear matter is compressed to $\rho \approx 2.5\rho_0$. As a consequence of the condensation, the explicitly broken chiral symmetry in QCD vacuum starts to disappear. If we further increase the matter density, the matter finally face the phase transition to the deconfined QGP state. However it is not yet clear how these condensations affect the hadronization of the fireball, and how we can connect this to experimental measurement.

[2]One example is a general scaling of all hadron masses. According to Brown et al. [19, 20, 21], the effective hadron masses at finite temperature (T) and baryon density (ρ_N) can be described by

$$\frac{m(T,\rho_N)}{m(0,0)} \approx [1-(\frac{T}{T_c})]^{1/3}[1-\frac{\lambda}{2}(\frac{\rho_N}{\rho_0})],$$

where $\lambda \approx 0.4$ and T_c is the critical temperature. The above parameterized mass formula indicates hadron masses decrease with increasing temperature [22] and nuclear matter density [23] and may vanish when the chiral symmetry is restored. Recent studies by Ko et al. [20, 21, 24] showed the kaon spectra from the AGS experiment (E802 collaboration) had been well reproduced by the model, including in - medium mass reduction, down to 0.2 GeV in p_t.

There were attempts to explain hadron p_t spectra in relativistic heavy ion collisions from the different physics points of view. Lee and Heinz [30, 31] introduced the collective flow model for fitting particle p_t spectra. They assumed a local Boltzmann thermal distribution of the fireball with global collective expansion velocity radially. Different decoupling positions for several hadron species, depending on their mass, result in not only different slope parameters but also the overall concave shape of the spectra. However, this model may overestimate the transverse flow effect by starting with isotropic expansion, which is not true for the AGS energy, since the flow should be mainly longitudinal as the initial pressure gradient is dominant along the beam axis due to the Lorentz contraction. Furthermore the low p_t component ($p_t \leq$ 0.2 GeV) of hadron data at CERN energies could not be reproduced by such a macroscopic model.

Another significant effort to generate low p_t enhancement was undertaken by Shuryak, considering a pion collective potential induced by the strong interaction [32, 33]. Since the pion dispersion equation is changed in the dense medium, pions with momentum less than a critical value, p_c, have less energy than free pion mass and are trapped in the fireball. They have to wait until the system cools and the magnitude of potential decreases. On the other hand pions with momentum greater than p_c can leave the fireball only if they hit the bag boundary inside a certain cone so that p_t is large enough to escape. As the system stays for a while at such a temperature, a significant fraction of pions are trapped by the collective potential. Collective potential study has been done for kaons as well [34]. These results showed only K^- with kinetic energy less than 20 MeV to be affected by the strong collective potential.

These pure medium effects, however, are disturbed by resonance decay processes [16, 35, 36]. The baryonic resonances play a dominant role at the AGS energy, while the mesonic resonances are dominant at the SPS energy. It has been shown by the E814 collaboration that 30 to 40 % of all participating nucleons are in the $\Delta(1232)$ resonance at AGS energies [16, 17]. This implies that the observed $\pi^{\pm}$ p_t spectra contain a major contribution of daughter pions from resonance decays. The resulting particles from the resonance state cause low p_t enhancement [36, 37]. According to [36], the observed negative (mostly π^-) spectrum by the E810 collaboration [38] is well reproduced by adding about 34% of $\Delta(1232)$ to the primary thermal distribution with temperature 150 MeV. Sollfrank et al. [37] calculated the effects of the two and three body decay kinematics on the p_t spectrum. They showed that a higher number of daughter particles resulted in a steeper distribution at low p_t, and also that lighter particle spectra would be more affected by the resonance dacays. They concluded that the low p_t $\pi^{\pm}$ spectra were fully explained by resonance decay and there was no low p_t enhancement beyond that. This means we can not rely on, or at least it will be extremely difficult, $\pi^{\pm}$ measurement in order to look into the medium effects, although resonance physics in itself is very interesting. Therefore the next natural candidate for studying the medium effects would be $K^{\pm}$, since it has relatively high abundance and much less contributions from the resonance decay channel (only $K^{\star} \rightarrow K\pi$, $\phi \rightarrow K^+K^-$ would be important). The modified E814 (1992 run) and E877 experimental setups have the unique capability to investigate such effects in the $K^{\pm}$ spectra for the low p_t region ($p_t \leq 250$ MeV).

The rest of this thesis is dedicated to the verification of any possible medium effects in high density nuclear matter by analysis of the $K^{\pm}$ spectra. This thesis includes the detailed analysis procedure and results not only for ^{28}Si + Pb reactions at 14.6 A GeV taken during the spring of 1992, but also for ^{197}Au + Au reactions at 10.8 A GeV taken during the fall of 1993. Chapter 2 is the description of the experimental setup for the experiment E814/E877. Chapter 3 will explain the detailed procedure of the offline cuts and detector calibrations (Drift Chambers and Time of Flight). Chapter 4 will give a description how we select $K^{\pm}$, how we correct for the geometrical asymmetry of our setup, and how we subtract the background resulting from $\pi^{\pm}$ and proton contamination. In chapter 5 we will present the results of $K^{\pm}$ production from both ^{28}Si and ^{197}Au induced reactions. Conclusion will follow in chapter 6.

1.3 Commonly Used Physical Variables

The longitudinal (p_l) and transverse (p_t) momenta are defined as the momenta along and perpendicular to the incident beam respectively:

$$p_l = p \cdot \cos\theta \tag{1.1}$$

and

$$p_t = p \cdot \sin\theta, \tag{1.2}$$

where p is the momentum and θ is the polar angle with respect to the beam direction.

The longitudinal momentum is often replaced by the rapidity y defined as

$$y = \frac{1}{2}\ln(\frac{E + p_l}{E - p_l}), \tag{1.3}$$

where $E = \sqrt{p^2 + m^2}$ is the total energy of the particle, since it is an invariant under the Lorentz transformation to another frame along the beam direction. A Lorentz transformed rapidity y' is related to the rapidity y of the particle in a moving frame as

$$y' = y + y^\star, \tag{1.4}$$

where

$$y^\star = \frac{1}{2}\ln(\frac{1 + \beta}{1 - \beta}) \tag{1.5}$$

is the rapidity of the moving system with the speed of the inertial frame, β, so that the rapidity distribution is simply shifted by $y^\star$ and thus keeps its shape.

In the case, where the rest mass of the particle is negligible, the rapidity can be approximated by the pseudorapidity, η,

$$y \to \eta \equiv -\ln[\tan(\frac{\theta}{2})] \tag{1.6}$$

for the angle θ in the laboratory system.

For the particle production in high energy and nuclear physics we often use the invariant inclusive cross section, $E\frac{d^3\sigma}{dp^3}$, because $\frac{dp^3}{E}$ is an invariant quantity under Lorentz transformations. The invariant cross section can also be expressed in y and p_t according to

$$E\frac{d^3\sigma}{dp^3} = \frac{1}{\pi}\frac{d^3\sigma}{dy dp_t^2} = \frac{1}{2\pi p_t}\frac{d^2\sigma}{dy dp_t} = \frac{1}{2\pi m_t}\frac{d^2\sigma}{dy dm_t}, \tag{1.7}$$

where $m_t = \sqrt{p_t^2 + m^2}$ is so called transverse mass. In this thesis we will express all invariant spectra as a function of y, p_t, and m_t. We will also use the convention $\hbar = c = 1$.

The total energy and longitudinal momentum can be expressed in terms of rapidity and transverse mass as

$$E = m_t \cdot \cosh y \tag{1.8}$$

and

$$p_l = m_t \cdot \sinh y. \tag{1.9}$$

The total transverse energy, E_t, is another useful term to describe the centrality of event as well as the energy flow closely related to the energy density produced in the collision. It is defined as

$$E_t = \sum_i E_i \cdot \sin\theta_i, \tag{1.10}$$

where i is summed over all the detector channels and θ_i is the geometrical angle between the beam axis and the detector element.

Chapter 2

Experimental Setup

2.1 Experiment 814

Figure 2.1 shows the schematic view of the experiment 814. The beam particles are incident from the left, and encounter a set of beam counters and a pair of silicon microstrip vertex detectors. After the collision of the beam with the target, surrounded by the target calorimeter, the produced particles into the very forward angle, as well as the survived beam and the projectile fragments, pass through the hole of two multiplicity detectors and the participant calorimeter (or the collimator for the large open configuration). They will see the first drift chamber before the dipole magnet, two drift/pad chambers, two time of flight hodoscopes, and uranium calorimeter. Charged particles are identified by the measurements of their momentum and time of flight in the spectrometer. For the kaon analysis the upstream time of flight wall is only used, since about half of the kaons from the interaction ($p = 2 \sim 3$ GeV) would already have decayed on the way to reach the upstream wall.

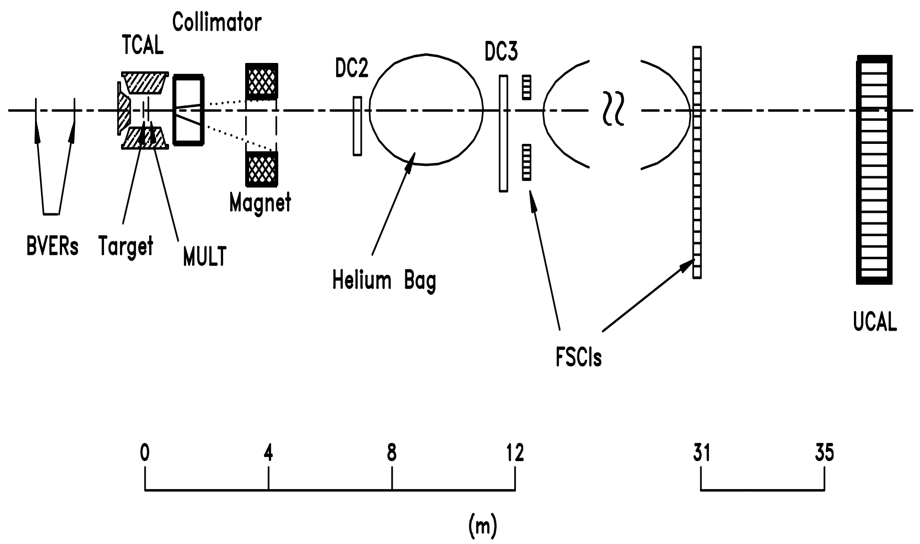

Figure 2.1: E814 experimental setup. According to the E814 reference frame, x is directed up, y points out of plane and z points to the right. The beam enters from left.

Particles emitted into large angles are detected by the target and participant calorimeters and the charged particle multiplicity detector.

The projectile for the 1992 run was 14.6 A GeV ^{28}Si ion and the target was approximately 2 mm thick (2.4 % of nuclear interaction length) natural Pb. The highest central trigger, corresponding to the upper 6 % of the geometrical cross section (200 mb) from the E_t distribution of the target calorimeter, was applied. Here the geometrical cross section of nuclear collision is defined by

$$\sigma_{geom} = \pi(R_p + R_t)^2 \tag{2.1}$$

where R_p and R_t are the radii of the projectile and target nuclei defined by $R = r_0 A^{1/3}$ with $r_0 = 1.2$ fm. The description of the major detectors in the E814 setup follows.

Beam Scintillator(BSCI) A series of scintillators before the target is used to define good beam and to provide a start signal of the time of flight measurement for the experiment. It consists of a pair of ellipsoidal scintillator disk, S2 and S4 (BC422), with two photomultiplier read outs for each, and another pair of veto counter, S1 and S3, with a circular hole at their centers and four photomultiplier read outs for each. The beam logic defines a good beam by requiring the coincidence of $\bar{S1} \cdot S2 \cdot \bar{S3} \cdot S4$.

The start of time of flight measurement is provided by the second photomultiplier of S4. The scintillators of S2 and S4 are tilted 45° with respect to the beam axis to improve the time resolution by receiving direct scintillating light. In order to fill the circular hole in the middle of veto detectors, the ellipsoidal shape has been chosen. The fast response photomultipliers have also been used: Hamamatsu R2083 which is 8 stage tube with 0.7 ns rise and 16 ns electron transit time for S4, and R2059 which is 12 stage tube with 1.3 ns rise and 28 ns elctron transit time for S2. Providing direct scintillating light and equalizing the pathlength of the beam + scintillating photons with this setup, the sigma of the time difference between two photomultipliers of S4 has been measured as 70 ps comparing to 100 ps for the perpendicular (not tilted) configuration to the beam axis. The positions and sizes of the four scintillators are described in Table 2.1 in detail.

Beam Vertex Detector(BVER) Two beam vertex detectors, located at z = -5.9 and -2.8 m respectively, determine the horizontal position of the beam to measure the incident angle. They are silicon strip detectors oriented

Counter	z	Thickness	O.D.	I.D.	L.D.	S.D.
S1	-652.8	0.4	15.0	1.5	—	—
S2	-627.4	0.05	—	—	2.6	1.8
S3	-177.8	0.4	15.0	0.6	—	—
S4	-203.2	0.05	—	—	1.3	0.9

Table 2.1: The positions and sizes of beam counters. O.D. means outer and I.D. means inner diameter of two veto counters. L.D. means longer and S.D. means shorter diameter of two ellipsoidal scintillators. All units are in cm.

vertically. The detectors are made of 300 μm thick silicon wafers and each detector consists of 320 strips with 50 μm spatial resolution in x. The multiple scattering dominated resolution is about 40 μrad in the incident beam angle and 50 μm in the x coordinate for ^{28}Si beam [14] and about 300μm for ^{197}Au beam.

Upstream Silicon Detector(UP-SILI) To eliminate the events with upstream interaction of the beam and improper charge states, an upstream silicon detector is placed at z = -2.5 cm, right before the target, on the beam axis. It measures the charge of the traversing particles with an active area of 2 cm^2 and a sensitive depth of 87 μm.

Target Calorimeter(TCAL) The target calorimeter is an electromagnetic calorimeter consisting of 992 Sodium Iodide crystals doped with Thallium as the impurity activator (NaI(Tl)) arranged in five walls surrounding the target. The crystals are positioned in an approximately projective geometry with the long axis of each one pointing at the target, confining the energy deposition from a single particle to minimal number of crystals and making the location of a crystal with respect to the target well defined in terms of angle. Most of the crystals are 13.8 cm in depth, which corresponds to about 5.3 radiation lengths or 0.33 nuclear interaction lengths, and measures the energy flow in the backward hemisphere. Four side walls cover a polar angle range of $48° < \theta_{Lab} < 118°$ corresponding to a pseudorapidity coverage of $-0.5 < \eta < 0.8$, and the backwall covers $-2.5 < \eta < -1.2$. Signals from the detector elements are read out by photodiodes mounted on the back face of each crystal with pre and shaping amplifiers. It measures the transverse energy distribution from the central collisions and serves also as the second level centrality trigger (LeCroy 4300B FERA, Fast Encoding Readout, system). A more detailed configuration of the arrays as well as the procedures of testing, calibration and operation can be found elsewhere [39].

Target Paddles(TPAD) The target scintillators are made of 52 scintillator paddles lining the inside of the side walls of the target calorimeter. Each counter has a dimension of $0.64 \times 3.5 \times 49$ cm^3 plastic scintillators (BC400) and read out by EMI 9127B photomultipliers. The paddles measure the number of charged particles traversing and define an interaction at the first trigger level. They also serve as a shielding material of the target calorimeter from the delta electrons.

Multiplicity Detector(MULT) The charged particle multiplicity detector consists of two silicon pad detectors sitting at z = 3.4 (MULT1) and 8.2 cm (MULT2). Each pad detector is made from an identical silicon disk of 300 μm thick and approximately 38 mm in radius with an active area extending up to 34 mm. Each detector is divided into 512 pads. MULT1 is segmented into 8 concentric rings of 64 pads each and MULT2 is segmented into 12 concentric rings of from 16 to 64 pads. It covers the pseudorapidity interval $0.89 < \eta <$ 3.86. The read out electronics (LeCroy PCOS II system) only registers whether or not each individual pad recorded a signal above threshold (approximately half of the most probable energy loss of a minimum ionizing particle (mip) at the normal incidence, about 120 KeV for 300 μm thick silicon) for a given event. Adding to measure the spatial distribution of the charged particle multiplicity, the FERA (LeCroy 4300B) information of the multiplicity detector serves as the second level centrality trigger. For more detailed decription of detector and multiplicity distribution, see [40].

Participant Calorimeter(PCAL) The participant calorimeter is a Pb/ Fe/ Scintillator sampling calorimeter measuring energy flow into the forward angle region $1.0^\circ < \theta_{Lab} < 47.0^\circ$ corresponding to the pseudorapidity range $0.83 < \eta < 4.7$. It has a dimension of $\Delta r \times \Delta z = 83.8 \times 81.3$ cm^2. The upstream face of PCAL is placed at $z = 73.4$ cm and it is divided into two electromagnetic (EM1 and EM2) and two hadronic (HD1 and HD2) depth segments. Each of the two electromagnetic segments has 0.4 interaction (or 10 radiation) lengths in depth consisting of six lead absorber (1 cm thick each) alternating with scintillator (BC408) layers (0.3 cm thick each). The next 24 absorber/scintillator (KSTI 430) layers make up the first hadronic segment and the remaining 23 layers with one iron plate at the end constitute the second hadronic segment. Each of the hadronic segments is approximately 1.6 interaction (or 40 radiation) lengths in depth. Beginning with the first lead absorber, every sixth lead plate with 1 cm depth is replaced by an iron plate with 1.6 cm depth for the mechanical stability. Looking down on $x-y$ plane, PCAL consists of four identical movable quadrants designed to be close to the azimuthal symmetry. Each quadrant is divided into four azimuthal slices of

22.5°. Then each slice is divided into eight towers radially. Therefore each quadrant consists of 128 towers and total 512 towers for the whole setup.

To transmit light from the scintillator to the photomultiplier, wavelength shifting optical fibers are glued on the side edges of the scintillating plates. Within the tower the fibers from each depth segments are bundled and coupled to a photomultipler tube (EMI 9954A).

The hadronic energy resolution is $45\%/\sqrt{E(\mathrm{GeV})}$ and the electromagnetic energy resolution is $28\%/\sqrt{E(\mathrm{GeV})}$. An e/π ratio of 1.06 has been determined at the beam energy of 4.34 GeV and it varies at other beam energies [41, 42]. The detailed Monte - Carlo simulation of the detector response, which was a part of my responsibility in E814, is summarized in Appendix A.

Collimator(COLL) For the large acceptance configuration, a collimator was used instead of PCAL. The collimator is simply a stack of lead blocks shimmed with shaped iron pieces around the opening to cover $-115 < \theta_x < 14$ mrad and $-21 < \theta_y < 21$ mrad in the laboratory frame[1].

Drift Chamber(DRCH) DRCH system is formed by three drift chambers (DC1, DC2, and DC3). By measuring the time taken for the ionization electrons to arrive at the anode wire, the absolute perpendicular distance of the trajectory of the charged particle from the wire is determined, although the

[1] Unfortunately, the dipole magnet was placed in a wrong x position during the 1992 run. Therefore the acceptance of the E814 setup was $-47 < \theta_x < 14$ mrad, which was determined by the magnet instead of the collimator.

left and right ambiguity will be solved in the pattern recognition process.

The first chamber, DC1, is located between the PCAL/Collimator and magnet as a confirmation detector. DC1 consists of a single wire plane above a cathode pad plane. The wire plane consists of 18 μm diameter gold plated tungsten anode wires alternating with stainless steel field wires. The wires on DC1 lie in the x direction and the y position resolution is limited by the wire spacing (4 mm between sense wires). The induced charge on the cathode plane by electrons drifting to the wires above the pad plane, shared among several pads through resistive strips, determines x position of the charge cluster, x_{Clus}, as the centroid of the charge distribution:

$$x_{Clus} = \frac{x_L Q_L + x_C Q_C + x_R Q_R}{Q_L + Q_C + Q_R} \tag{2.2}$$

where x_C is the position of the central pad, x_L and x_R are for the adjacent left and right pads, and Q_C, Q_L, and Q_R are the measured charge in those pads, respectively.

DC2 and DC3 are very similar in design except for size. Both of them have six drift planes and one wire plane with a cathode pad. Each of the six drift planes consists of 18 μm gold plated tungsten anode wires and stainless steel field wires alternatively. The wire planes are separated by aluminized mylar cathodes and the position of the field and sense wires are staggered on alternate planes to facilitate the pattern recognition process. The wires in DC2 (DC3) lie parallel to the y direction with sense wire spacing 6 (12) mm. The cathode pad planes are chevron shaped. By measuring the relative amounts of induced charge shared by neighboring pads along the wire, the y position of the charged particle trajectory along the wire, y_{Clus} can be deduced:

$$y_{Clus} = \frac{y_T Q_T + y_C Q_C + y_B Q_B}{Q_T + Q_C + Q_B} \tag{2.3}$$

where all definitions are same as DC1 except y position. Three density regions have been introduced in the pad planes, and y position resolutions of DC2 (DC3) have been estimated as 2.3, 5.1 and 15.0 mm (4.3, 7.0 and 36.0 mm) for fine, medium and coarse regions respectively. The x position resolutions determined by the drift plane of DC2 and DC3 are approximately 250 and 300 μm each for minimum ionizing particles. The multiple scattering dominated momentum resolution was estimated as $\delta p/p \sim 3.6\%/\beta$ for ^{28}Si induced reactions[2], where β is the particle velocity relative to the speed of light [14, 15].

All three drift chambers are run with a flow of a gas mixture of 50 % Ar and 50 % Ethane at atmospheric pressure. This gas mixture gives a drift velocity about 51-53 μm/ns at the operating voltages. A slight amount of ethanol was added to the gas of DC1 as a quencher to reduce charge accumulation on the wires. This was done by bubbling the gas through a bottle of ethanol maintained at 0°C temperature. The calibration of drift chambers for the 1992 and 1993 run is explained in next chapter. More detailed description of the construction, charateristic features, and pattern recognition program are found in the references [43, 44, 45].

Time of Flight Upstream(TOFU) The upstream time of flight scintillator wall was installed to detect charged kaons, before they decay, for the 1992

[2]For ^{197}Au induced reactions, $\delta p/p \sim 2.0\%/\beta$.

run. It consists of 20 vertical plastic scintillator slats (BC404) from x = -130 to 70 cm at $z = 12$ m downstream of the target. Each slat has a dimension of $\Delta x \times \Delta y \times \Delta z = 10 \times 60 \times 1$ cm^3 read out by two photomultipliers at top and bottom ends through light guides. A typical time resolution for the minimum ionizing particle was about 227 ps on average. The detailed description of the gain and time calibrations will be the subject of the next chapter.

Forward Scintillator(FSCI) The forward scintillator hodoscope wall consists of 39 vertical plate scintillator slats (BC404) with dimensions $\Delta x \times \Delta y \times \Delta z = 10 \times 120 \times 1$ cm^3 read out on top and bottom ends with photomultipliers (EMI 9954B) through light guides. It is positioned at $z = 31$ m downstream from the target and covers from x = -294 to 101 cm. A typical time resolution of 350 ps for the minimum ionizing particles has obtained. FSCI is specially useful for the analysis of antiprotons, since the negative charged kaons will mostly decay and the background will be significantly reduced.

Uranium Calorimeter(UCAL) The uranium calorimeter positioned at 36 m downstream of the target is designed for measuring the total energy of a projectile fragments including neutrons. It consists of 20 U/Cu/Scintillator[3] modules horizontally and each module is segmented into 12 optically decoupled towers vertically. Each tower with a cross sectional dimension of $\Delta x \times \Delta y = 20 \times 10$ cm^2 has two separate wavelength shifter bars coupling to the photomultiplier (EMI 9905B). Longitudinally each module consists of 40

[3]Historically uranium was used to achieve $e/\pi \sim 1$, using the fission energy.

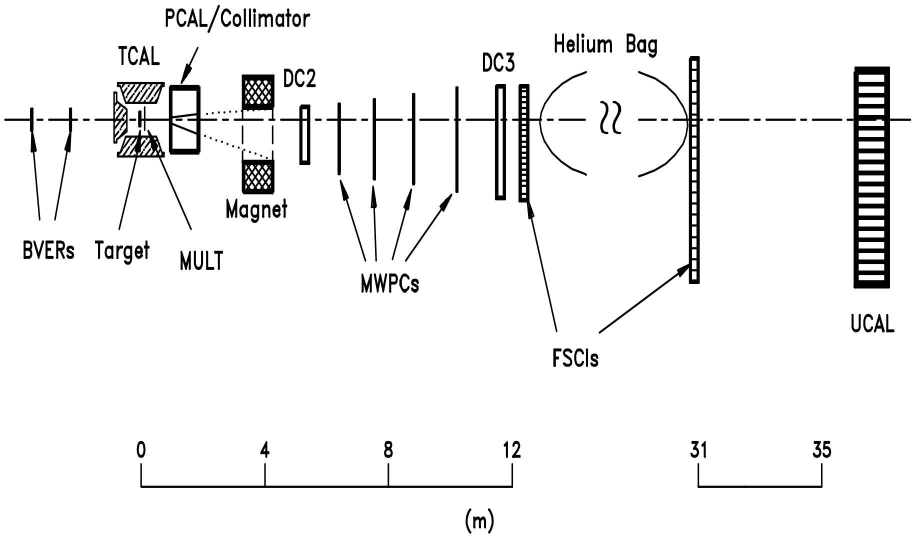

Figure 2.2: E877 experimental setup.

identical sections with one 0.5 cm Cu plate and two 3 cm uranium plates as an absorber alternating with 0.25 cm scintillators (PMMA). The total depth of a stack is 4.2 nuclear interaction lengths. The hadronic energy resolution of $57\%/\sqrt{E(\mathrm{GeV})}$ has been measured. The vertical and horizontal position resolutions for 12 GeV pion beam have been determined as 1.8 and 1.3 cm respectively [46].

2.2 Experiment 877

Figure 2.2 shows the E877 experimental setup for the 1993 run. There are two major changes compared to the E814 setup. One is the installation of four MWPCs between DC2 and DC3 in order to track about ten charged particles in the forward opening from the ^{197}Au induced reactions. Another major upgrade is to modify the upstream time of flight wall, aiming at much better time resolution to separate higher momentum particles, in addition to the much better spatial resolution.

For the 1993 run the projectile was 10.8 A GeV ^{197}Au ions[4], and the target was approximately 0.5 mm thick (1.9 % nuclear interaction lengths) natural Au. The explanation of the configuration for MWPC and new TOFU as well as the acceptance follows.

PCAL/COLL During the 1993 run, opening of top two quadrants of PCAL enabled us to manage to place a collimator inside the opening of PCAL. PCAL E_t measurement has been used for the second level centrality trigger. The collimator set the acceptance to $-134 < \theta_x < 16$ mrad and $-11 < \theta_y < 11$ mrad in the laboratory frame. Specifically, vertical acceptance has been reduced to restrict the number of charged particles in the spectrometer.

Multiwire Proportional Chamber(MWPC) The four multiwire proportional chambers are exactly same in design except for size. The 18 μm diameter gold plated tungsten wires lie along vertical direction with 5.08 mm spacing. MWPCs detect only whether or not there were particles passing through each chamber, with an x position resolution on the order of the wire spacing. Two aluminized mylar windows are accompanied at each side of wire plane supported by a G - 10 frame. The inner window is for high voltage cathode plane

[4]The beam momentum measurement of the ^{197}Au beam by using E877 spectrometer for the 1993 run is explained in Ref. [47].

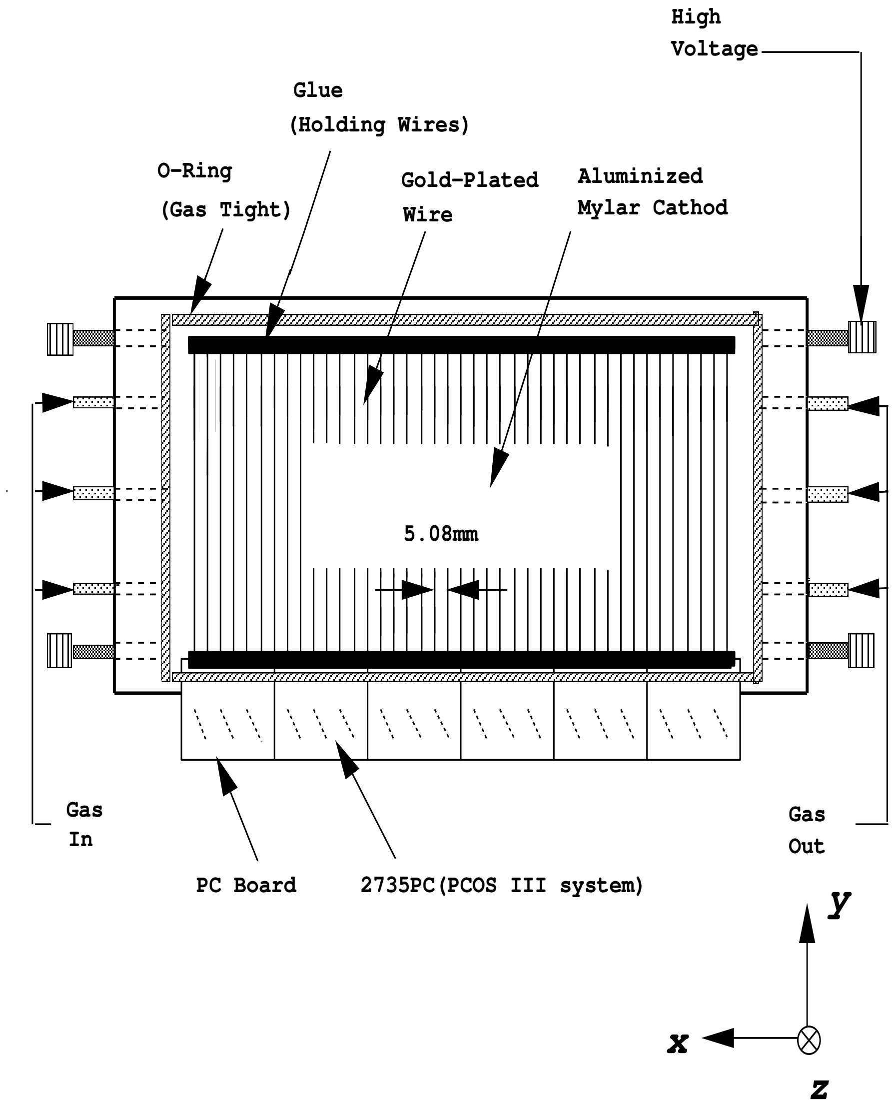

Figure 2.3: The front view of the wire body frame of MWPC.

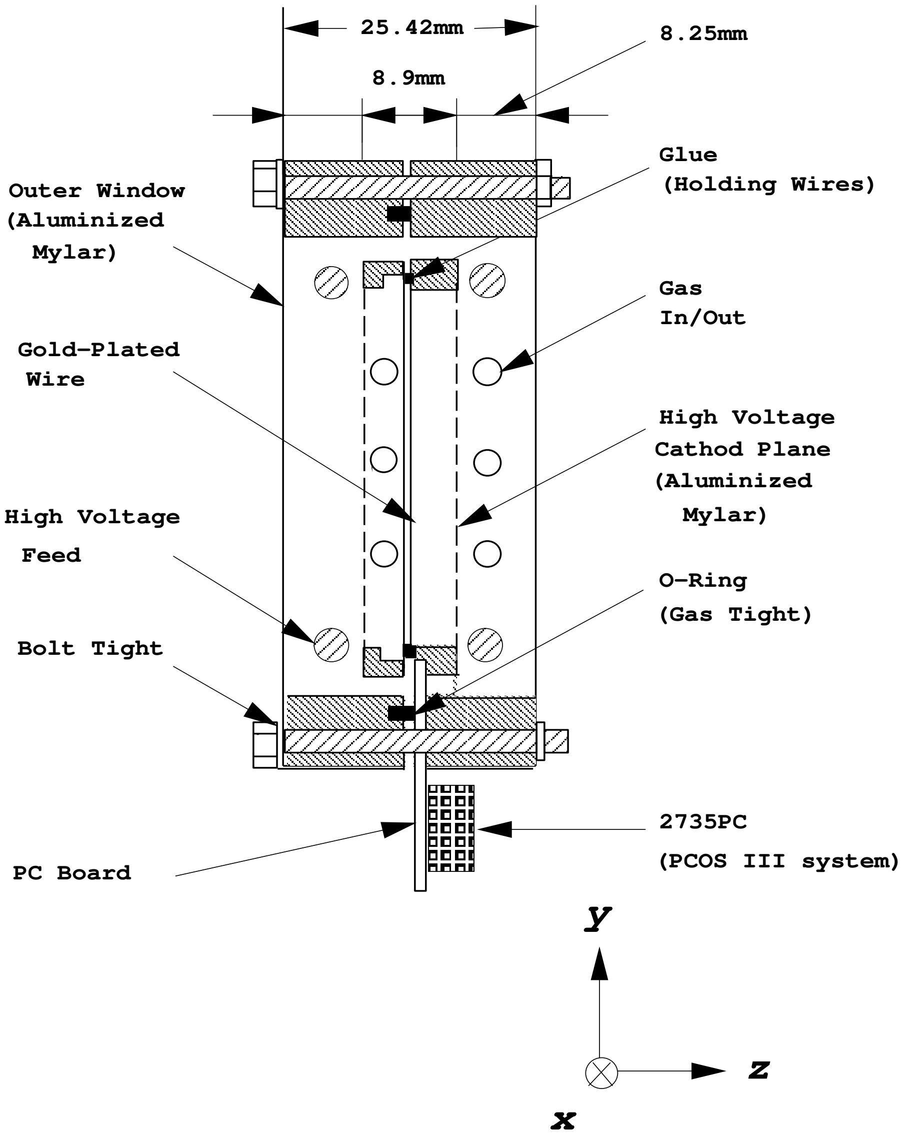

Figure 2.4: The side view of MWPC.

Chamber	z	x	Active Area		External Dimension	
			Width	Height	Width	Height
MWPC1	663.3	-80.8	110.2	33.0	143.3	66.0
MWPC2	784.1	-96.0	134.6	38.7	167.6	71.8
MWPC3	908.7	-111.3	159.0	44.5	192.0	77.5
MWPC4	1031.7	-126.5	183.4	50.2	216.4	83.2

Table 2.2: The summary of the position and size of four MWPCs. z position is measured from the target to the upstream face of chamber and x position is measured from the neutral line (z axis) to the first wire of chamber. All units are in cm.

and outer window for the mechanical enclosure of gas. The positions and sizes of each chamber are summarized in Table 2.2 [47]. The schematic front and side views of chamber are shown in Figs. 2.3 and 2.4 respectively.

During the construction the following points were emphasized:

- All inside cuts of G - 10 frame were glue sealed to prevent gas leakage.
- All glue seals were washed with acetone and alchol to remove any electrical conductivity through the glue surface.

- All G - 10 frames were baked by heat lamps for at least 24 hours each, to help to complete out - gasing chemical reactions.

- The electrical resistance across the inner cathode plane was checked and maintained within 10 % (High voltages are supplied from four corners of each cathode window to generate a more uniform electric field between the foil and wires).

- Wire tensions were maintained with 17.5 g·gravity (The maximum allowed tension on 18 μm diameter tungsten wire is approximately 23 g·gravity).

All tracking chambers including DC2 and DC3 were accompanied by the gas flow system with a gas mixture of 50 % Ar - 50 % Ethane at atmospheric pressure.

The signals produced by ionization electrons were read out by LeCroy PCOS III system [48]. PCOS III operating system includes 16 channel chamber-mounted amplifier/ discriminator card (2735PC), remote delay and latch module (2731A) with readout controller (2738) and CAMAC interface (4299). The block diagram for MWPC readout system is given in Fig. 2.5.

In order to avoid the high voltage break down of chamber due to the high charge of beam particles, we have disconnected the read out in the beam region and applied low voltage on those wires. The position of the beam trajectory at each chamber was detected at relatively low voltage, -1.4 kV. The beam position and deaden channels for different magnetic field settings during the 1993 run are summarized in Table 2.3 in terms of wire index.

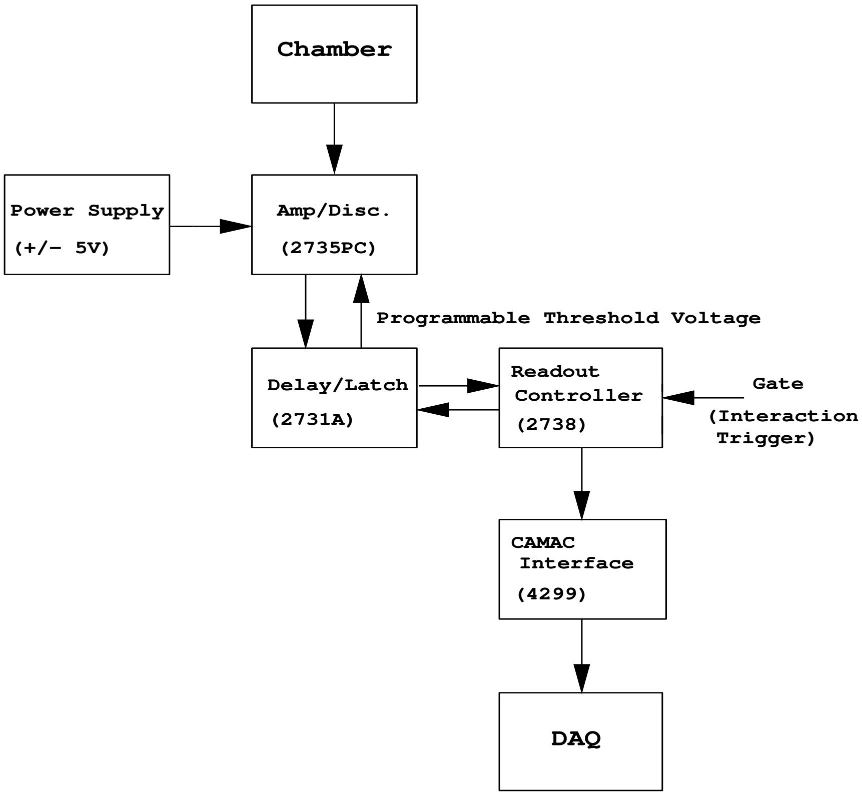

Figure 2.5: The block diagram of MWPC readout system (LeCroy PCOS III system).

Chamber	B(Tesla)		
	0	-0.262	0.262
MWPC1	157±3	160±3(154,166)	155±3(149,161)
MWPC2	188±4	190±4(184,196)	185±4(179,191)
MWPC3	217±4	221±4(215,228)	214±4(208,221)
MWPC4	247±5	252±5(246,259)	243±5(237,250)

Table 2.3: The measured x position of the beam trajectory and beam dead region (in the parenthesis) during the run at each chamber in terms of wire number for different magnetic field settings.

Applying approximately -2.2 kV on cathode plane of all MWPCs, we achieved an overall 97 % detection efficiency[5], requiring three out of four chambers, for the most central PCAL E_t trigger condition (about 10 % σ_{geom}).

Time of Flight Upstream(TOFU) The new high resolution upstream time of flight detector consists of 160 plastic scintillators (BC404) oriented vertically

[5]The determination of detection efficiency of each MWPC has been done by visual inspection of 500 ^{197}Au + Au events for PCAL high E_t trigger. The results are 99.1, 98.7, 99.4 and 99.0 % for MWPC1, MWPC2, MWPC3 and MWPC4 respectively.

at 12 m downstream. The signal is read out by photomultipliers (Hamamatsu R3478 or H5010 MOD assembly) at both ends. They cover from x = -159 to 78 cm. In general each counter has a squre shape cross sectional view on $x-z$ plane with 1.7 cm width and 0.25 mm overlap between neighboring counters. The 39 scintillators near the beam region (-21.0 cm $\leq x <$ 17 cm) have 1.0 cm width and 0.16 mm overlap for handling higher multiplicity around 0°. The detailed analysis for time calibration[6] has shown that overall 85 ps time resolution could be achievable.

[6]This work is done by collaborators at McGill University.

Chapter 3

Analysis I

3.1 Offline Cuts

The following analysis is only for the 1992 run.

3.1.1 Pedestal

Accurate analysis requires a good determination of the pedestal for each detector element. We have developed a technique to understand the systematic behavior of pedestal as a function of time [49]. Picking up empty events from an arbitrary "reference" run, we could compare all other runs to the reference, channel by channel, to find the average linear difference (y_{lin}),

$$y_{lin} \equiv \frac{1}{N_c}\sum_{i=1}^{N_c}[Ped_{ref}(i) - Ped_{cur}(i)], \tag{3.1}$$

root - mean - squre (rms) difference (y_{rms}),

$$y_{rms} \equiv \frac{1}{N_c^2}\sum_{i=1}^{N_c}[Ped_{ref}(i) - Ped_{cur}(i)]^2, \tag{3.2}$$

and maximum difference (y_{max}),

$$y_{max} \equiv max|Ped_{ref}(i) - Ped_{cur}(i)| \tag{3.3}$$

for $i = 1, 2, ..., N_c$. Here N_c is the total number of channels, $Ped_{ref}(i)$ is the mean of the ADC distribution of detector element i for the reference run and $Ped_{cur}(i)$ is that of the current run.

Figs. 3.1 and 3.2 show the above variables for Si data as a function of run number for two detectors, BSCI and TCAL. They clearly show there are two groups of pedestals for BSCI and three for TCAL. We can now pick any one of the runs for each group, and represent the whole group. We noticed that y_{max} of TCAL shows large deviation as a function of time. Specifically, 6 crystals (it became 9 crystals approaching to the end of the run) were problematic. However that number of crystals can be neglected for our further analysis, because their contribution to the total E_t is negligible ($\approx 0.1\%$ of maximum E_t for Pb target). Having done the pedestal adjustment, we could proceed to look at the individual detectors for several trigger conditions.

3.1.2 BSCI

The upstream interactions can be removed by looking at the pulse height of the veto detectors, S1 and S3. Figure 3.3 shows the sum of pulse heights for 4 PMTs at the beam and pre trigger conditions. The arrow represents the cut we applied to remove the upstream interactions.

For the beam and pre trigger events, the cuts on the pedestal of S2 and S4 were applied as shown in Fig. 3.4. We can also discard the double beam,

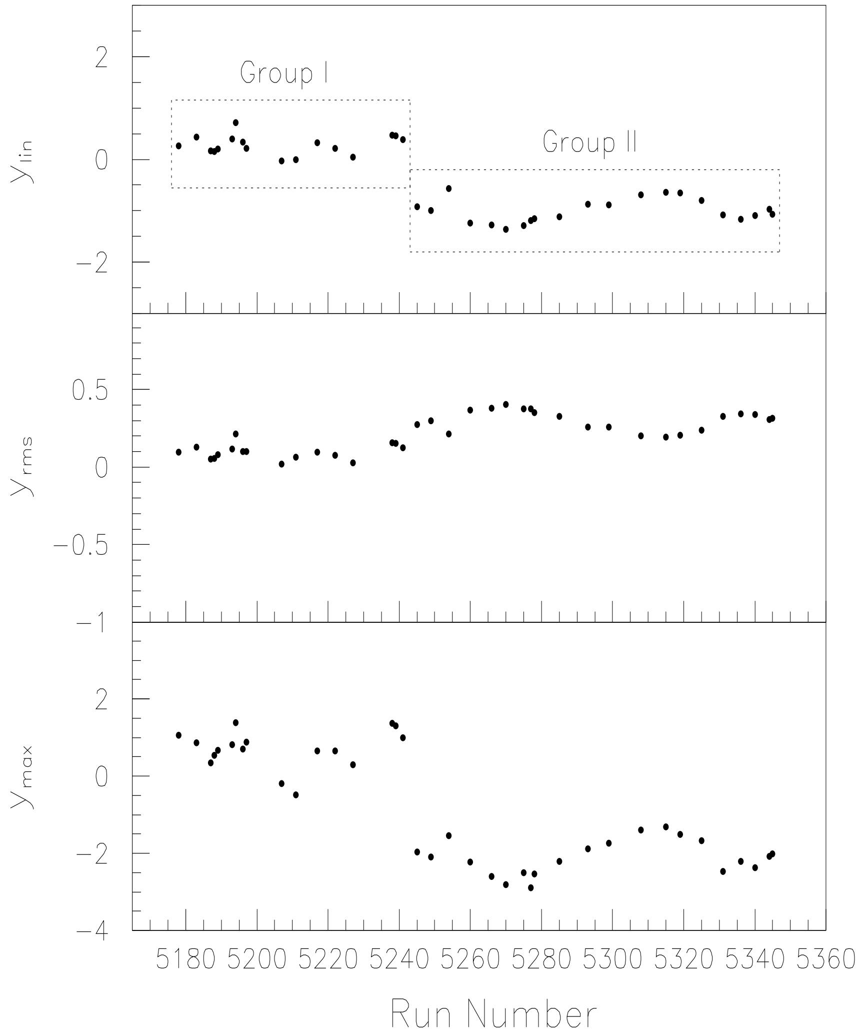

Figure 3.1: The averaged linear, rms, and maximum differences of the pedestal in channel for BSCI between the reference and the current run defined as in the text. The dotted boxes in the top figure represent two groups determined in this analysis.

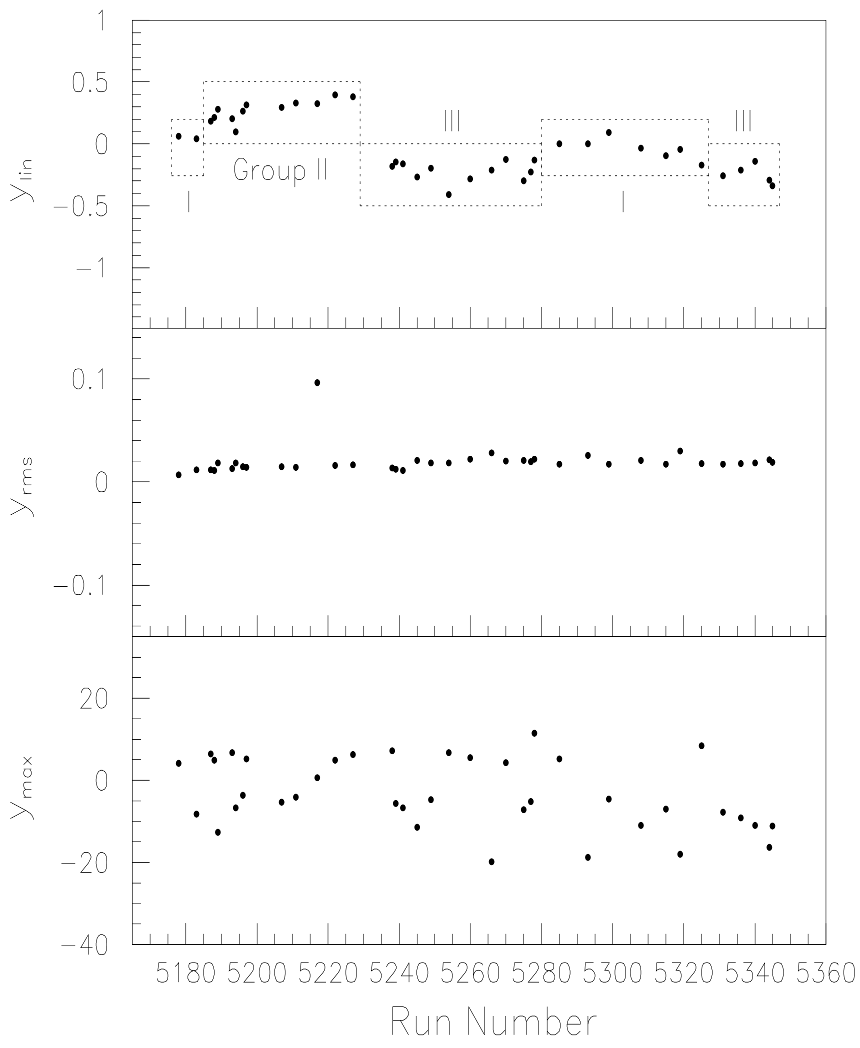

Figure 3.2: The averaged linear, rms, and maximum differences of the pedestal in channel for TCAL between the reference and the current run defined as in the text. The dotted boxes in the top figure represent three groups determined in this analysis.

two beam particles passing through the beam counter system within 20 ns, by looking at the pulse height sum of two PMTs of S2 and S4. Only the events for the pulse height sum between two arrows were taken. After applying all BSCI cut conditions, about 6 % of all the events were removed for the physics trigger conditions.

3.1.3 UP-SILI

From the pulse height information of the upstream silicon detector, sitting just upstream of the target, the events which have generated signal, not the beam, were excluded (Fig. 3.5). This cut rejects about 18 % of bad events from the physics trigger conditions.

3.1.4 TCAL and MULT

Another possible way to get rid of the upstream interaction is to use the correlation between TCAL E_t and multiplicity for the interaction trigger. Upstream interaction may generate abnormally high E_t in TCAL with very low multiplicity in MULT. These candidates were removed by excluding any events satisfying

$$E_t(\mathrm{GeV}) > 0.014 \times N_{FERA} - 4.0, \tag{3.4}$$

where N_{FERA} is the FERA output of MULT (Fig. 3.6). At the same time, the events with noisy multiplicity signal and low TCAL E_t were also removed by the condition:

$$E_t(\mathrm{GeV}) < 0.0072 \times N_{FERA} - 6.4 \tag{3.5}$$

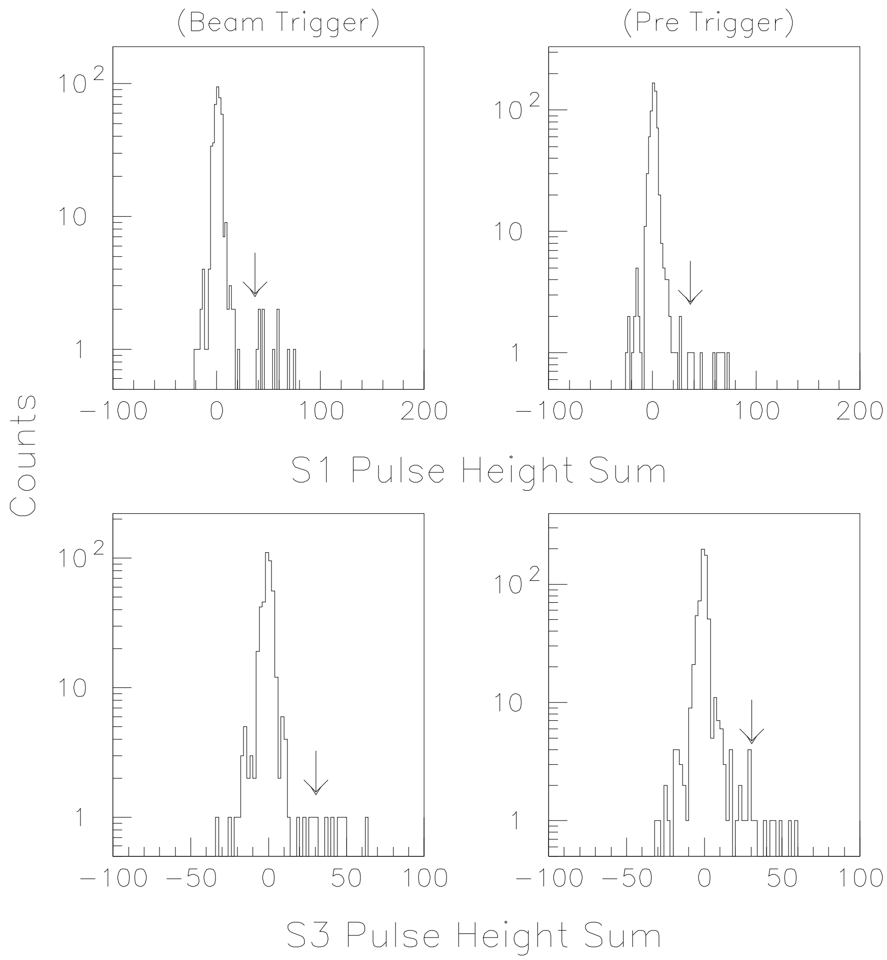

Figure 3.3: BSCI pulse height sum of two veto detectors, S1 (top) and S3 (bottom). Two trigger conditions of beam (left) and pre (right) have been applied. The arrows represent the cut we applied to get rid of the upstream interactions.

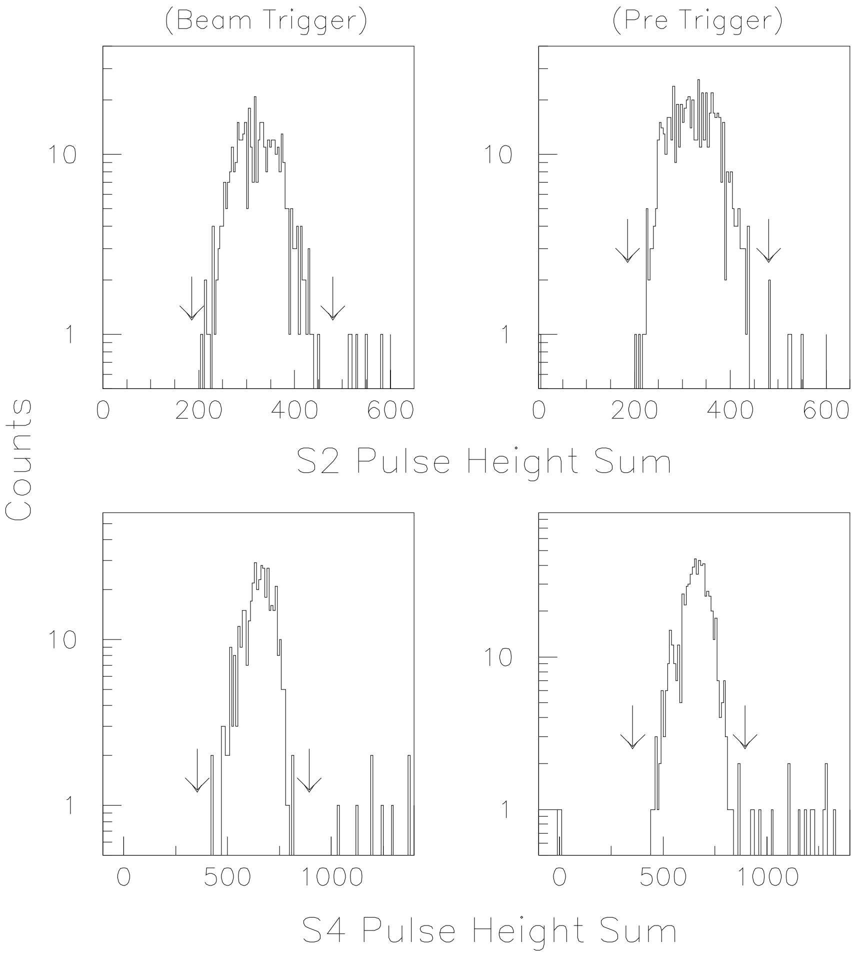

Figure 3.4: BSCI pulse height sum of two scintillators, S2 (top) and S4 (bottom). Two trigger conditions of beam (left) and pre (right) have been applied. The arrows represent the cut we applied to get rid of mostly the double beam.

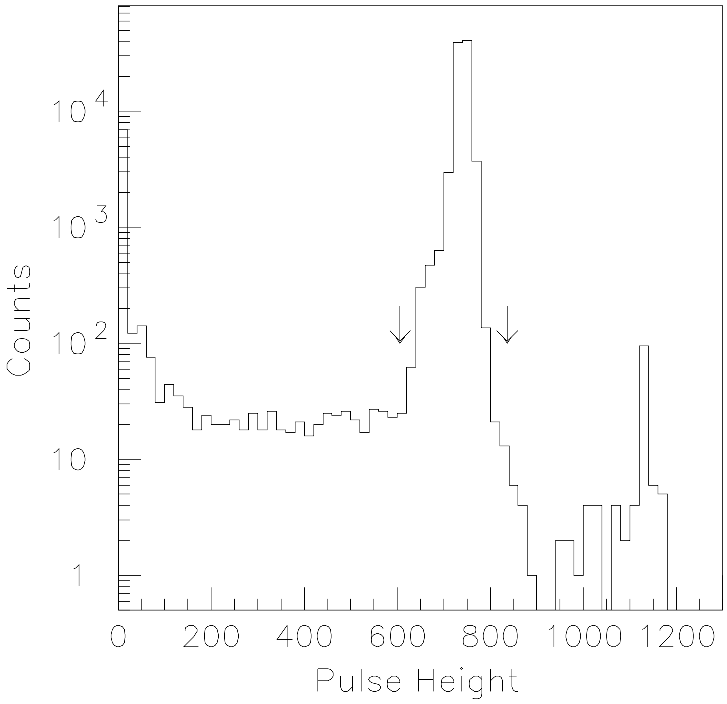

Figure 3.5: The pulse height information from the upstream silicon detector. The arrows represent the cut we applied to get rid of the upstream interaction and double beam, etc.

Cut Level	Trigger								
	32	34	35	64	65	66	69	82	84
BSCI	96.4	94.3	94.5	94.0	94.4	94.1	93.4	93.9	93.9
Up−Silicon	96.4	77.6	70.0	74.8	76.2	72.1	76.3	74.0	74.0
TCAL	96.4	77.6	66.4	74.3	76.1	72.1	75.8	73.6	73.6
MULT	95.6	76.4	66.2	73.9	75.6	71.4	75.7	73.1	73.1

Table 3.1: The fraction in % of the events survived after each offline cut level for several triggers in ^{28}Si + Pb reactions.

(Fig. 3.6). These requirements get rid of about 1.5 % of total events. The surviving probability of all events after each cut for the several trigger conditions are summarized in Table 3.1 with the trigger list in Table 3.2.

3.2 Drift Chamber Calibration

3.2.1 Time Offset(T_0)

Since the x position of the reconstructed track at each wire plane is determined by TDC (time) information and the measured drift velocity ($v_{DC2} =$

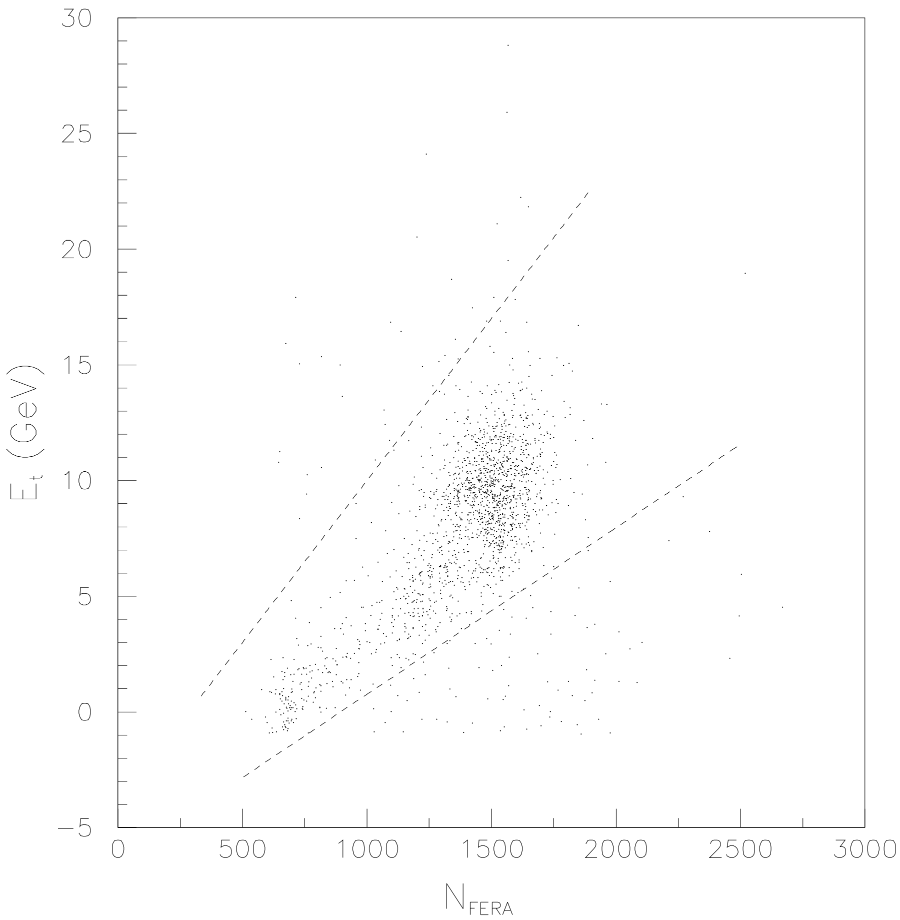

Figure 3.6: The correlation between TCAL E_t and the multiplicity from FERA, N_{FERA}, for the physics trigger. Two dashed lines correspond to the cut conditions for removing the upstream interaction (top) and the multiplicity noise (bottom).

Trigger	Meaning
32	Empty
34	Beam Downscaled
35	Pre Downscaled
64	Multiplicity Low Downscaled
65	Multiplicity Medium Downscaled
66	Multiplicity High
69	TCAL E_t High
82	Pre (MULT)
84	Pre (TPAD)

Table 3.2: Trigger List for the 1992 run.

53.8 μm/ns and $v_{DC3} = 51.2$ μm/ns), the time calibration of drift chamber is crucial for the pattern recognition. In order to determine the time offset, T_0, of the drift chamber, we employed an iterative procedure, in which we calculate the time difference determined from the difference in the measured x position (x_{Mea} using the default values of $T_{0,DC2} = 248$ ns and $T_{0,DC3} = 278$ ns in the 1992 run) and the linearly fitted x position (x_{Fit}) divided by the drift velocity,

$$\delta T_{0,DC2(DC3)} \equiv \frac{x_{Mea} - x_{Fit}}{v_{DC2(DC3)}}. \tag{3.6}$$

This procedure is repeated adjusting $T_{0,DC2}$ and $T_{0,DC3}$ until the difference δT_0 becomes minimal. Figure 3.7 shows $\delta T_{0,DC2(DC3)}$ using default T_0s (left pannel) and new values, $T_{0,DC2} = 244$ ns and $T_{0,DC3} = 272$ ns, (right pannel).

For the 1993 run, the same procedure is repeated and the modified time offsets of $T_{0,DC2} = 47$ ns and $T_{0,DC3} = 54$ ns have been determined starting from the default values of $T_{0,DC2} = 55$ ns and $T_{0,DC3} = 60$ ns [47].

3.2.2 Position Alignment

Another piece of essential information needed to operate the track reconstruction precisely is to find the exact position of each detector. In diagnosing surveyed x positions, a linear fit is done to the beam tracks for the two BVERs and three drift chambers with zero magnetic field and without a target. Under these conditions the beam particles make a straight track through the spectrometer. After selecting only the maximum charge clusters in the pad chambers, we calculated the position difference, δx, between the measured x position (x_{Mea}) and the linearly fitted x position (x_{Fit}) of x_{Mea} at the surveyed

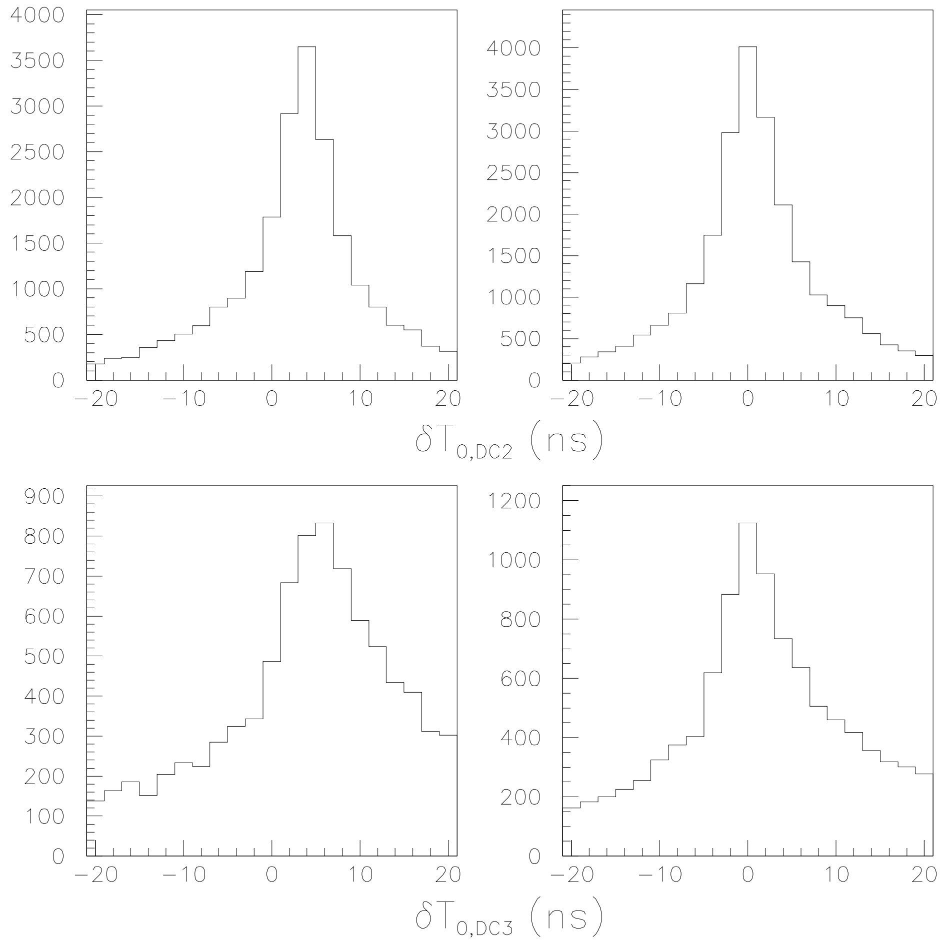

Figure 3.7: The δT_0 of DC2 (top) and DC3 (bottom) before (left) and after (right) the correction for the 1992 run.

z of each detector. The left column of Fig. 3.8 represents δx of two BVERs, DC1, DC2 and DC3 using only surveyed values, x_{Survey}, without any correction for the 1992 run. The resulting histograms, after an iterative procedure to shift all δx's to zero, applying correction offsets are shown in the right pannel of Fig. 3.8. The surveyed x positions and the determined correction factors are given in Table 3.3.

The same procedure is repeated for the 1993 run with the two BVERs, DC2 and DC3. High voltages of DC2 and DC3 were lowered to 900 and 1000 V respectively to have a clearer beam signal[1] and to avoid tails due to δ - electrons. Although the drift velocities remain the same for this voltage setting, since they are already in the saturation region [50], the time offsets of the two drift chambers have to be determined again. Applying the same procedure for T_0s explained in the previous section, $T_{0,DC2}$ = 36 ns and $T_{0,DC3}$ = 43 ns have been obtained. The correction factors of the x position of each detector for the 1993 run are also summarized in Table 3.3 [47].

3.2.3 DC1 Confirmation

The first drift chamber, positioned right before the magnet, was used as a confirmation detector to verify all tracks reconstructed downstream after the magnet. DC1 confirmation may help to get rid of any tracks not being connected with DC1 cluster. These tracks are considered wrong, since DC1

[1]Typical high voltages applyed to DC2 and DC3 are above 1500 V. However these can not be used for the highly charged particles like $^{197}_{79}$Au.

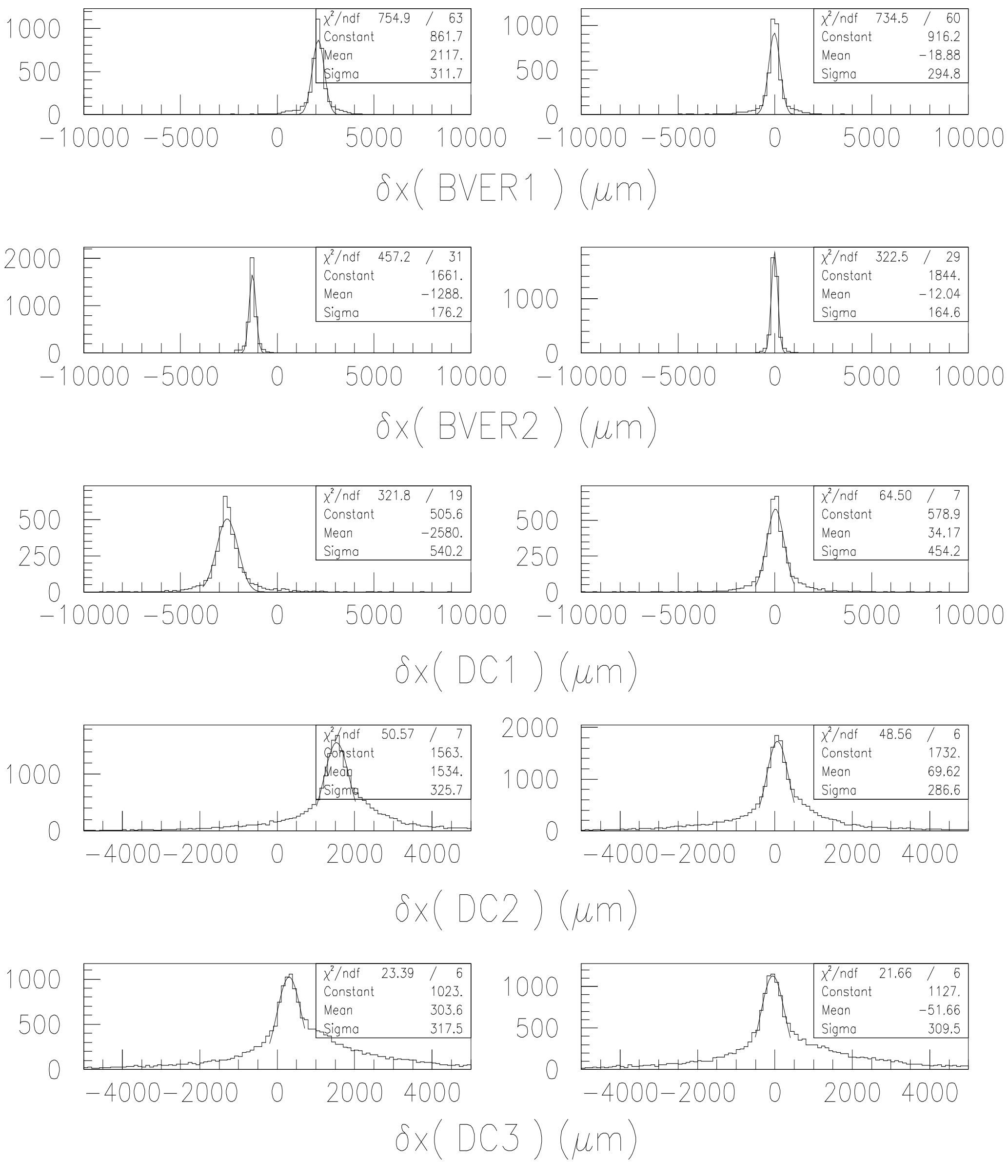

Figure 3.8: The δx of two BVERs, DC1, 2 and 3 before (left) and after (right) the x position alignment for the 1992 run.

	1992 RUN			1993 RUN		
	z	x_{Survey}	$x_{Correct}$	z	x_{Survey}	$x_{Correct}$
BVER1	-563.0	0.0	0.3437	-585.6	0.0	0.0351
BVER2	-258.0	0.0	0.0554	-279.9	0.0	-0.2813
DC1	196.3	10.0	-0.9553	—	—	—
DC2	692.5	15.6	0.4998	540.0	15.6	0.4781
DC3	1156.3	38.0	0.4797	1154.6	38.0	0.0106

Table 3.3: The surveyed x positions, x_{Survey}, and correction factors, $x_{Correct}$ in cm for two BVERs and three drift chambers for the 1992 and 1993 runs.

covers the whole collimator opening.

Before the DC1 cut, the low gain region in DC1 had to be restored. The beam region is insensitive to the minimum ionizing particle (*mip*), since the gain of pads corresponding to the middle four wires with 4 mm spacing was set lower during the data taking. Giving an arbitrary large number to the charge sum of those pads, all tracks through this region were assumed to pass the DC1 cut. Figure 3.9 shows the comparison of the projected y distributions of the reconstructed tracks at the surveyed z position of the DC1 before and after the low gain region is restored with DC1 cut[2].

Checking if DC1 has a cluster for each track increases the ratio of the number of real track to the uncorrelated background by discarding wrong tracks. Figure 3.10 shows the position differences of x and y, *i.e.*,

$$\delta x_{DC1} \equiv x_{proj} - x_{clus} \tag{3.7}$$

and

$$\delta y_{DC1} \equiv y_{proj} - y_{clus}, \tag{3.8}$$

where x_{proj} (y_{proj}) is the projected x (y) position of reconstructed track at the z position of DC1, and x_{clus} (y_{clus}) is the x (y) position of DC1 clusters. The signal to background ratio (S/N) is defined as the number of tracks above the uncorrelated background divided by that of background for $|\delta x_{DC1}| < 1.5$ cm and $|\delta y_{DC1}| < 1.3$ cm. The S/N is about 0.3 before the cut and 1.0 after the

[2]The fluctuation in the figure is from the nonlinearity of the charge sharing along y. No smoothing has been done to get an exact y position.

cut. These cut values are optimized, since the tighter cut on δx_{DC1} and δy_{DC1} results in losing the real tracks, as can be seen looking at the particle ID plot.

3.2.4 Dead Beam Region of DC2 and DC3 Pad Planes

The pad cells of DC2 and DC3 where the beam passes in a given magnetic field are not sensitive to the minimum ionizing particles, because the bipolar ADC signal by an earlier beam particle is huge, and *mip* contributes only a tiny bipolar signal on top of the tail which is still larger than the *mip* pulse height. For any particles passing through pads in the beam area, the tracks are reconstructed with the wire information only. Therefore it is necessary to find which wires are placed just above the pads of the beam region. Figures 3.11 and 3.12 show the charge sums of all pads above each wire of DC2 and DC3 for the two different magnetic field settings. Two different trigger conditions, beam and physics triggers, are displayed to see the effect of beam momentum protons. There was no difference beween two triggers and the wire numbers for the beam are summarized in Table 3.4.

3.3 Upstream Time of Flight Calibration

The following calibration is for the low resolution TOFU for the 1992 run.

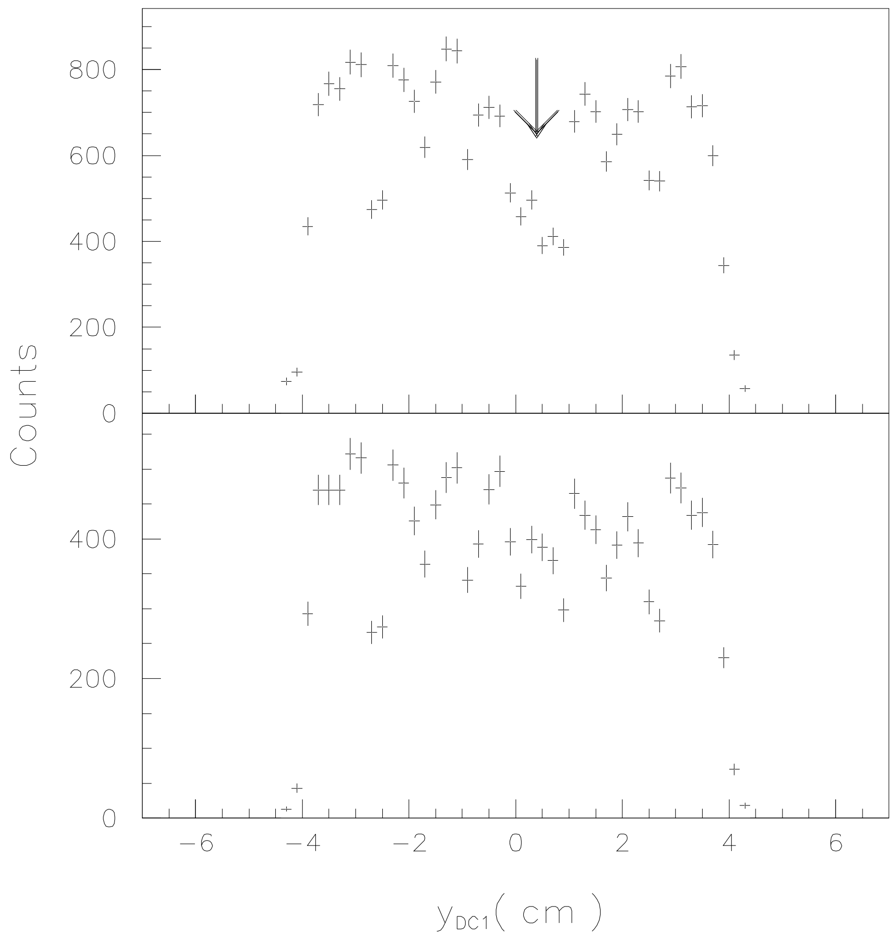

Figure 3.9: The comparison of the projected y distributions of the recontructed tracks at the z position of DC1 before (top) and after (bottom) the low gain region is restored. The arrow indicates the low gain region of DC1. For the explanation of the fluctuation, see text.

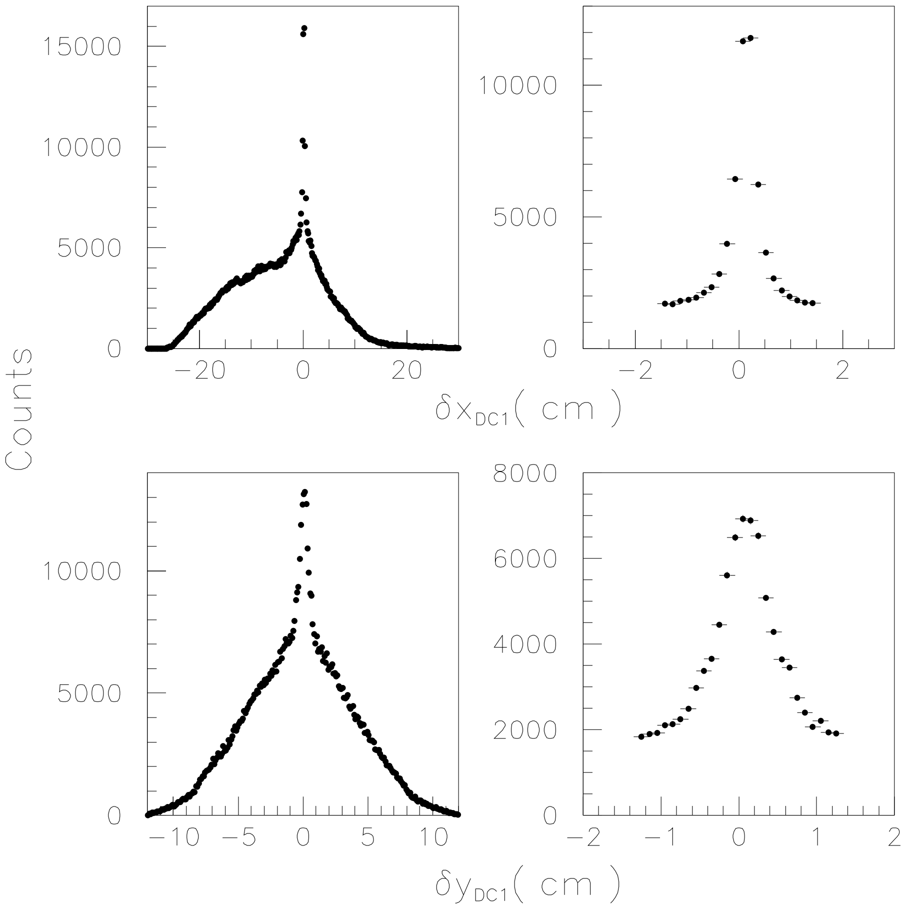

Figure 3.10: The δx_{DC1} (top) and δy_{DC1} (bottom) before (left) and after (right in expanded scale) the DC1 cut.

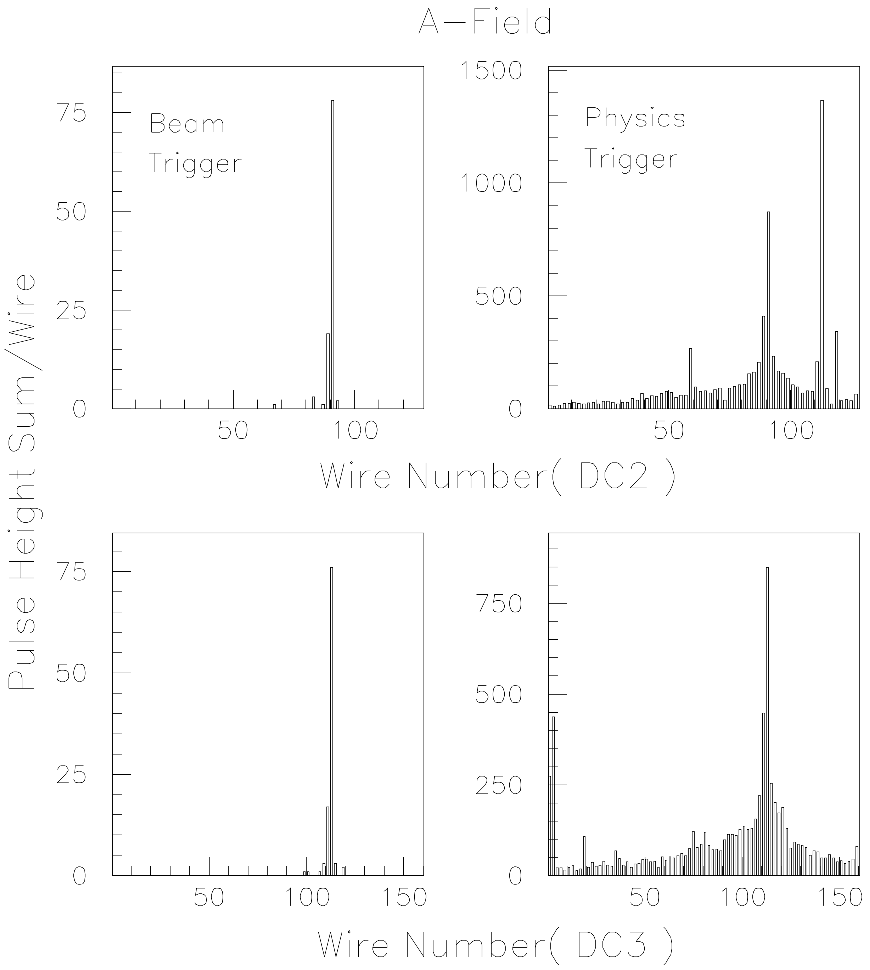

Figure 3.11: The charge sum of the pad cells below each wire of DC2 (top) and DC3 (bottom) for A-field. Beam (left) and physics (right) trigger conditions have been applied.

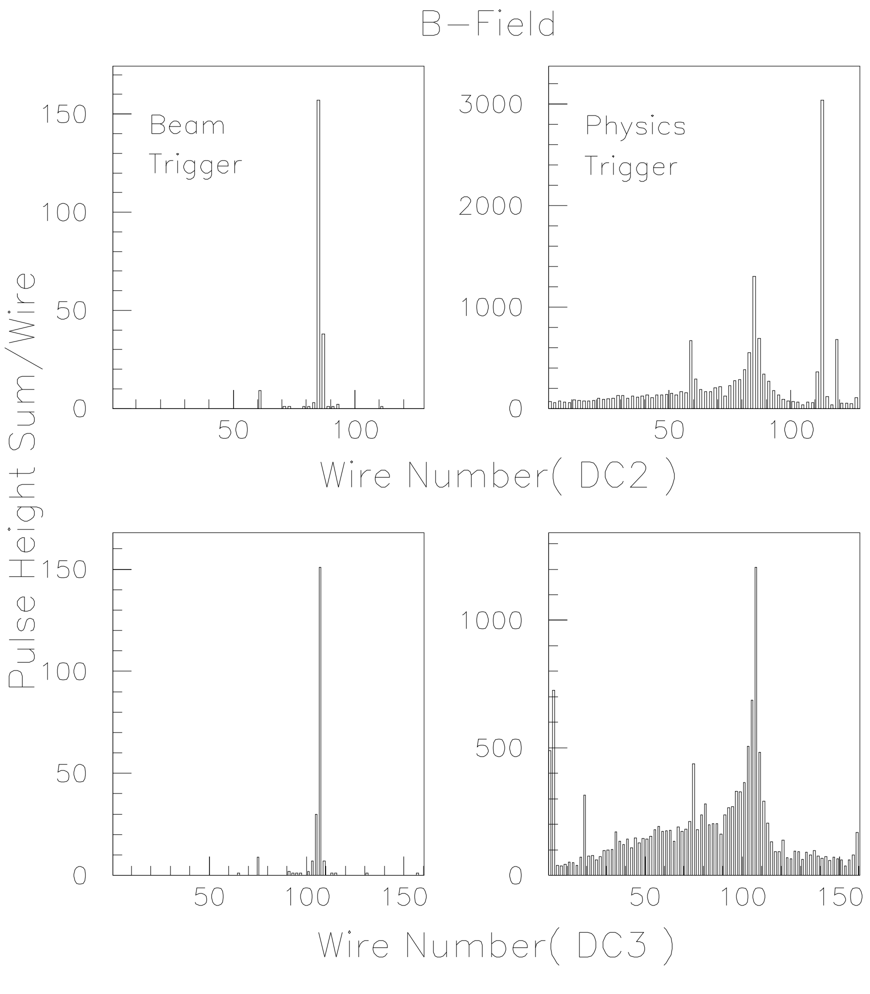

Figure 3.12: The charge sum of the pad cells below each wire of DC2 (top) and DC3 (bottom) for B-field. Beam (left) and physics (right) trigger conditions have been applied.

Field polarity	DC2	DC3
A	91	113
B	85	107

Table 3.4: Summary of the beam wires for two different fields.

3.3.1 Gain

For the amplitude calibration of TOFU, 60 Hz correction has been applied to the raw pulse height and the pedestal is substracted. Then the geometrical means of the pulse heights from the top and bottom phototubes are normalized by the minimum ionizing signal. The pedestal corrected, A_{raw}, and the normalized, A_{calib}, pulse heights for an arbitrary counter are shown in Fig. 3.13. The gain calibration will be important for the *mip* selection later.

3.3.2 Time : General

A schematic diagram of the upstream time of flight system is shown in Fig. 3.14. The common STOP of FASTBUS TDC is provided by one of the beam scintillator phototubes (S4-1) through an appropriate delay cable. All individual phototube signals from TOFU, as well as from the beam scintillator (S4-1), consist of STARTs. Recorded values are the time differences between individual STARTs and common STOP. The procedures for going from raw

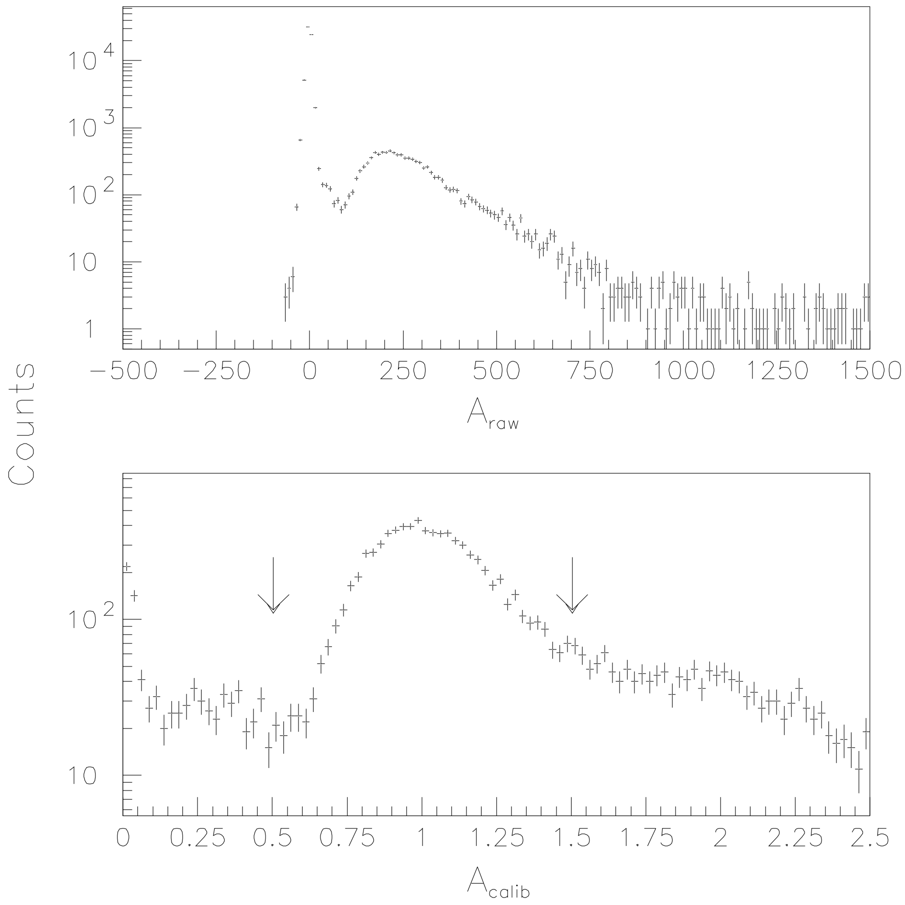

Figure 3.13: The pedestal corrected raw (top) and the calibrated (bottom) pulse heights of TOFU counter. Two arrows indicate the selection of *mip*, which will be used in the section of particle identification later.

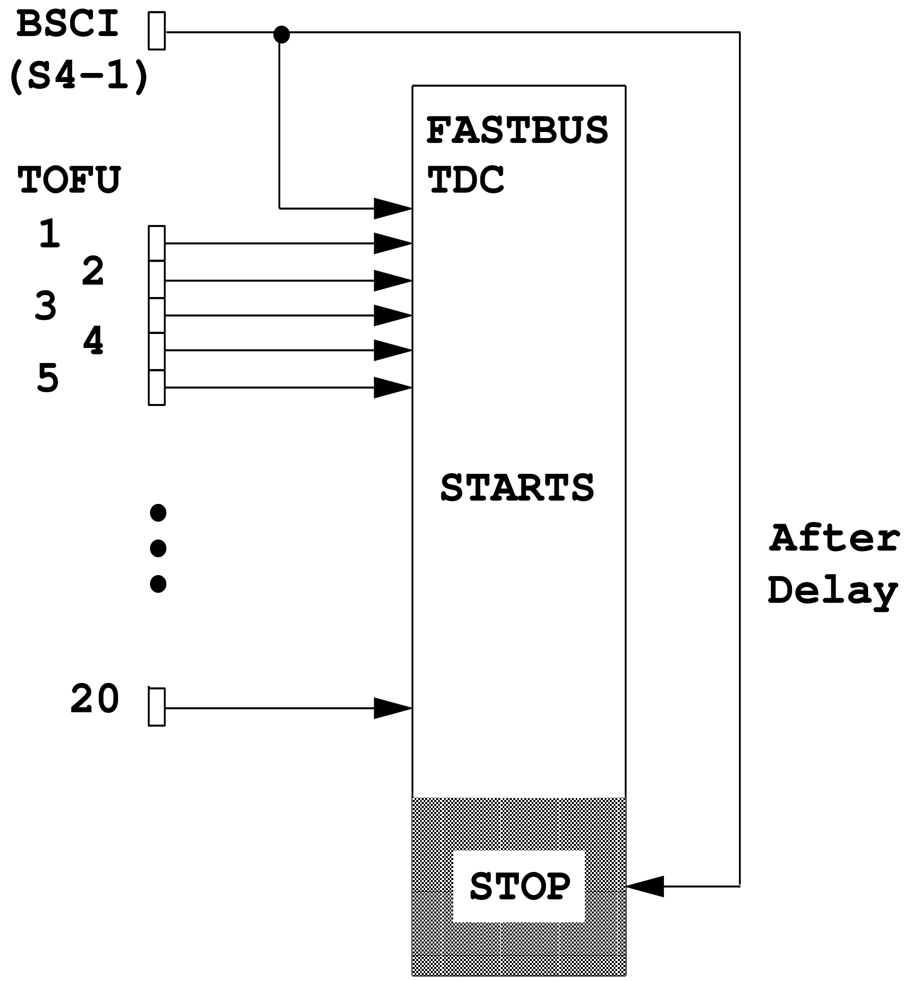

Figure 3.14: A schematic view of the time measurement in TOFU.

TDC information to true time are explained in the following sections.

3.3.3 Time : Pulse Height Correction

The pulse height fluctuation will cause worse time resolution, *i.e.*, a smaller pulse will trigger discriminator threshold later and *vice versa*. To minimize this effect, the so called slewing correction is applied, before the absolute time (T_0) is determined. However, there is always a possibility for a slewing effect to be masked by the attenuation of scintillating light during propagation in the scintillator. Therefore for the slewing correction determination, it is necessary to restrict signal samples within a certain range of vertical positions.

Figure 3.15 shows the correlation between inverse pulse height and time defined as

$$A^\star \equiv \frac{1000}{A_{calib}} \tag{3.9}$$

and

$$\delta T_0 \equiv \alpha(T_{raw} - \delta - T_{beam}) - T_{ref}(\mathrm{ns}) \tag{3.10}$$

where α is the TDC conversion factor (-0.025 ns/channel), T_{raw} is the raw TDC information in channel, δ is an arbitrary constant (3400 in this analysis), T_{beam} is S4-1 time and T_{ref} is the time calculated for $v = c$ particle to follow the exactly same path. Here T_{beam} was subtracted to eliminate the electronic jitter of the common STOP. In the analysis only particles within -5 $< y <$ 5 cm at the upstream face of the wall, according to the track reconstruction

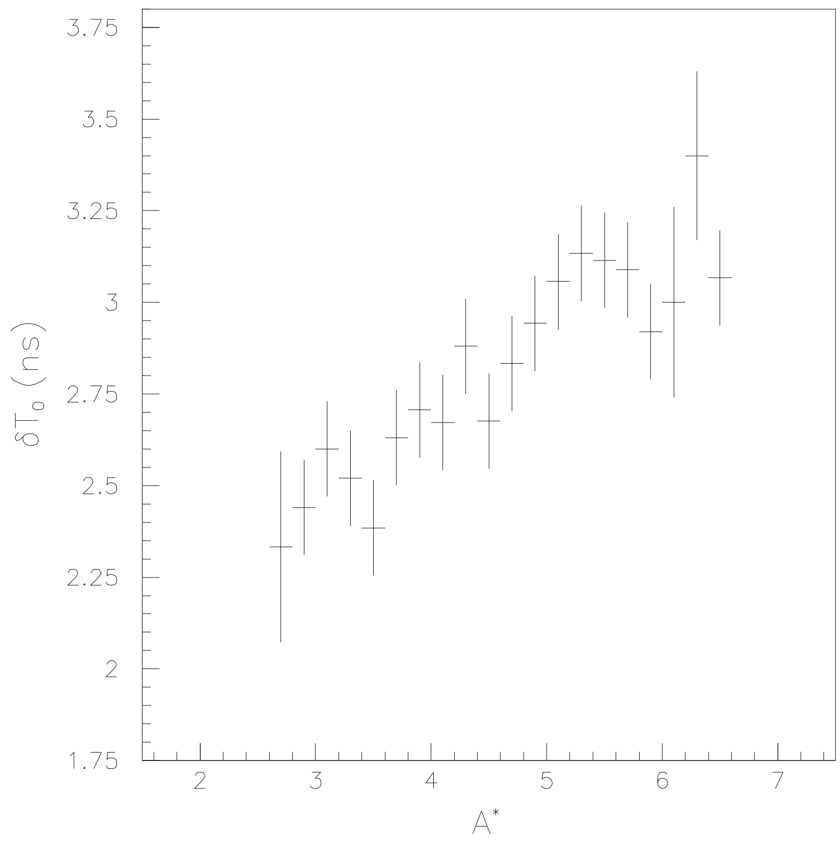

Figure 3.15: The correlation between the raw time, δT_0, and the inverted pulse height, $A^{\star}$, for the slewing correction.

by drift chambers, were considered. In this way we assumed the absence of differences in pulse height due to light attenuation as mentioned before. It also has to be noted that all the time calibrations, including Fig. 3.15, have been done only for relatively high momenta ($p \geq 2.0$ GeV) and negatively charged particles as determined by track reconstruction. Since the number of K^- and antiprotons is negligible (less than 5 %), compared to that of π^-, it is justified to assume that all entries in the sample have the speed of light. These are the only possible candidates for T_0 determination. The fitting parameters of a distribution like Fig. 3.15 to a linear function:

$$\delta T_s \equiv c_o + c_1 \times A^\star(\mathrm{ns}) \tag{3.11}$$

for all counters are summarized in Table 3.5 for one run. Table 3.5 shows only the coefficient c_1, which is important now, since c_0 will be changed by T_0 alignment in the next section. This coefficient has been determined for about every fifth run.

3.3.4 Time : Propagation of the Scintillating Light

Figure 3.16 shows the correlation between the slewing corrected time,

$$\delta T_v \equiv \delta T_0 - \delta T_s(\mathrm{ns}) \tag{3.12}$$

and

$$y' \equiv \frac{L_{TOFU}}{2} - y_{QUANAH}(\mathrm{cm}) \tag{3.13}$$

where L_{TOFU} is the length of TOFU counter (60 cm) and y_{QUANAH} is the vertical position of the hit by the pattern recognition code. This is true for the

Counter	Top	Bottom	Counter	Top	Bottom
1	0.4293	0.3383	11	0.1122	0.3078
2	0.0821	0.1467	12	0.4707	0.3554
3	0.3118	0.3575	13	0.2398	0.1330
4	0.4048	0.1871	14	0.2802	0.2732
5	0.2503	0.1098	15	0.2119	0.2607
6	0.1602	0.1474	16	0.2479	0.3341
7	0.1607	0.2404	17	0.2100	0.2103
8	0.1427	0.0551	18	0.3379	0.2424
9	0.1464	0.0908	19	0.3012	0.3057
10	0.1080	0.1300	20	0.3356	0.3833

Table 3.5: One example of the slewing parameter, c_1, for the correlation between the raw time and the pulse height. This table is for the run 5164 which is the begining of the physics runs. "Top" means top phototube and "bottom" means bottom phototube for each counter.

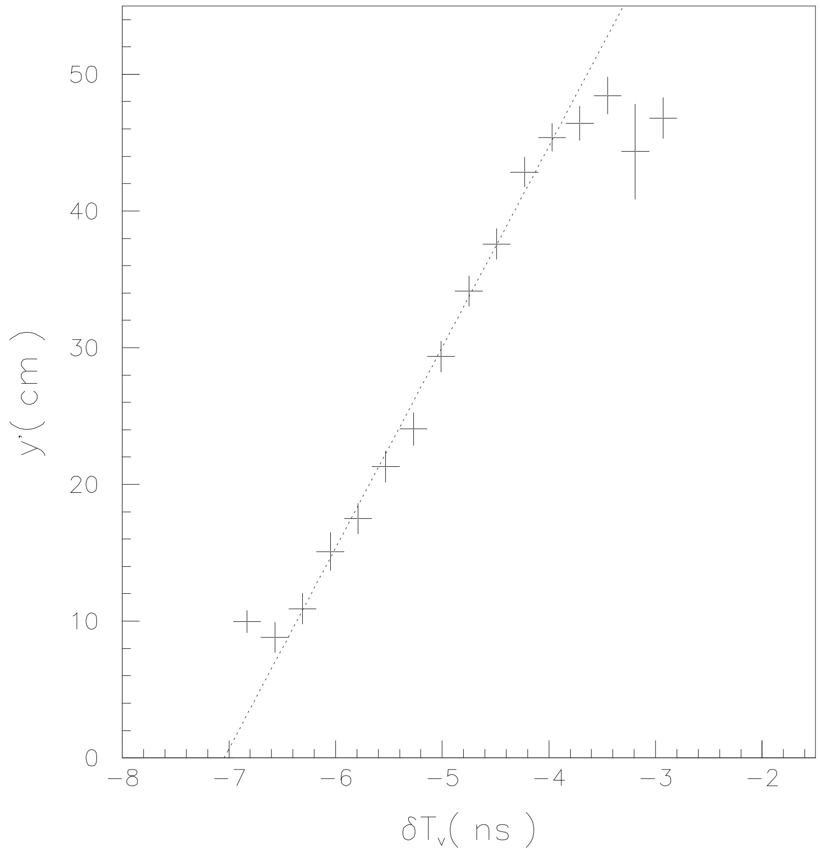

Figure 3.16: The correlation between y' and the slewing corrected time, δT_v, of each hit by the pattern recognition. The dotted line represents the linear fit to the data of this specific counter.

top phototubes, and the same correlation can be made for the bottom phototubes by reversing the sign in the y' definition. The variable y' corresponds to the distance from the hit position to the considered phototube. The slope of the distribution represents the propagation velocity parameter ($\equiv < v >$) in cm/ns of the scintillating light inside counter. Parameters $< v >$ for all counters are summarized in Table 3.6.

3.3.5 Time : T_0

As a last step of the time calibration, the absolute time adjustment, T_0, needs to be done. Since only $\beta \approx 1$ particles (high momentum π^-) were chosen in the beginning, we will have the true time by shifting $\delta T_v - y'/ < v >$ to zero. Defining

$$\delta T_{u(d)} \equiv \delta T_v - \frac{y'}{< v >} + C_{u(d)}, \tag{3.14}$$

where $C_{u(d)}$ is the time offset for the up (down) phototube, the time of flight (TOF) can be calculated by averaging over two values, *i.e.*,

$$TOF \equiv \frac{\delta T_u + \delta T_d}{2} - \frac{L_{TOFU}}{2\cdot < v >}. \tag{3.15}$$

Table 3.7 summarizes the time resolution, $\delta(TOF)$, which is the sigma of the gaussian fit to the distribution of TOF for each counter. The average time resolution:

$$\delta(TOF) \equiv \frac{1}{N_{TOF}} \sum_{i=1}^{N_{TOF}} \sigma_i = 227.4\text{ps}, \tag{3.16}$$

where N_{TOF} is the number of TOFU counter (20) and σ_i is the width of the gaussian fit to the time distribution of counter i, was achieved.

Counter	$< v >$(cm/ns)	Counter	$< v >$(cm/ns)
1	16.75	11	15.73
2	16.36	12	19.32
3	16.25	13	17.51
4	17.30	14	16.62
5	16.87	15	15.67
6	16.77	16	16.57
7	16.30	17	16.11
8	16.27	18	16.22
9	16.75	19	16.12
10	14.82	20	16.30

Table 3.6: Propagation velocity parameter, $< v >$, in cm/ns for the individual counters.

Counter	σ_i(ps)	Counter	σ_i(ps)
1	197.3	11	221.0
2	206.6	12	238.0
3	238.0	13	214.1
4	237.5	14	249.3
5	203.3	15	216.0
6	214.1	16	221.9
7	247.0	17	227.2
8	225.8	18	228.7
9	206.3	19	222.7
10	285.9	20	246.4

Table 3.7: The time resolution of each TOFU counter in ps.

Chapter 4

Analysis II

4.1 ^{28}Si + Pb Reaction

4.1.1 Particle Identification

The first particle selection has been done using the pulse height information from the upstream time of flight wall. Any particle that generated the calibrated pulse height within a range between 0.5 and 1.5 was considered to be a minimum ionizing one[1] (Fig. 3.13).

In the plot of Z/p vs. TOF being applied by the above criterion (Fig. 4.1), we can identify particles rather clearly as $\pi^{\pm}$, $K^{\pm}$, proton and deuteron at relatively low momenta. Figure 4.2 shows the projection of p and TOF

[1] For p = 2 - 5 GeV, the $-dE/dx$ of π is about 30 % higher than kaon, proton and deuterons. The correction for this has been determined by Monte - Carlo simulation. When we applied the same cut with 30 % higher peak position for $-dE/dx$, we need to correct about 21 % for overall normalization.

onto the mass for $TOF \geq 41.8$ ns. The particle mass was determined by

$$m = \frac{p}{\beta\gamma} \tag{4.1}$$

where $\gamma = 1/\sqrt{1-\beta^2}$. Since every time of flight analysis was made with respect to the particle with the speed of light, the relationship between measured time of flight (TOF) and the true one (T_{true}) is given by

$$T_{true} = TOF + T_{v=c} \tag{4.2}$$

where $T_{v=c}$ is the time calculated for a particle travelling at the speed of light to traverse the same flight path as the particle in consideration. Therefore β can be calculated by

$$\beta = \frac{T_{v=c}}{T_{true}}. \tag{4.3}$$

Specifically for the kaon analysis we used another display scheme for the particle identification, which was more convenient for the background subtraction. Figure 4.3 represents this new particle identification plot which is the correlation between p/Z and

$$\delta T \equiv T_{true} - T_K \tag{4.4}$$

where

$$T_K = T_{v=c}\sqrt{(\frac{m_K}{p})^2 + 1} \tag{4.5}$$

is the time required, assuming kaon mass (494 MeV) and same flight path. The kaon peak shows a near gaussian distribution, projecting onto the δT axis in a

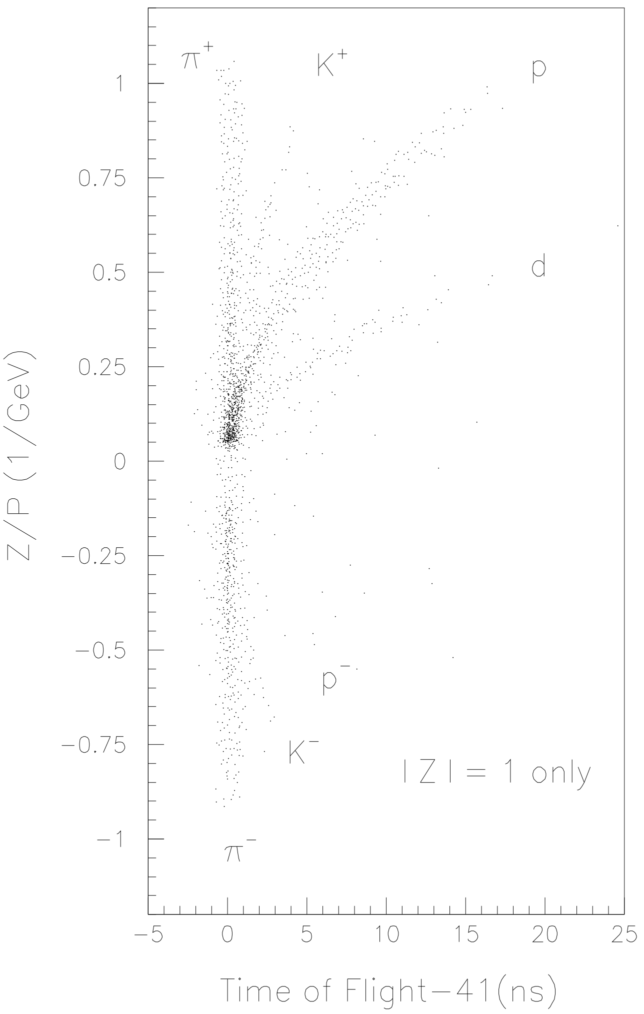

Figure 4.1: The Z/p vs. TOF for $|Z| = 1$ particle.

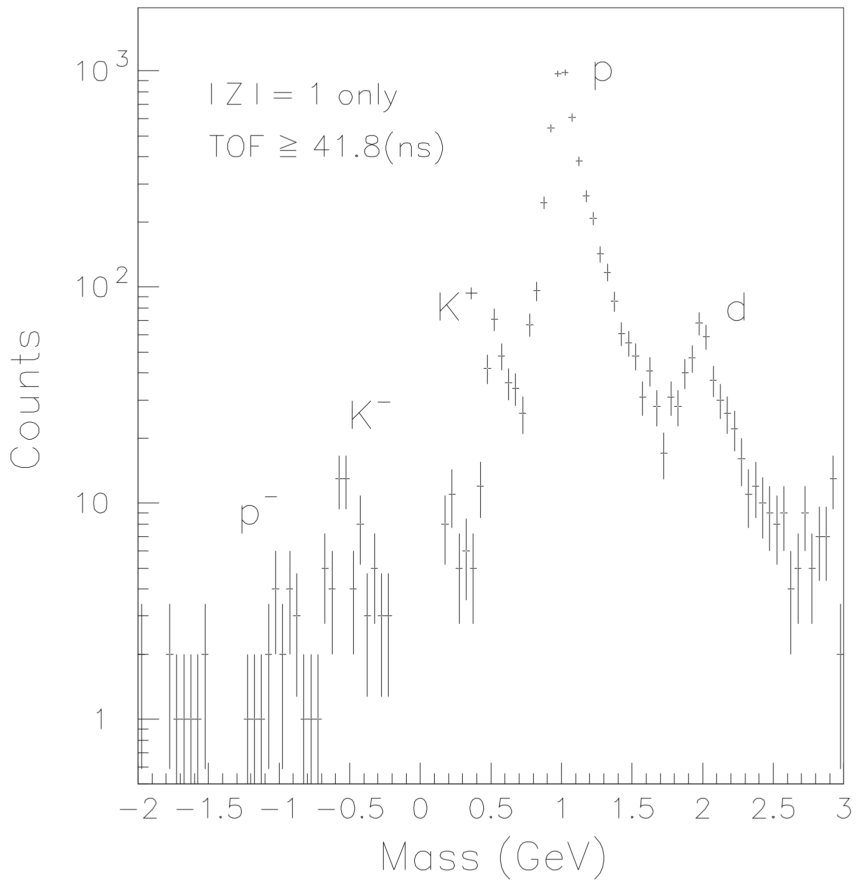

Figure 4.2: The projection of Z/p vs. TOF onto the mass in GeV for $TOF \geq 41.8$ ns.

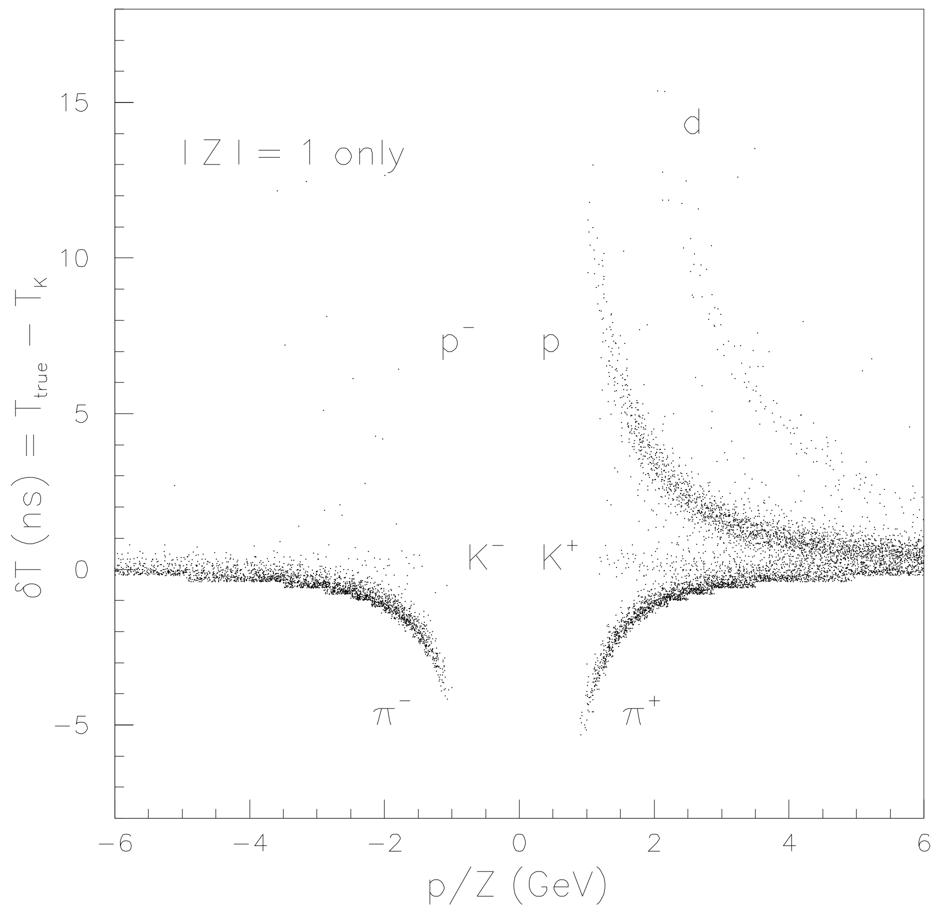

Figure 4.3: The δT, defined as the time difference between the true time of flight (T_{true}) and the required time assuming kaon mass (T_K), vs. p/Z for *mip*.

narrow momentum bin. The width of the δT distribution becomes wider than the intrinsic time resolution due to the momentum resolution ($\delta p/p \sim 3.6\%/\beta$, see chapter 2);

$$\delta T_K = T_{v=c} \frac{m_K^2 \delta p}{p^3 \sqrt{(m_K/p)^2 + 1}}. \tag{4.6}$$

Therefore the overall resolutions of δT were estimated about 245 and 231 ps at $p = 2$ and 3 GeV respectively. The pion and proton peaks are supposed to be the superposition of infinite number of kaon - like distributions with different mean. However the width of proton is wider than pion, since the proton peak merges to kaon peak faster in our interesting momentum range (Fig. 4.3). We used a single gaussian function to fit δT distribution of each particle, since it seems to describe them well[2].

The projection of Fig. 4.3 onto δT for various momentum bins is shown in Fig. 4.4 for positive charge, and in Fig. 4.5 for negative charge. We have binned the momentum with 0.1 GeV width from 2.0 to 3.0 GeV. The coarsely hatched area stands for our pion and proton samples to simulate p_t behavior assuming kaon mass. After fitting pion and proton distributions with the gaussian function (dashed lines in Figs. 4.4 and 4.5), we subtracted them from the orignal δT distribution to determine if the leftover, pressumed, kaons

[2]The systematic error, caused by assuming a single gaussian shape, was negligible. We first generated many gaussians with there widths determined by the above formula for δT and the mean following the center of proton and π lines in Fig. 4.3. The sum of many gaussians for each momentum bin can be well described by one gaussian. Moreover the background amount from the tail of a gaussian function underneath kaon region was very small, less than 3 % (see section 4.1.3).

would show a gaussian shape. The resultant δT distributions of kaons, after the background subtraction, are shown in Figs. 4.6 and 4.7 with their gaussian fit. The sigma of all distributions are about 270 ps which is consistent with the earlier TOFU time analysis and a small contribution due to momentum resolution.

The acceptance (p_t vs. y) of the selected kaon is shown in Fig. 4.8. The dead beam region of DC1 is reflected by the fact that there are no entries along $p_t = 0$ in the acceptance. The low rapidity edge is from the geometrical shape of our opening and the high rapidity edge is due to the particle identification, *i.e.*, momentum cut.

4.1.2 Acceptance Correction

The acceptance correction due to the geometrical limit and asymmetry was determined by using a Monte - Carlo simulation of the complete experimental apparatus. The GEANT [51], CERN computer library program, allows us to set up the whole detector geometry with proper material and to simulate the physics processes including particle interaction in the detector materials. A sample of 10 million kaons for each charge was generated in a 8.5° forward cone with a flat distribution in y and p_t. The generated particles were propagated through the hole of the collimator. The time of flight and position at TOFU were determined for a given magnetic field. Since we let kaons decay during the flight with a given life time (12.4 nsec), the decay probability is already included in the correction factor.

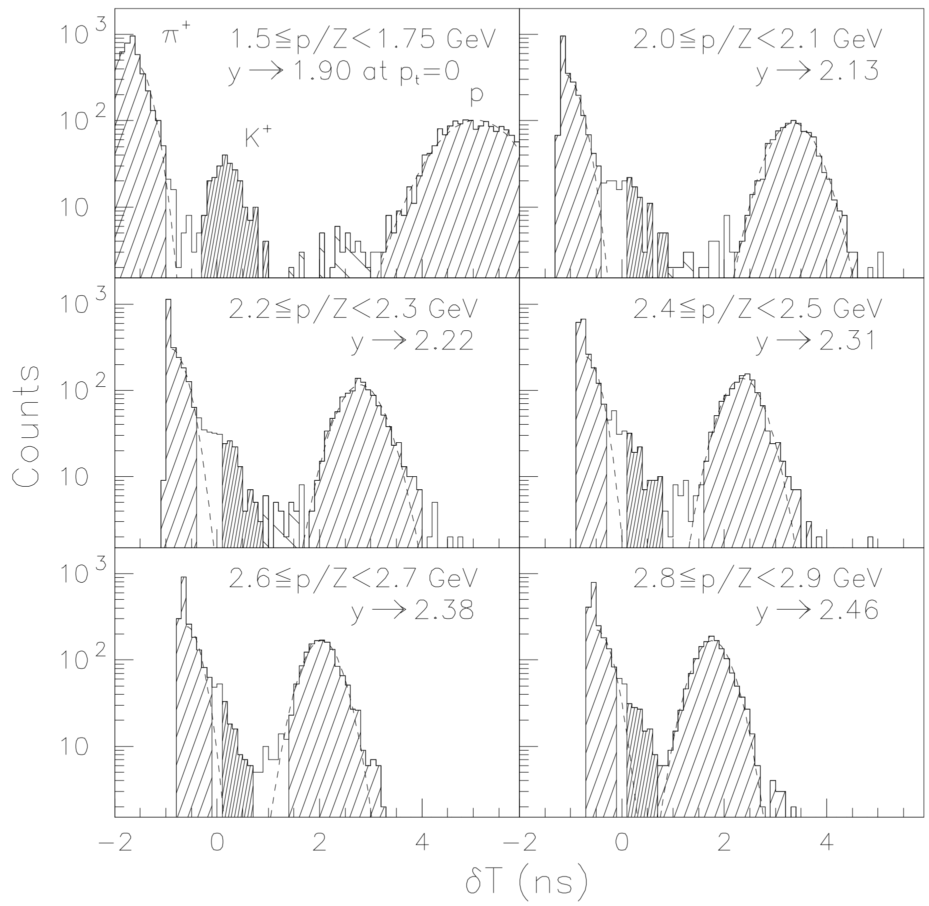

Figure 4.4: The δT distribution for K^+.

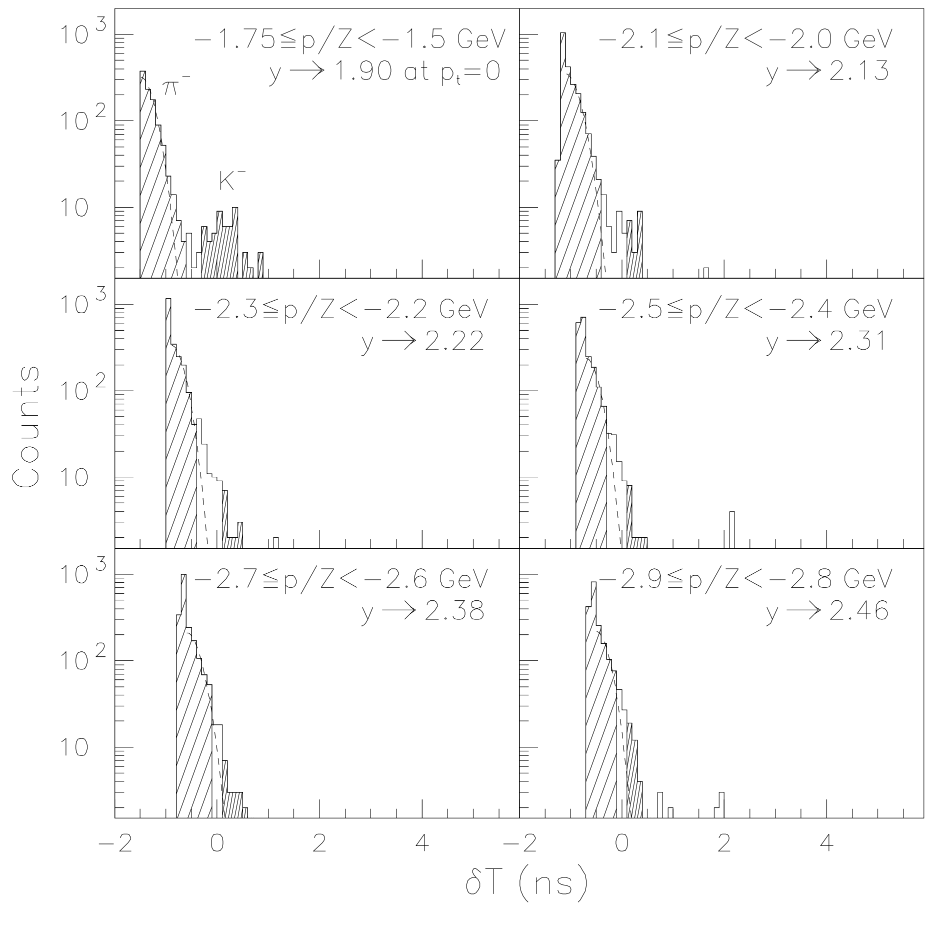

Figure 4.5: The δT distribution for K^-.

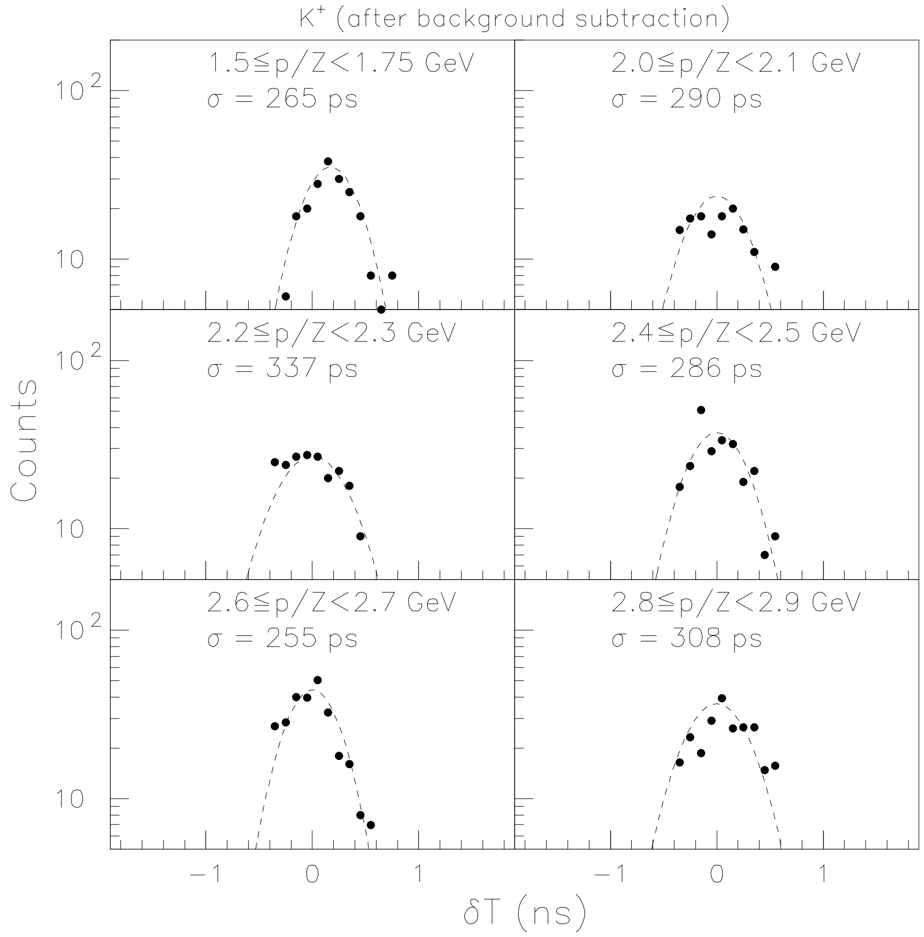

Figure 4.6: The δT distribution of K^+ after the background subtraction.

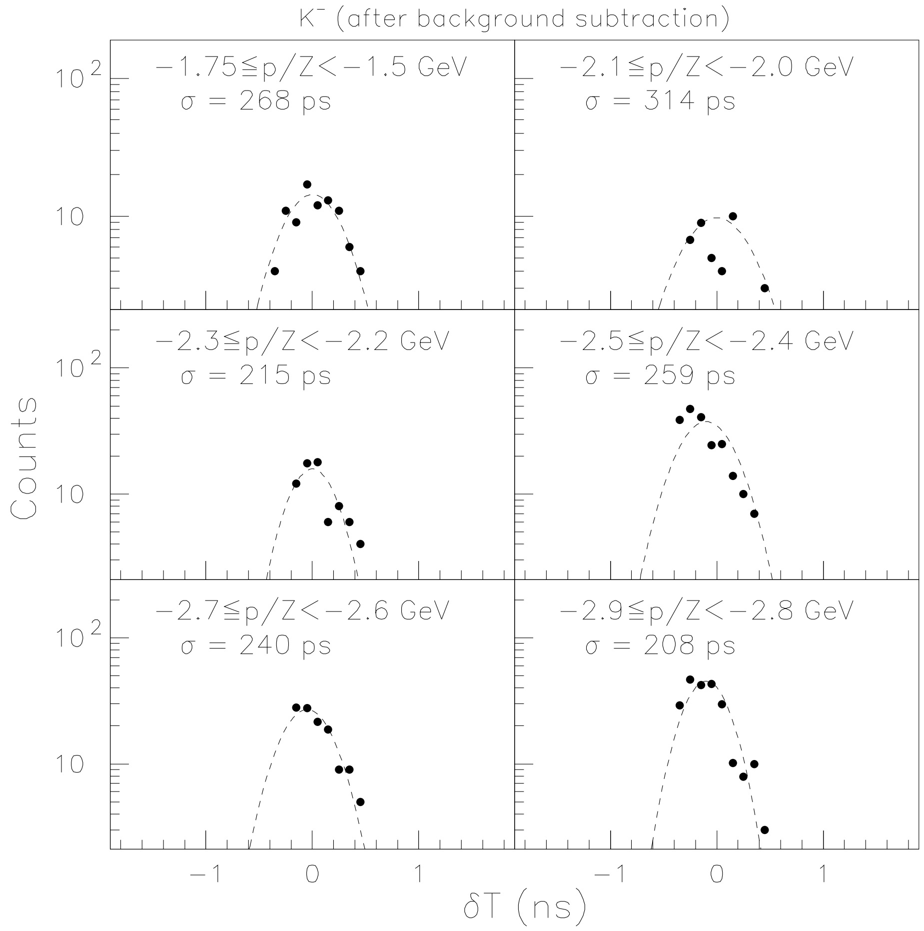

Figure 4.7: The δT distribution of K^- after the background subtraction.

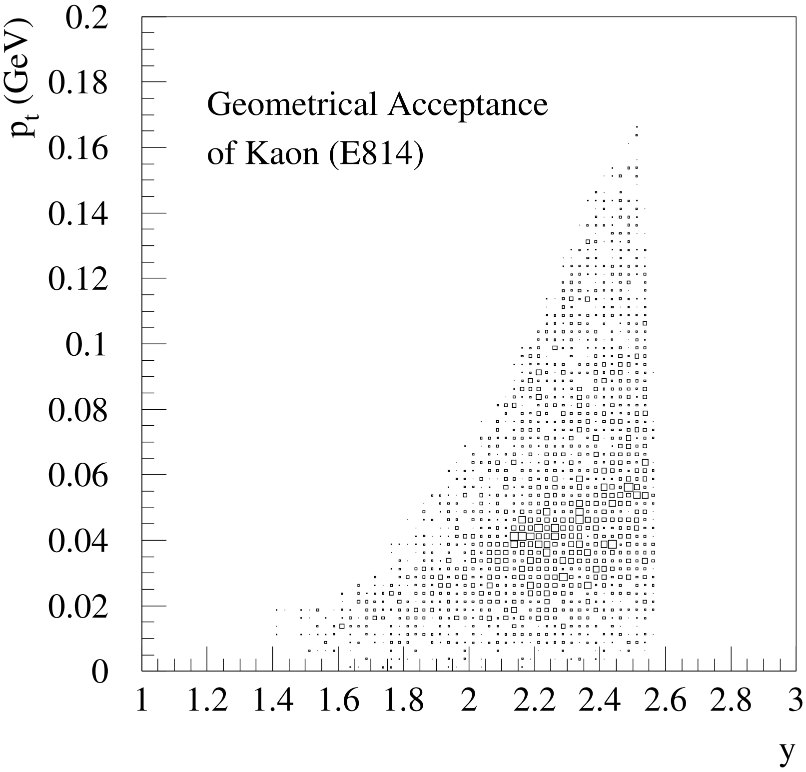

Figure 4.8: The acceptance of E814 for kaon.

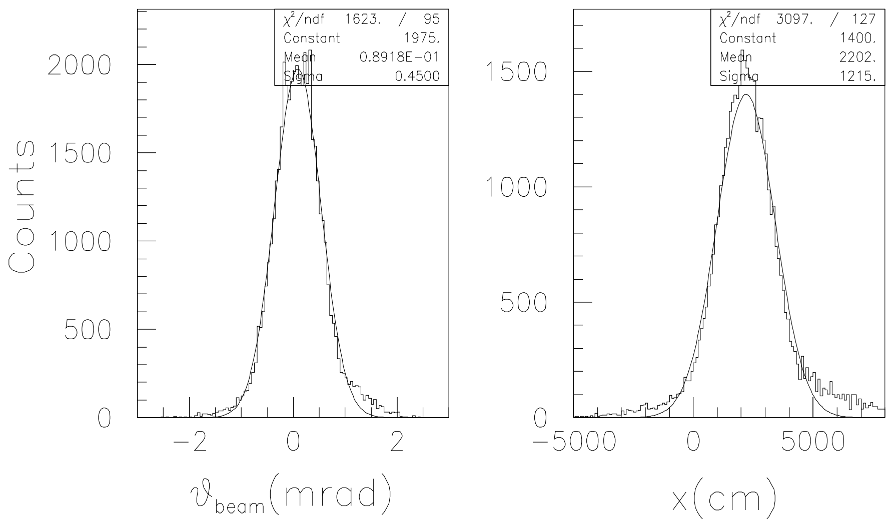

Figure 4.9: The informations provided by BVER, *i.e.*, incident angle of the beam (left) and x position of the beam vertex at $z = 0$ (right), with their gaussian fits.

In order to simulate as closely as possible real beam status, the BVER informations were considered, for example, distribution of beam angle, x position of the beam at the target, etc. (Fig. 4.9). All necessary inputs are summarized in Table 4.1. In the event generator, the vertex x position was randomized as

$$x_{vertex} = < x > + \sigma_x \cdot x_{NORAN} \tag{4.7}$$

where $< x >$ is the mean and σ_x is the sigma of gaussian fit to the x distribution of the beam at the target and x_{NORAN} is a random number generated with normal distribution [52]. The averaged beam angle was then calculated by

$$\theta_{beam} = < \theta_b > + \frac{\sigma_b}{\sigma_x}(x_{vertex} - < x >) \tag{4.8}$$

where σ_b is the beam divergence. Then the new momentum components were used to be determined by the rotation matrix;

$$\begin{pmatrix} p'_x \\ \\ p'_z \end{pmatrix} = \begin{pmatrix} \cos\theta_{beam} & -\sin\theta_{beam} \\ \\ \sin\theta_{beam} & \cos\theta_{beam} \end{pmatrix} \begin{pmatrix} p_x \\ \\ p_z \end{pmatrix}. \tag{4.9}$$

In addition to the beam conditions, the dead beam region of DC1, $-1.0 < x \leq 0.1$ cm and $-0.4 < y \leq 0.8$ cm, was also considered. All tracks passing through this region were suppressed so that they were not considered as accepted particles in the downstream spectrometer. The geometrical effect to the correction factor is complicated by the fact that the collimator opening is rectangular leading to acceptance loss, which depend on the orientation of the particle within this opening.

Input item(units)	Symbol	Value
Averaged Beam Angle(mrad)	$<\theta_b>$	0.089
Beam Divergence(mrad)	σ_b	0.45
Displacement of Beam at $z=0$(mm)	$<x>$	2.2
Sigma of $<x>$(mm)	σ_x	1.2

Table 4.1: Summary of the inputs by BVER with their notations.

The generated and accepted kaon distributions were divided into bins of 0.1 units of rapidity, and for each rapidity bin a p_t spectrum with 0.01 GeV binning was produced. Then the ratio (ϵ) of the accepted to the generated number of kaons for each y and p_t bin was calculated. Figure 4.10 shows the result for several rapidities. Each bin of the measured p_t spectrum is divided by this ratio.

4.1.3 Background Subtraction in p_t Distribution

The necessary variables to estimate the amount of contamination due to $\pi^{\pm}$ and proton to be subtracted from the p_t spectra are defined in Fig. 4.11. Each of these particles has been selected by

$$K^{\pm}; T_K^d < \delta T \leq T_K^u$$

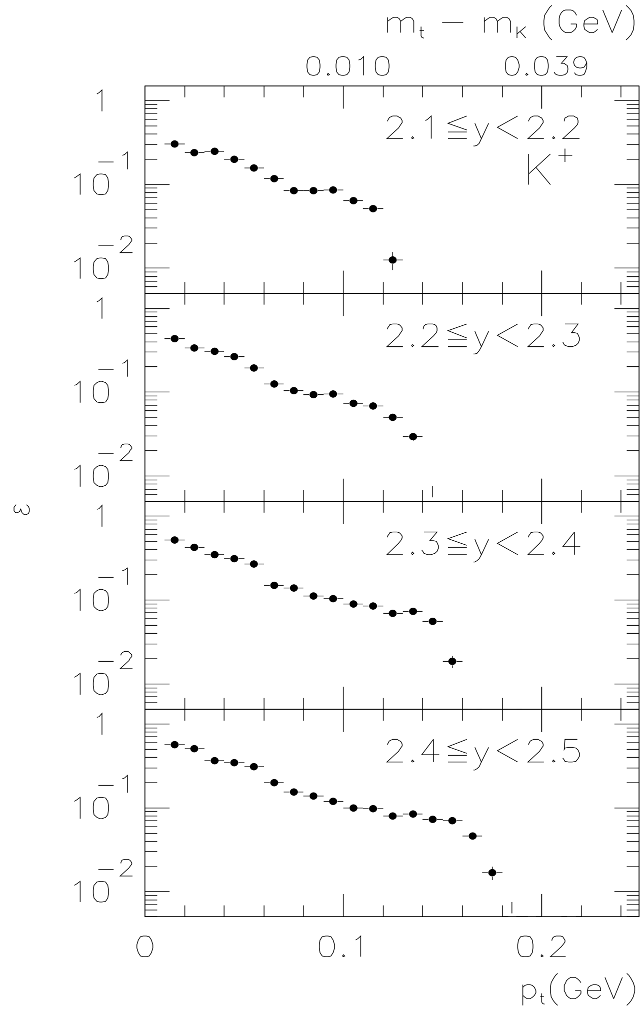

Figure 4.10: The acceptance correction factor (ϵ) for K^+. The error bars are statistical.

$$\pi^{\pm}; -\infty < \delta T \leq T_{\pi}^{u} \tag{4.10}$$

$$p; T_p^d < \delta T \leq T_p^u.$$

The integrals;

$$I_{\pi}^{1(2)} \equiv \int_{-\infty(T_K^d)}^{T_\pi^u(T_K^u)} G_\pi(x)dx \tag{4.11}$$

and

$$I_{p}^{1(2)} \equiv \int_{T_p^d(T_K^d)}^{T_p^u(T_K^u)} G_p(x)dx, \tag{4.12}$$

where

$$G_{\pi(p)}(x) \equiv C_{\pi(p)} e^{-\frac{1}{2}(\frac{x-T^0_{\pi(p)}}{\sigma_{\pi(p)}})^2} \tag{4.13}$$

with $x \equiv \delta T$, and C and σ are the amplitude and sigma of the gaussian, were used to estimate the possible contamination underneath kaon region by I_π^2/I_π^1 and I_p^2/I_p^1 for pion and proton respectively. Considering a 78 % tracking efficiency, we show the background subtracted kaon spectra together with the possible background sources, assuming kaon mass, in Fig. 4.12.

The most significant systematic error is from the assumption of the shape for the misidentified tracks, constant background. In this analysis, we estimated about 25 % of constant background, assuming a flat distribution of δT in the kaon region. However, if we assumed an exponential shape of background, this estimation increased up to about 65 %. As a result of such an uncertainty, we can give a rather large amount (about 53 % from $\delta N_K/N_K$(flat), where $\delta N_K \equiv N_K$(flat) $- N_K$(exp) and N_K is the number of kaon yield) of systematic error to our kaon spectra for ^{28}Si induced collision.

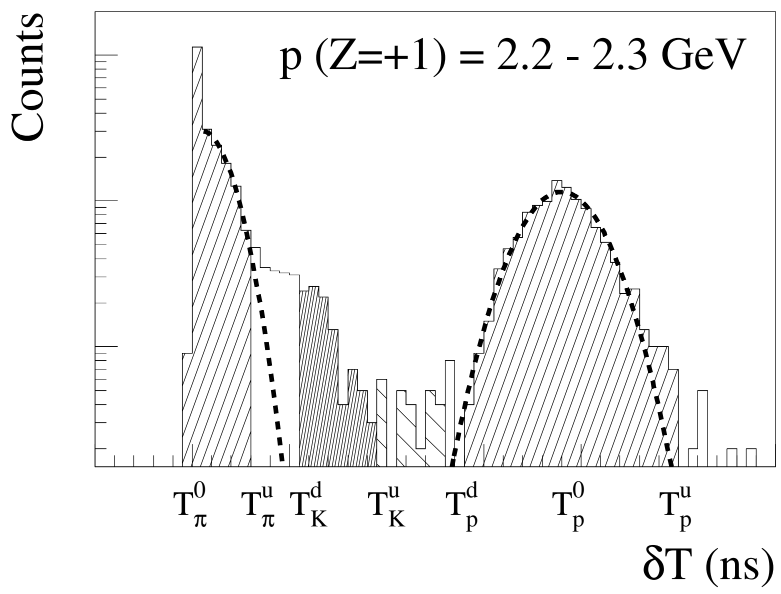

Figure 4.11: The definition of variables to determine background.

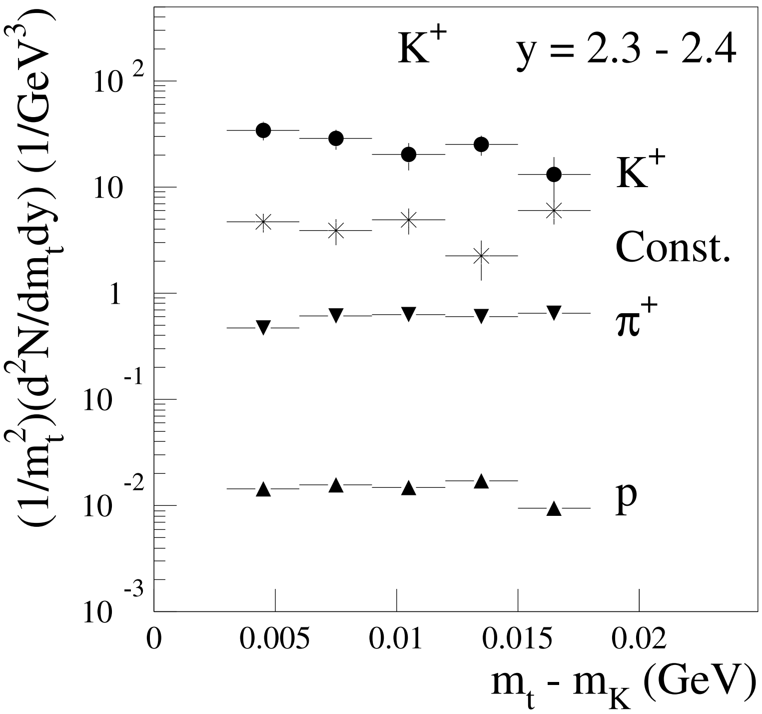

Figure 4.12: The shape comparison of K^+ spectrum with backgrounds.

4.2 ^{197}Au + Au Reaction

4.2.1 Particle Identification

The plot of Z/p vs. TOF for $|Z| = 1$ particles, whose calibrated TOFU pulse height is between 0.88 and 1.3, (Fig. 4.13) shows that we can identify particles such as $e^{\pm}$, $\pi^{\pm}$, $K^{\pm}$, proton and deuteron, etc. Here we used three measurements to verify the y positions to increase the signal to background ratio (S/N), *i.e.*, we first made all the possible y combinations ($y_{DC2} - (z_{DC2}/z_{DC3}) \cdot y_{DC3}$, $y_{DC3} - (z_{DC3}/z_{TOFU}) \cdot y_{TOFU}$ and $y_{TOFU} - (z_{TOFU}/z_{DC2}) \cdot y_{DC2}$) and applied very conservative cuts to these three correlations as shown by arrows in Fig. 4.14. This procedure increases the S/N about 70 % overall. Fig. 4.15 shows the mass spectra at four different kaon rapidity bins together with the fitting of the sum of three gaussians, corresponding to π^+, K^+ and proton each, and one exponential background[3]. It shows that the gaussian and exponential functions represent the mass and background shapes well. The acceptance of E877 for kaon is shown in Fig. 4.16 with a 3.5 GeV momentum cut at the high rapidity edge.

Having better time resolution and enough statistics for ^{197}Au induced collisions, we can divide the acceptance into small cells with 0.1 units of y_K and 0.02 GeV units of p_t, and then generate the mass plot. By fitting each

[3]There is no physical reason why we choose an exponential background. The systematic error due to this will be discussed below.

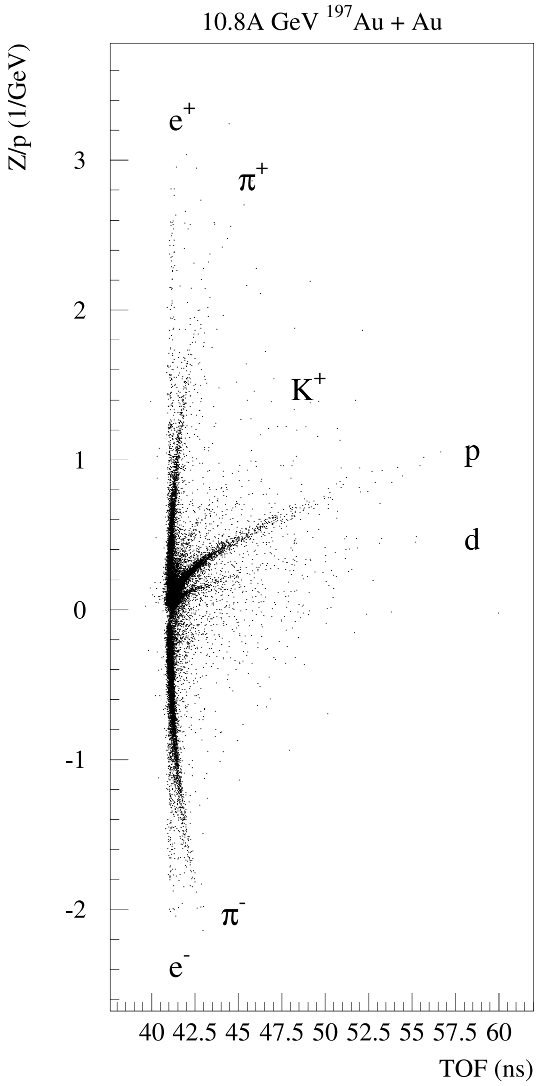

Figure 4.13: The Z/p vs. TOF for $|Z| = 1$ particles (1993 run).

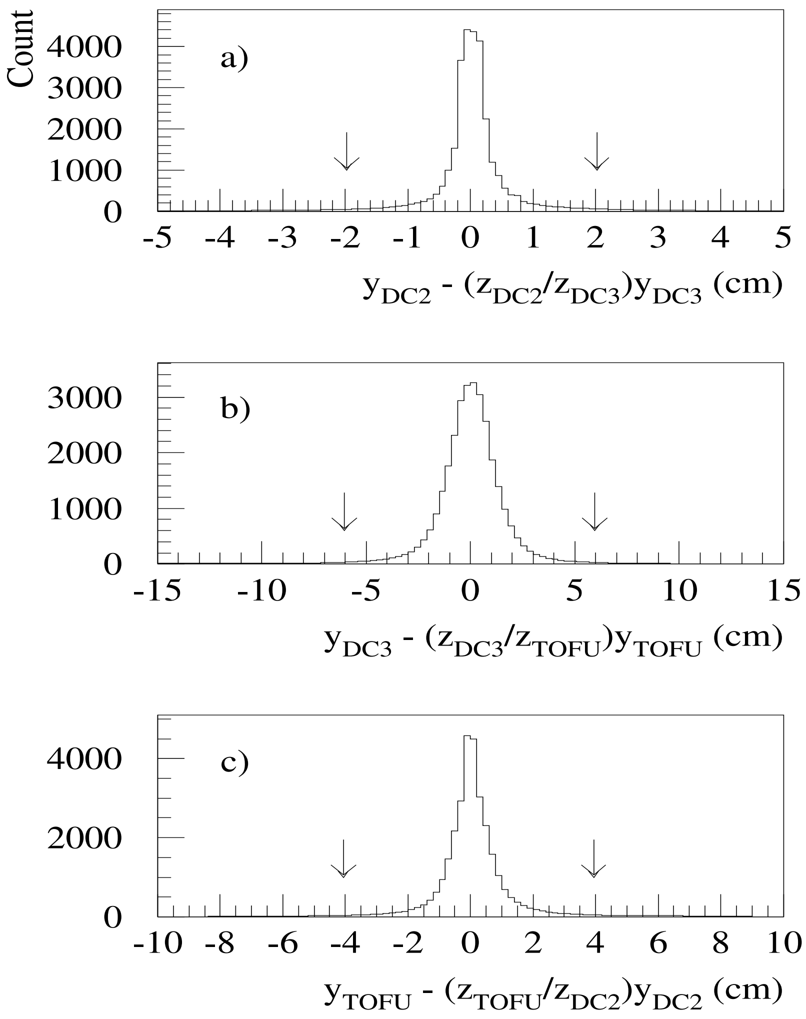

Figure 4.14: (a) $y_{DC2} - (z_{DC2}/z_{DC3}) \cdot y_{DC3}$, (b) $y_{DC3} - (z_{DC3}/z_{TOFU}) \cdot y_{TOFU}$, (c) $y_{TOFU} - (z_{TOFU}/z_{DC2}) \cdot y_{DC2}$.

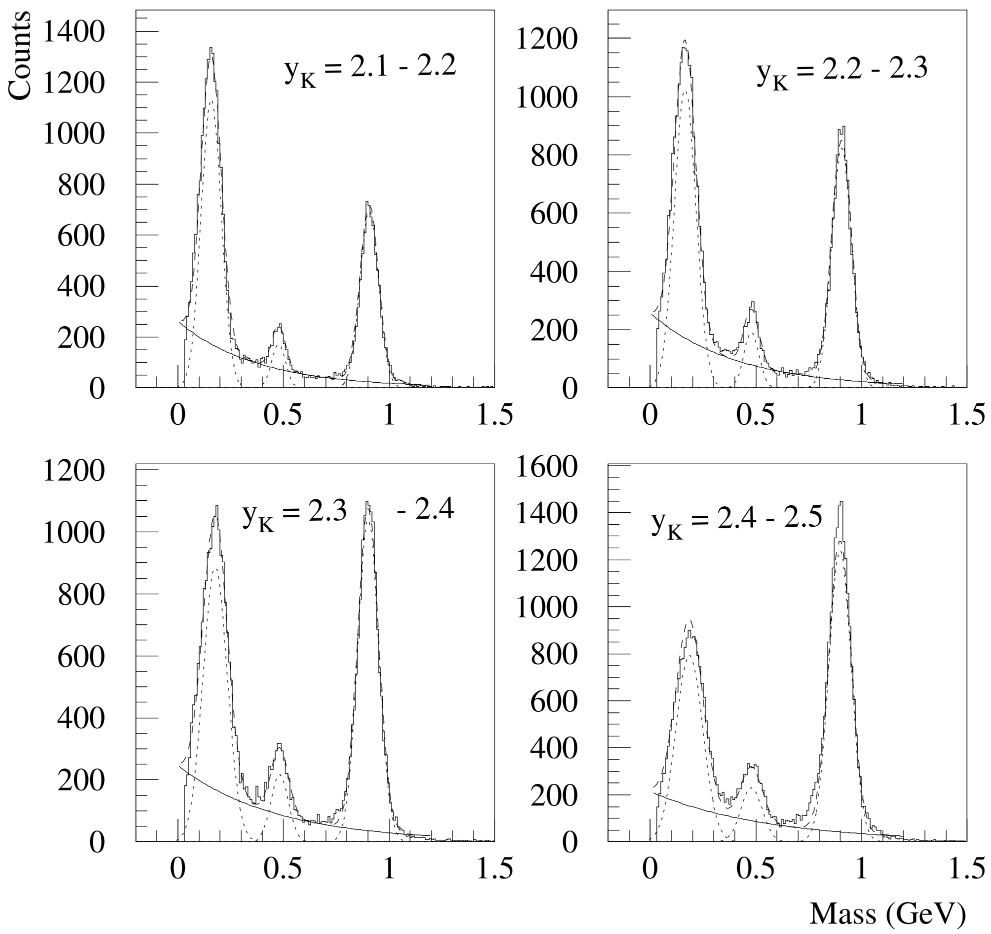

Figure 4.15: The mass spectra at four kaon rapidity bins together with the fitting of the sum (dashed line) of three gaussians (dotted lines) and an exponential shape background (solid line).

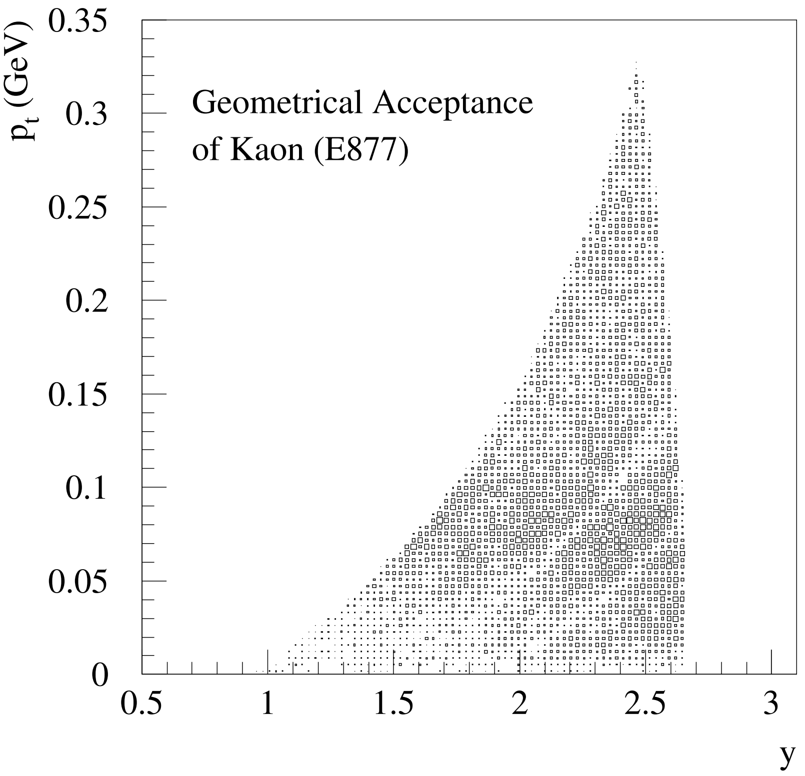

Figure 4.16: The acceptance of the E877 spectrometer for kaons (1993 run).

mass plot with the sum of a gaussian and an exponential background;

$$p_{g1} \cdot exp(-\frac{1}{2} \cdot (\frac{m - p_{g2}}{p_{g3}})^2) + exp(p_{e1} - p_{e2} \cdot m), \tag{4.14}$$

where p_{g1}, p_{g2} and p_{g3} represent the amplitude, mean and sigma of a gaussian, and p_{e1} and p_{e2} represent the amplitude and slope of the exponential respectively, we can estimate the number of kaons above the background. Fig. 4.17 shows the summary of the fitting parameters, *i.e.*, the mean and sigma of the gaussian and the slope of exponential, with their linear fit by dashed line. In order to reduce the systematic fluctuations, we used the fitted values, corresponding to the dashed line above, rather than the original values. Some examples of fit results are shown in Fig. 4.18.

The systematic error on the kaon yield, caused by using the exponential background, was about 9 %. This error was estimated by comparing the results between the exponential and linear backgrounds. Another systematic error on the kaon yield, caused by the uncertainty in the amplitude of the exponential background fit, was about 18 % on average[4]. The other conceivable source of systematic error is from the difference of the widths of kaon mass distribution between the measurement and calculation based on momentum and TOF resolutions. The mass resolution due to the momentum and TOF resolutions can be obtained by

$$(\frac{\delta m}{m})^2 = (\beta\gamma^2)^2(\frac{\delta T_{true}}{z})^2 + (\frac{\delta p}{p})^2. \tag{4.15}$$

[4]This kind of error varies as a function of p_t, *i.e.*, 20 % at p_t = 0 - 0.02 and 15 % at p_t = 0.22 - 0.24 GeV.

Using the relation

$$\beta = \frac{p}{E} = \frac{\sqrt{E^2 - m^2}}{E} \tag{4.16}$$

with $E = \sqrt{m_K^2 + p_t^2} \cdot \cosh y$, we can estimate the width of kaon mass distribution for a given p_t and y (solid lines in Fig. 4.17 for $\delta T_{true} = 85$ ps and $\delta p/p = 2\ \% \ /\ \beta$). By fixing the width of the kaon mass distribution with these calculated values, about 10 % of the error was estimated. Therefore the overall systematic error of kaon spectra from the above sources is about 23 %.

4.2.2 Acceptance Correction

The geometrical acceptance and decay correction was determined by a Monte - Carlo simulation. Exactly the same numbers used in the data analysis for the size of the collimator opening as well as the geometry (x, y, z positions) of drift chambers, including dead beam region, have been employed in the Monte - Carlo simulation. The beam conditions measured by BVER (Table 4.2) have also been considered in the same way as in the previous section. The physics distribution of pions in RQMD was generated, and they were randomized azimuthally. The decay probability of $K^{\pm}$, ω_K, at TOFU has been calculated by

$$\omega_K = e^{-\tau_0/(\gamma \cdot \tau)} \tag{4.17}$$

where τ_0 is the time required for $v = c$ particle produced at the target to arrive at TOFU (41 ns), τ is the life time of charged kaons (12.4 ns) and γ is the

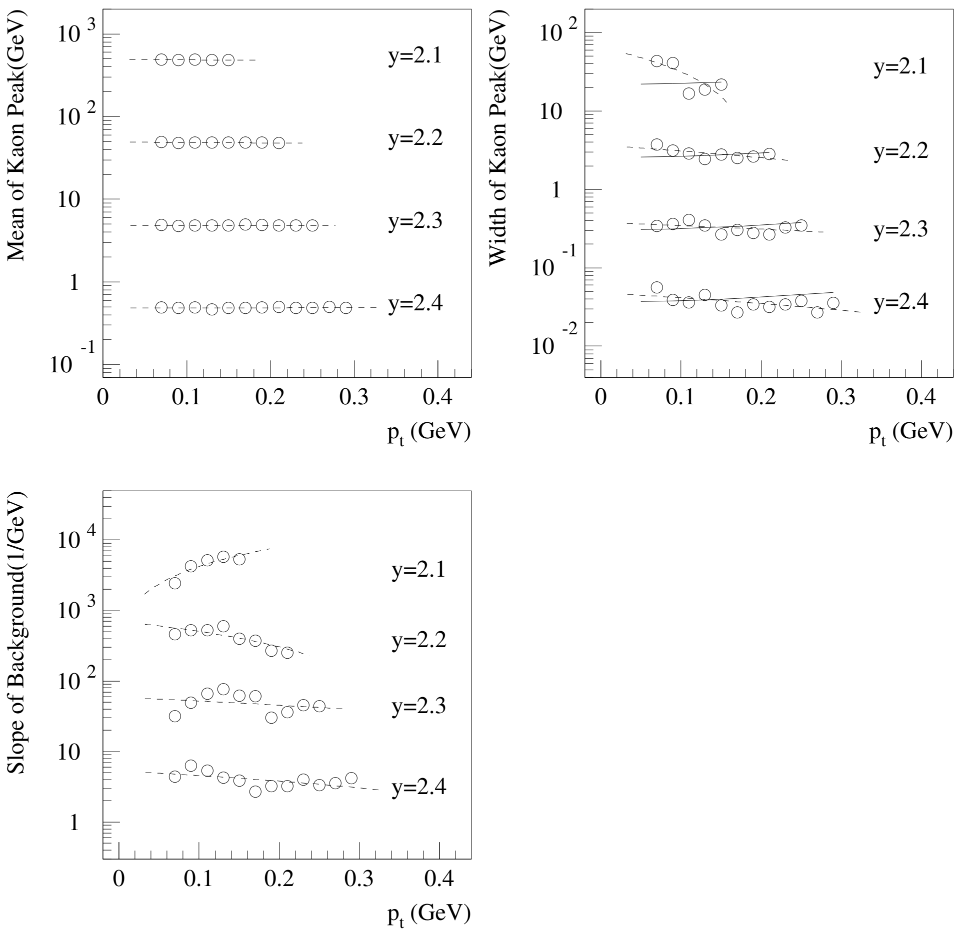

Figure 4.17: The parameters of a gaussian and an exponential function. Starting from the next to the highest rapidity, each successive rapidity bin was multiplied by the power of 10 for the clearer display. The solid lines in the width of kaon peak are the estimations due to the momentum and TOF resolutions.

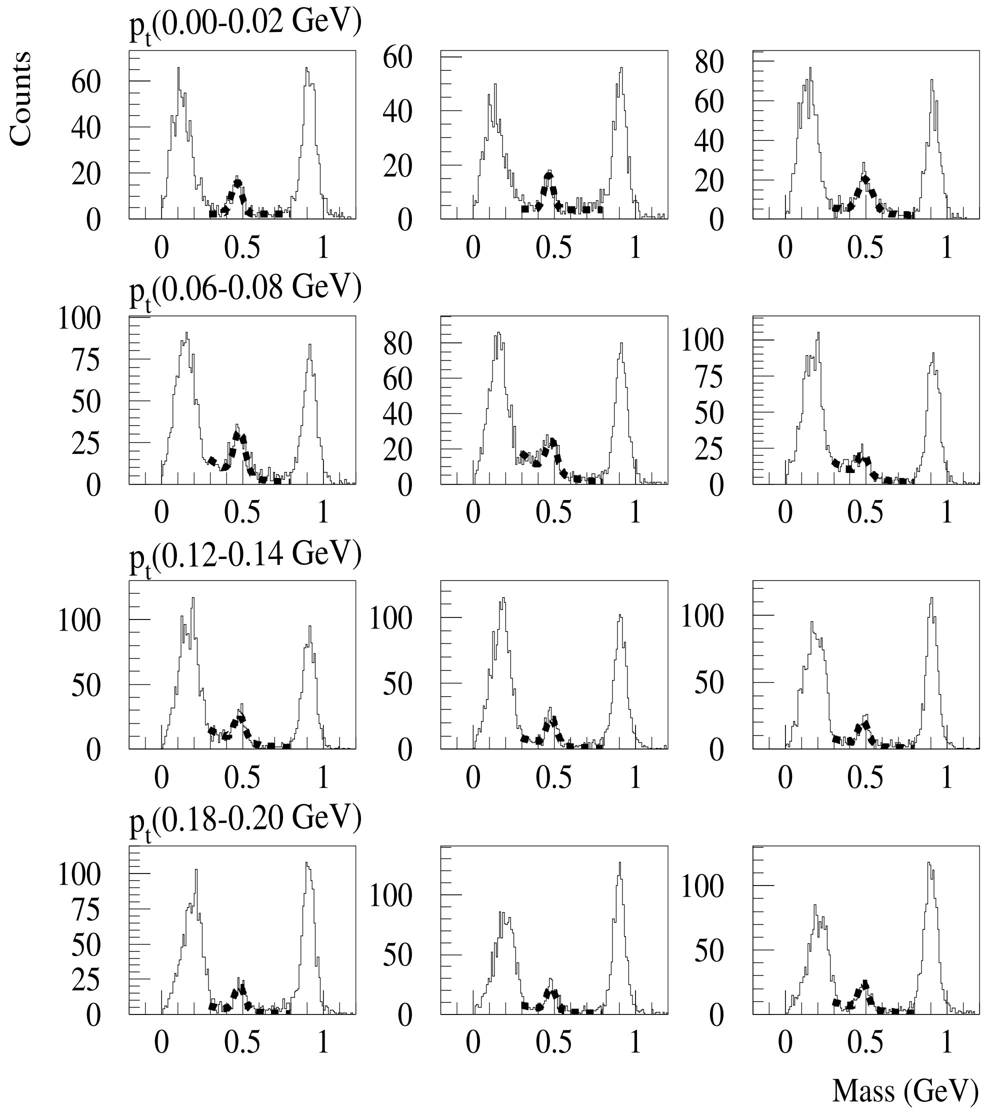

Figure 4.18: Some examples of mass fits (y = 2.3 - 2.4).

Input item(units)	Symbol	Value
Averaged Beam Angle(mrad)	$< \theta_b >$	-0.513
Beam Divergence(mrad)	σ_b	0.678
Displacement of Beam at $z = 0$(mm)	$< x >$	3.75
Sigma of $< x >$(mm)	σ_x	1.42

Table 4.2: Summary of the inputs by BVER with their notations (1993 run).

Lorentz factor obtained by

$$\gamma = \sqrt{1.0 + (\frac{p}{m_K})^2}. \tag{4.18}$$

The particle interactions in the detector material and multiple scattering, having been considered in the GEANT scheme previousely, were not simulated here. However a very detailed study of those interactions have shown that their effects were neglegible[5]. The ratio, ϵ, of the accepted and generated number of kaons for a given y and p_t sector was calculated. Figure 4.19 shows the results for several rapidities. Each bin of the measured p_t spectrum is divided by this factor.

[5]This effect was investigated by Y. Kwon.

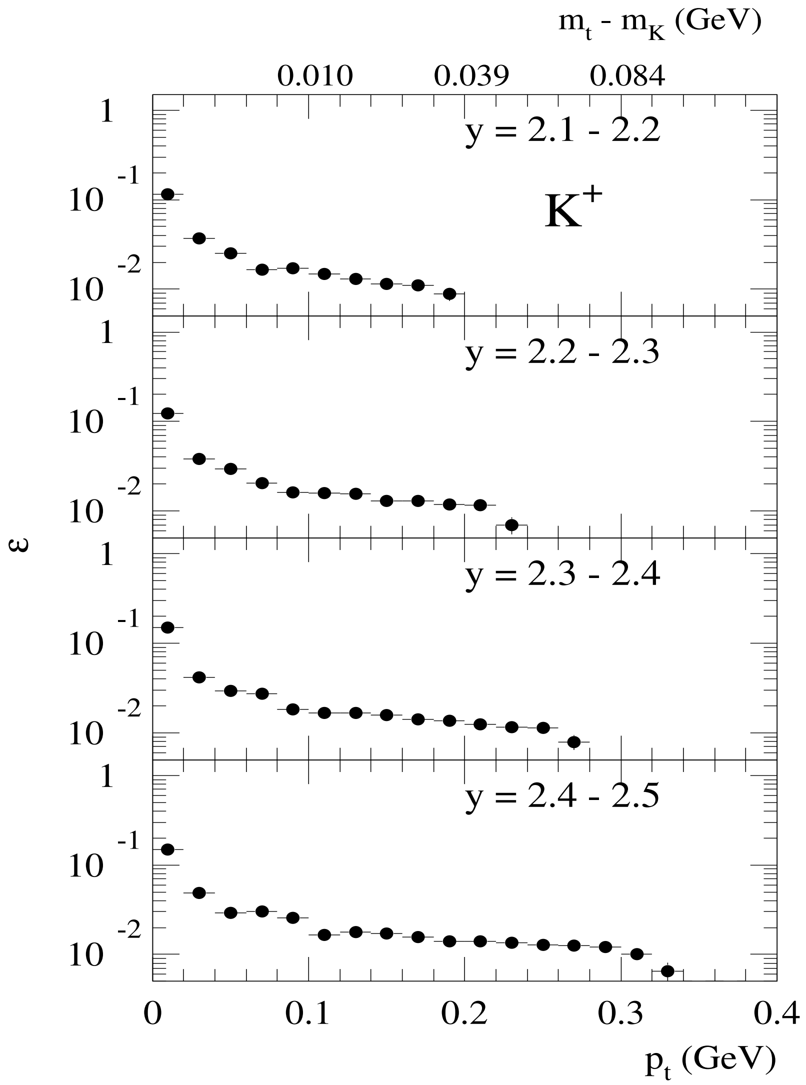

Figure 4.19: The correction factor, ϵ, for K^+ (B-field, 1993 run). The corresponding p_t range of kaon enhancement is from about 0.06 to 0.12 GeV.

Chapter 5

Results and Discussion

5.1 ^{28}Si + Pb Reaction

5.1.1 Kaon

The Boltzmann thermal spectra of kaon after the background subtraction are shown in Fig. 5.1 for both charges. The error bars are statistical only[1]. The lines in the figure represent the fit functions of data to:

$$\frac{1}{m_t^2}\frac{d^2N}{dm_t dy} = C_B \cdot exp[-\frac{m_t}{T_B(y)}] \tag{5.1}$$

where m_t is the transverse mass of kaon and $T_B(y)$ is the rapidity dependent Boltzmann temperature parameter. In such a small p_t window, all Boltzmann

[1] The relative statistical errors, considering the background, can be calculated by

$$\frac{\delta N_K}{N_K} = \sqrt{\frac{(\delta N_t)^2 + (\delta N_B)^2}{N_K^2}} = \sqrt{\frac{N_t + N_B}{N_K^2}} = \sqrt{\frac{2+P}{P \cdot N_K}} = \sqrt{\frac{2-Q}{Q \cdot N_K}},$$

where $P \equiv N_K/N_B$, $Q \equiv N_K/N_t$, $N_t = N_K + N_B$ and N_K (N_B) is the number of kaons (background).

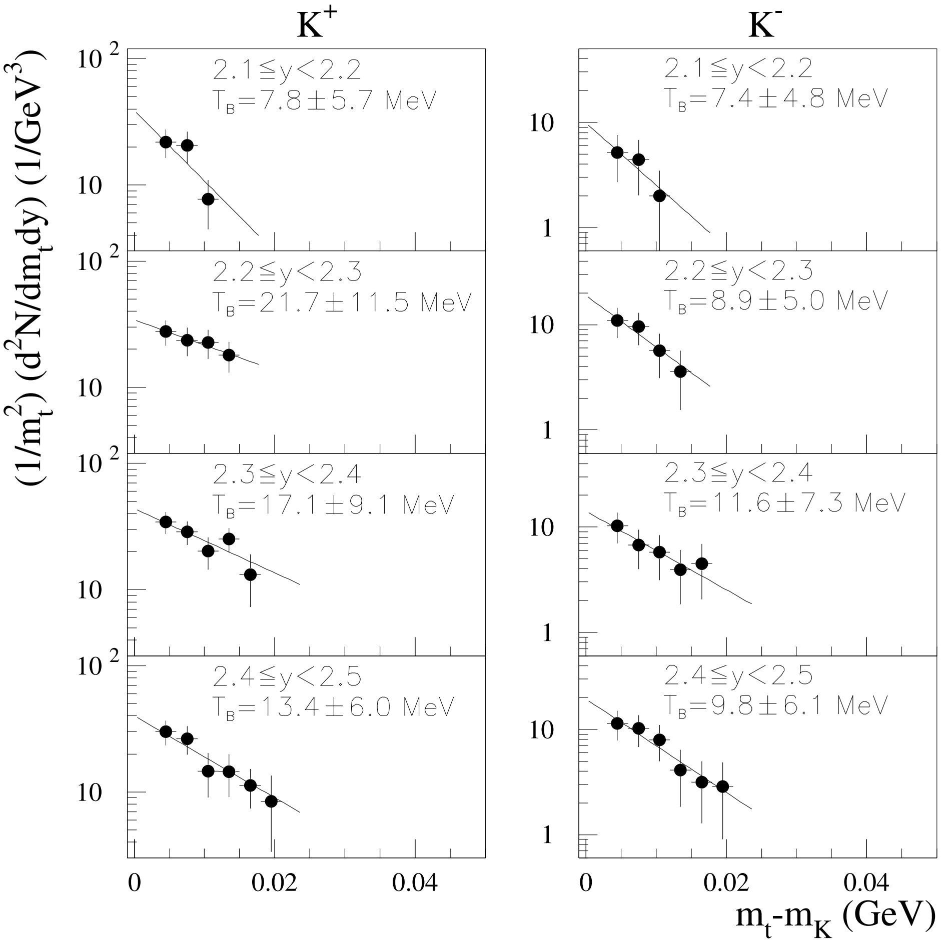

Figure 5.1: The Boltzmann thermal spectra of $K^{\pm}$ as a function of $m_t - m_K$. The error bars are statistical only.

temperatures in a forward rapidity region are below 30 MeV for both charges[2].

However we have to emphasize that there are some uncertainties in the kaon analysis of ^{28}Si induced reactions.

- First of all, the wrong position of magnet during the 1992 run narrowed the p_t coverage by more than factor of two. This pushed us to go to a higher rapidity region to obtain the temperature parameter (see Fig. 4.8).

- The time resolution of TOFU for the 1992 run ($\sigma \simeq 227$ ps) enabled us to identify kaons clearly up to about 2 GeV in momentum. However, because of the acceptace problem mentioned above, it was impossible to extract any inverse slope information for such low momenta.

- For momenta greater than 2 GeV, there exists an ambiguity for the method of background subtraction. The method we employed was based on the δT (section 4.1) distribution being close to a gaussian shape for the narrow momentum bin. But because of the nonlinearity of δT from the momentum resolution, there is always an uncertainty in our gaussian parametrization (see section 4.1.1).

- The misidentified background shape underneath the kaon peak is a big

[2]This enhancement at low p_t can not be from the background by $\pi^{\pm}$ and proton. Prof. J. Stachel has shown this fact by Monte - Carlo simulation. The pion and proton spectra with gaussian distribution in y with $\sigma_y = 0.85$ and $T_B = 150$ MeV were generated. Assuming kaon mass for all particles and look into the same rapidity window as kaon data, the temperature would be even lower, if these kinds of background exist.

uncertainty. We assumed a flat distribution, but this assumption still remains questionable (the systematic error was estimated as about 53 %).

5.1.2 Other Particles

To give more confidence to the procedure of data analysis, we analyzed data for other particles, *i.e.*, $\pi^{\pm}$, proton and deuteron. These spectra have been compared to the already existing data from the 1991 run.

The experimental setup for 1992 run had a indeed smaller opening angle than the 1991 run, as explained in chapter 2. This implies that the 1992 data have a smaller p_t coverage at low rapidities. Figure 5.2 shows the comparison of π^- Boltzmann distribution of the 1992 run with the 1991 run [35]. The agreement between these two independent experiments is remarkable including the low p_t enhancement.

The Boltzmann spectra of protons from the 1992 data are compared with the 1991 data in Fig. 5.3 [13, 14]. The p_t acceptance of the 1992 data was again much more limited compared to that of the 1991 data for $y \leq 3.2$. The agreement is reasonable except that the beam rapidity protons ($p_t \sim 0$ and $y \sim 3.4$) are not exhibited for the 1992 data because of the DC1 dead beam region.

The deuteron spectrum from the 1992 run was also analyzed. Figure 5.4 shows the mass spectra in different deuteron rapidity windows. Firstly, the proton distribution was fitted by a gaussian function and subtracted from the original mass spectra. Secondly, the deuteron peak was fitted by gaussian function again and subtracted to estimate the constant background. In this way the constant backgrounds were estimated at about 6.0 and 11.8 % for y = 1.9 and 2.1 respectively after the proper normalization. Its intercept at p_t = 0 is compared to the 1991 data [53] in Fig. 5.5. The error bars in the figure are statistical only including the background effect. Two independent analysis' of the different data sets agree well within the errors, although the centrality was a little different (8 % and 6 % of the geometrical cross section for the 1991 and 1992 data respectively). The data set for the 1992 run covers more rapidities in the geometrical acceptance.

5.1.3 Model Calculation

We have studied kaon production by a cascade model, Relativistic Quantum Molecular Dynamics (RQMD) [54]. For the calculation, the high central trigger condition on the charged particle multiplicity in the MULT acceptance ($0.8 \leq \eta \leq 4.0$) was applied. The model calculations to the Boltzmann and exponential fits for $1.8 \leq y < 2.6$ are shown in Figs. 5.6 and 5.7 for K^+ and K^- respectively. The fit was done only for relatively high p_t, corresponding to $m_t - m_K \geq 0.2$ GeV. The inverse slope parameter, T_E, of the exponential fit and dN/dy for the E859 preliminary result [55] are reasonably well reproduced by RQMD. The acceptance of E802/859 collaboration for kaon covers $m_t - m_K \geq 0.04$ GeV around mid rapidity of nucleon - nucleon system and it is quite complimentary to the acceptance of E814. It is clear that RQMD does

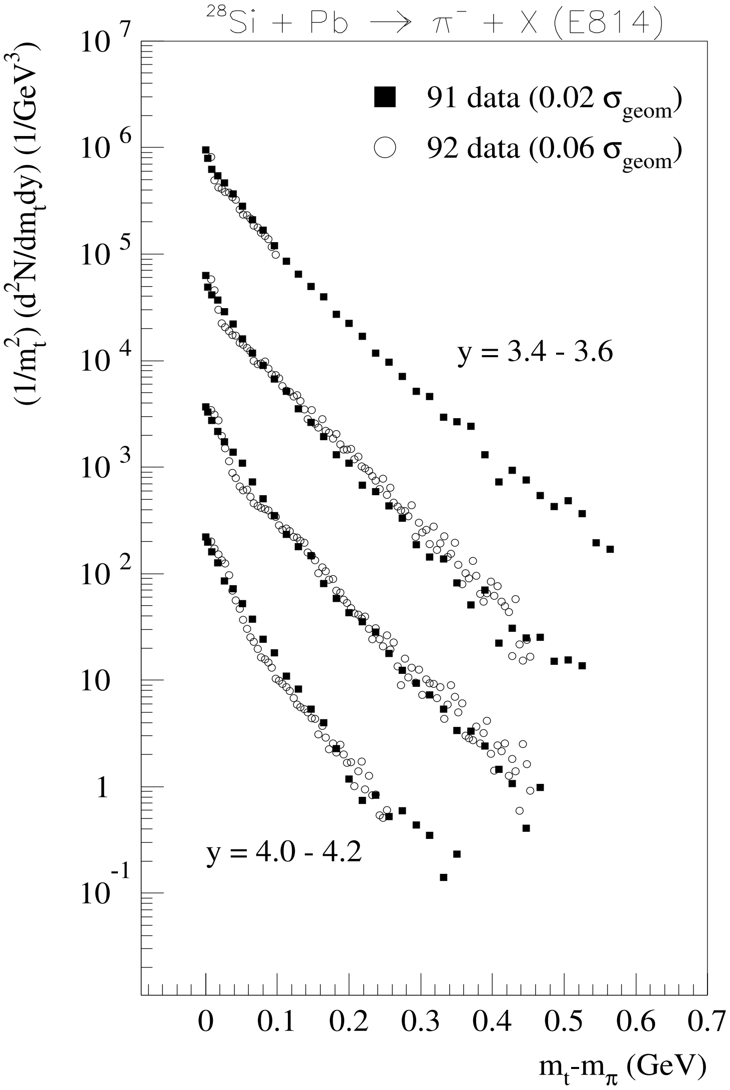

Figure 5.2: The comparison of π^- spectra in ^{28}Si + Pb collisions between the 1992 and 1991 data.

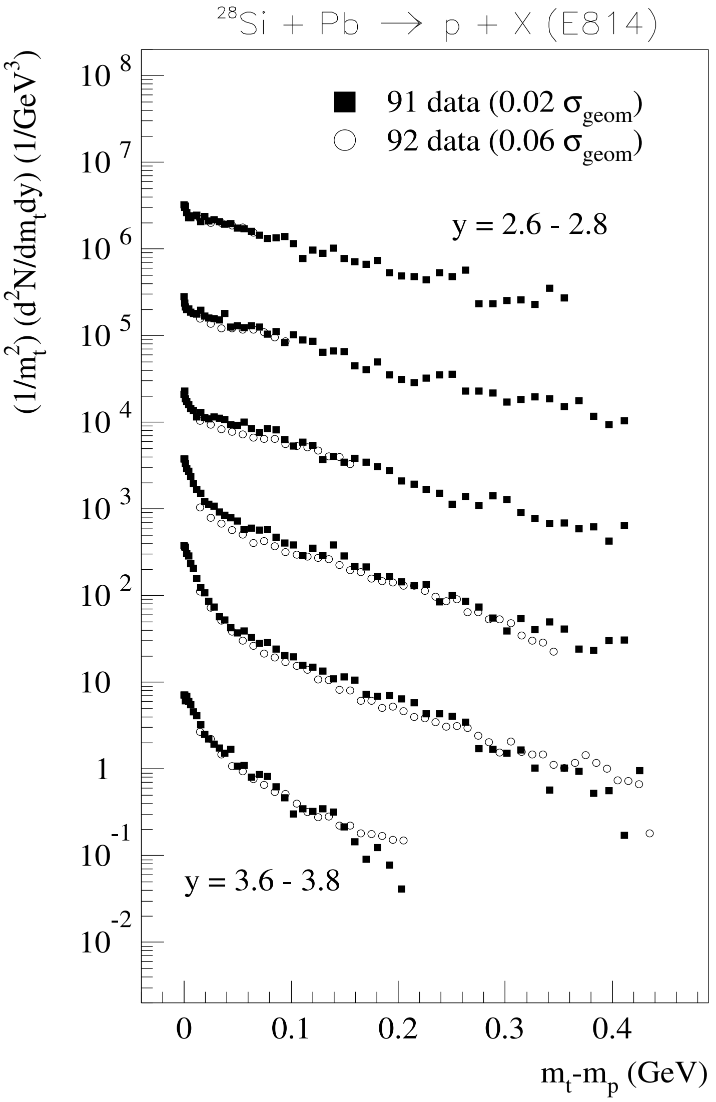

Figure 5.3: The comparison of proton spectra in ^{28}Si + Pb collisions between the 1992 and 1991 data.

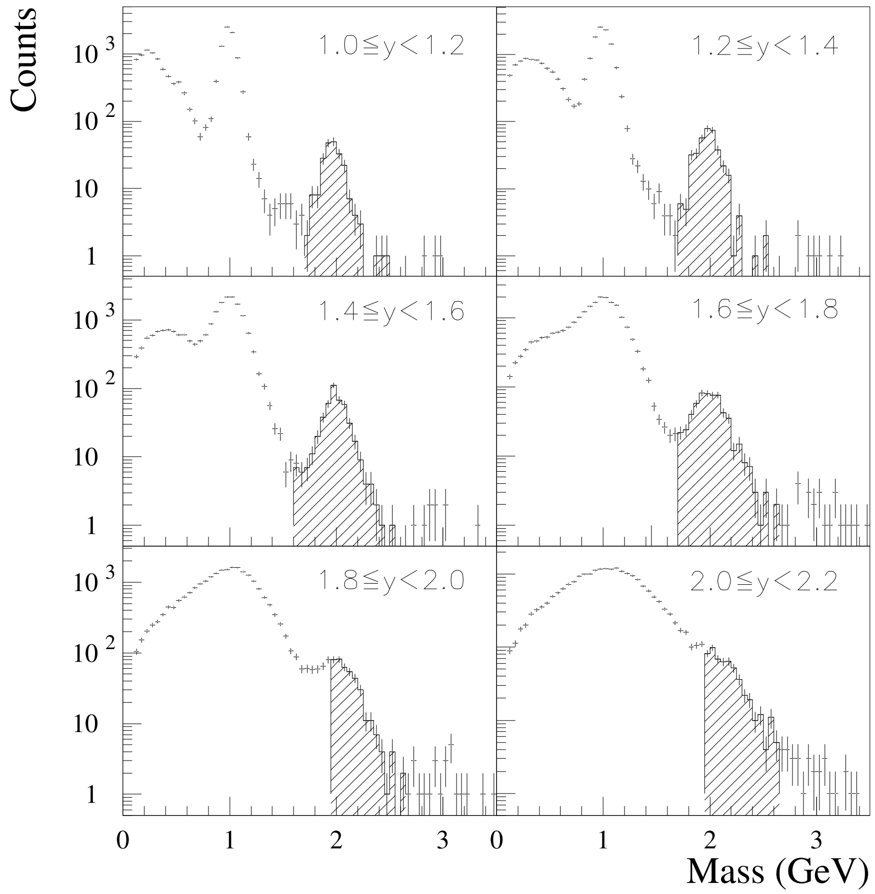

Figure 5.4: The mass spectra for several deuteron rapidity windows. The hatched area represents our deuteron samples.

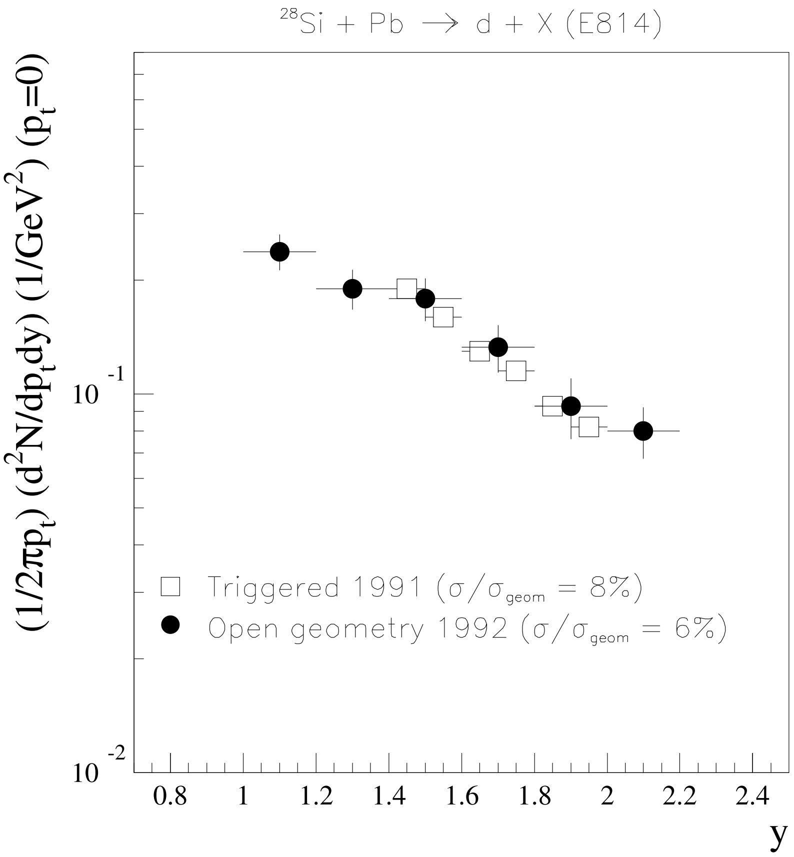

Figure 5.5: The comparison of deuteron yields at $p_t = 0$ between the 1992 and 1991 data.

not reproduce any feature of low p_t enhancement of kaon above exponential or Boltzmann thermal fit within the statistical errors.

The more detailed comparison of E814 data with RQMD at low p_t ($\leq$ 0.1 GeV) is shown in Fig. 5.8, where two rapidity bins in Fig. 5.1 are averaged, with fit lines mentioned above. We find significant enhancement of the data above the RQMD predictions for both charge kaons near zero p_t. A theory including a slow expansion velocity of a fireball and a drop of the kaon mass in the hot and dense nuclear medium could explain this enhancement quantitatively. The resonance decay is not enough to explain the size of this effect (for more details, see Appendix B).

5.1.4 Particle Ratio

Figure 5.9 shows the ratio of K^+ to K^- as a function of $m_t - m_K$. This ratio looks as if it decreases as we approach the $p_t = 0$. The ratio, however, is very close to the E859 result [55] at the relatively high p_t ($m_t - m_K \sim 0.02$ GeV) of the E814 acceptance.

In the QGP scenario, which generates the same amount of s and $\bar{\text{s}}$ quarks by pair production from gluons, K^+ is the major carrier of the $\bar{\text{s}}$ quark, and K^- carries only a fraction of the s quark, since a significant amount of s quark is used in hyperon production [56]. Based on this, the p_t dependence of K^+/K^- tells that a larger fraction of s is contained by K^- than hyperon near zero p_t.

On the other hand, the hadronic gas scenario tells that about 75 % of the K^+ are from the associated production ($pp \rightarrow p\Lambda K^+$) and other process (e.g.,

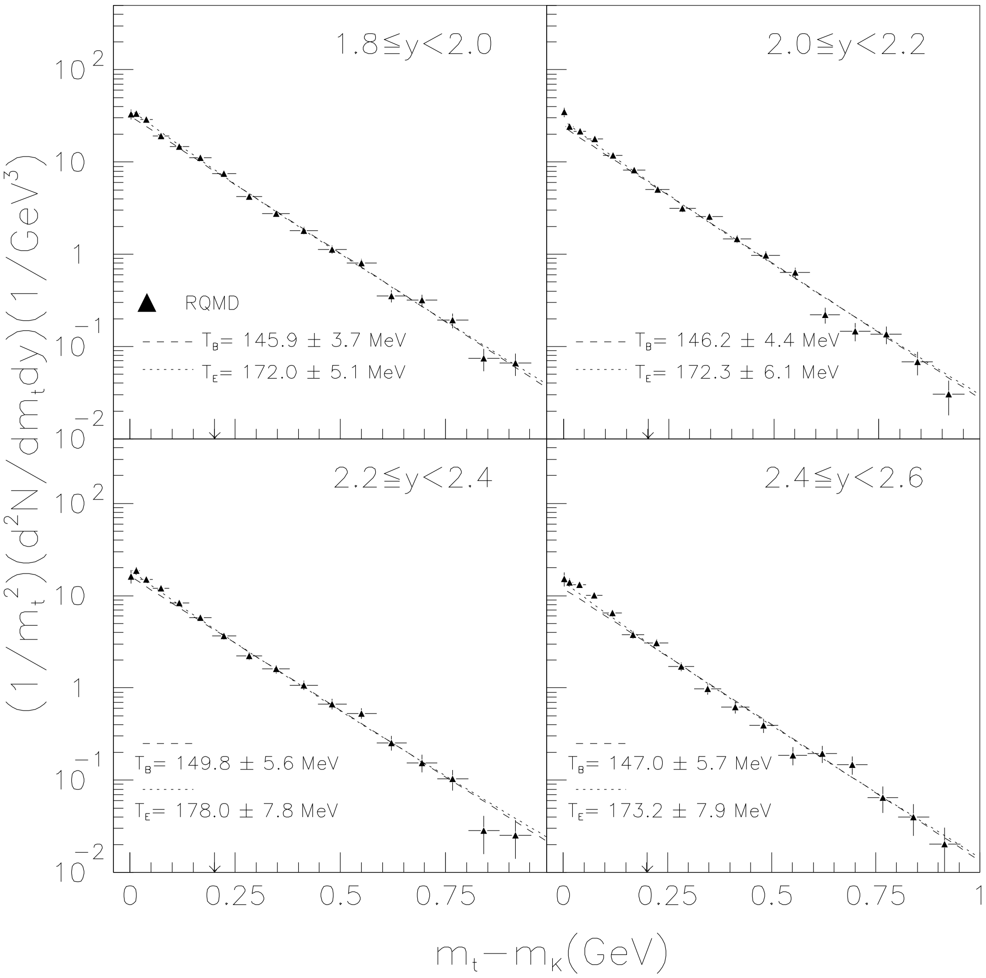

Figure 5.6: The model (RQMD) calculation of Boltzmann spectra of K^+ from ^{28}Si + Pb collisions for $1.8 \leq y < 2.6$. The Boltzmann and exponential fittings for $m_t - m_K \geq 0.2$ GeV are also shown.

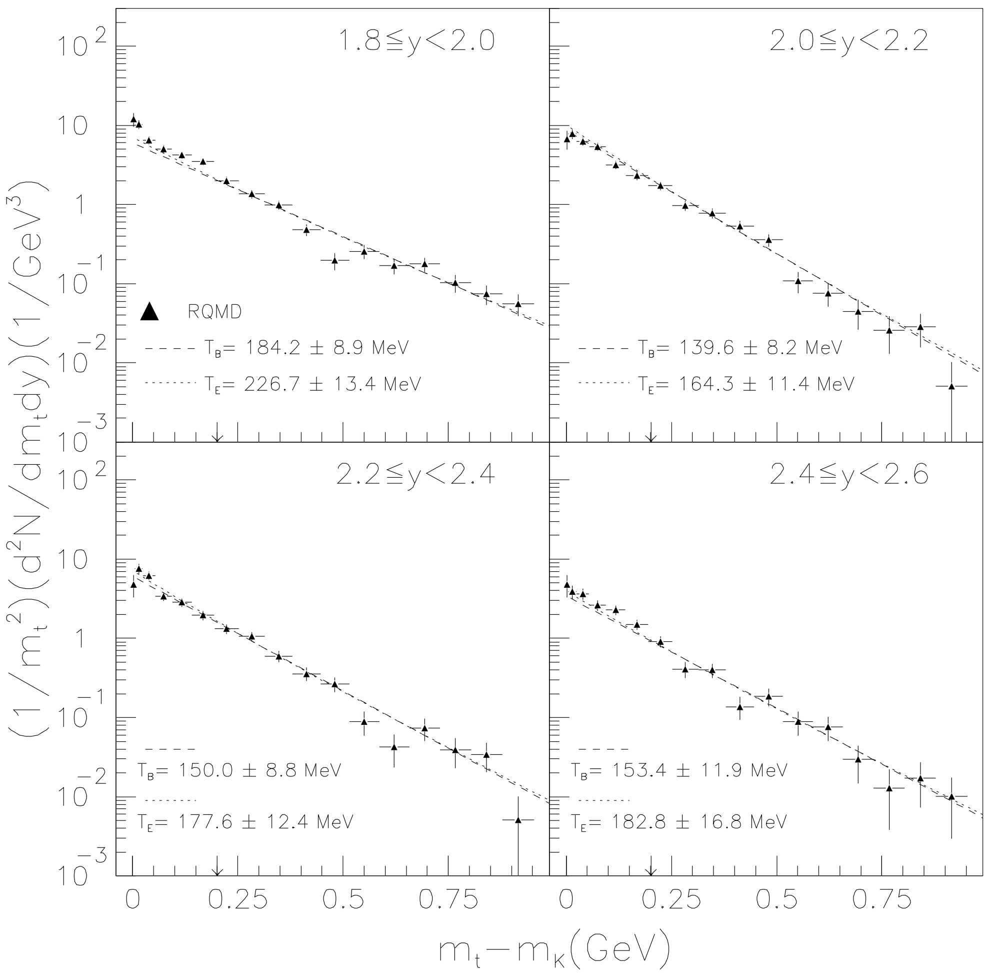

Figure 5.7: The model (RQMD) calculation of Boltzmann spectra of K^- from ^{28}Si + Pb collisions for $1.8 \leq y < 2.6$. The Boltzmann and exponential fittings for $m_t - m_K \geq 0.2$ GeV are also shown.

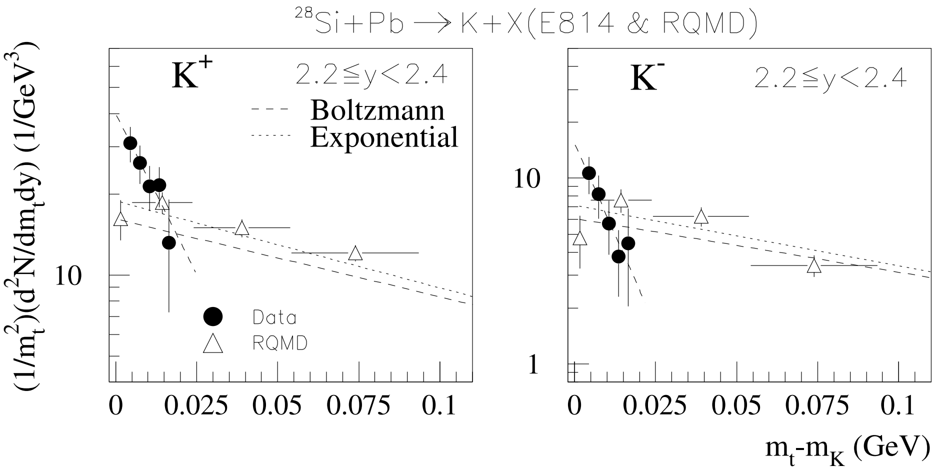

Figure 5.8: The comparison of E814 data to RQMD at low p_t for $K^{\pm}$.

$\pi N \rightarrow \Lambda K^{+}$), and about 25 % of the K^{+} are from the pair production, while all K^{-} are from pair production [55]. More K^{+} and K^{-} hadronic pair production should occur at low p_t to explain the p_t dependence of K^{+}/K^{-}. This could be another clue of the phase transition to chiral symmetry restoration.

Figure 5.10 shows the ratio of particle yield, $K^{\pm}/\pi^{\pm}$, as a function of p_t. Two dotted lines, each of them represent the lower and upper limit due to the error in temperature parameters, were calculated by the exponential fits from the E802/E859 collaboration. High p_t kaons (absolute normalization and exponential slope) are from Ref. [55] and pions are from Ref. [57]. Although the E814 data are lower than the extrapolated values from high p_t, they are in the region of approximate m_t scaling.

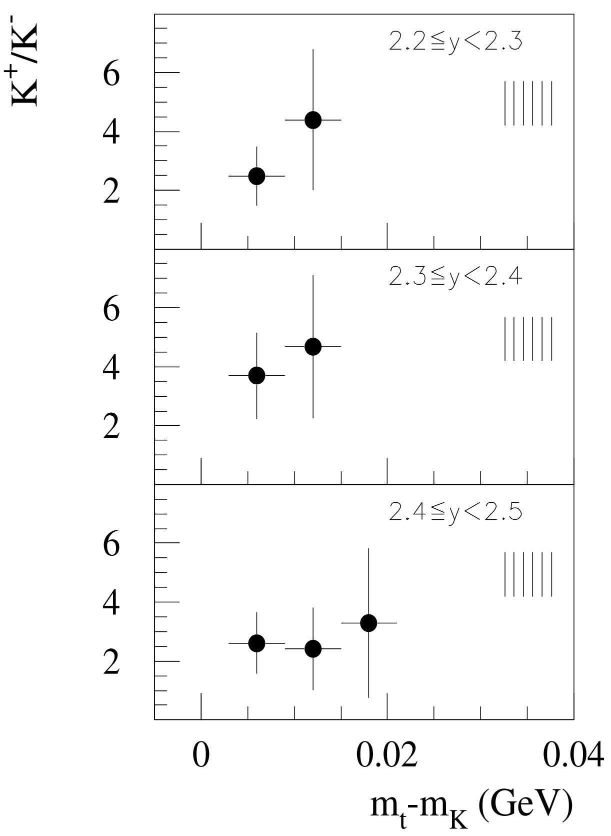

Figure 5.9: The K^+/K^- ratio as a fuction of $m_t - m_K$. The hatched area stands for 4.4 ± 0.2 which is the E802/E859 measurement integrated for $m_t - m_K \geq 0.08$ GeV. The errors are statistical only.

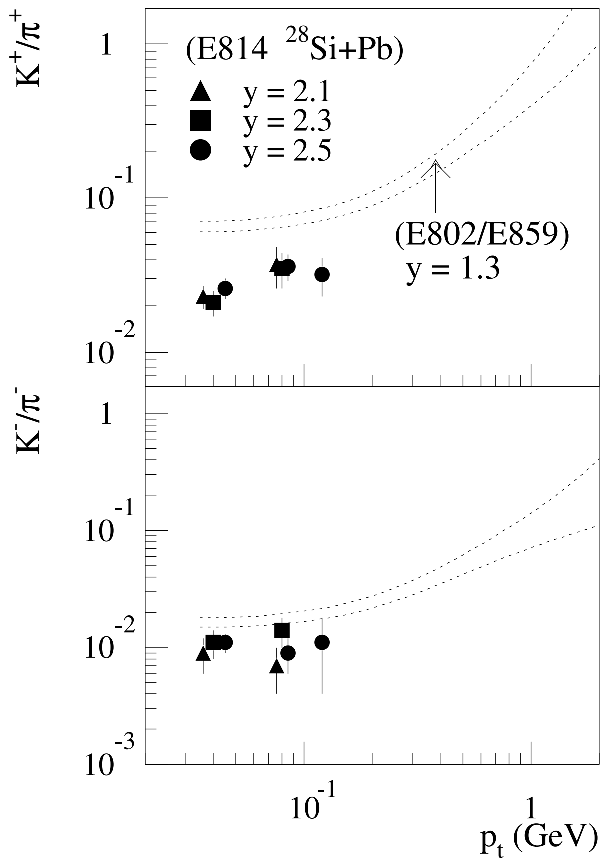

Figure 5.10: The $K^{\pm}/\pi^{\pm}$ ratio as a function of p_t. Two dotted lines represent the calculated ratios obtained from fitting E802/E859 data with exponential functions for $K^{\pm}$ and $\pi^{\pm}$. The errors are statistical only.

5.2 ^{197}Au + Au Reaction

5.2.1 Kaon

The Boltzmann spectra of K^+ are shown in Fig. 5.11. To understand the systematics, data from two field polarities are compared each other. The absence of A - field data points in $0.02 \leq p_t \leq 0.1$ GeV is due to the dead beam region of the spectrometer. The K^+ spectra with the Boltzmann fits at relatively high p_t (≥ 0.12 GeV) are shown in Fig. 5.12. The K^+ spectra at p_t ≥ 0.12 GeV follow very much a Boltzmann thermal function with temperature close to 100 MeV. Approaching low p_t, it seems to show the enhancement above the Boltzmann thermal spectra in $0.05 \leq p_t \leq 0.1$ GeV. However, K^+ yield suddenly drops near zero p_t (≤ 0.05 GeV).

The Boltzmann spectra of K^- are shown in Fig. 5.13. The K^- also shows the low p_t enhancement for less than about 0.1 GeV. However there is no dip at zero p_t within the present statistical errors. The comparison of K^+ with K^- with an equal p_t bin size (40 MeV) for y_K = 2.2 - 2.3 is shown in Fig. 5.14.

5.2.2 Pion

In order to study whether this peculiar behavior of the kaons is from a spectrometer effect, we analyzed $\pi^\pm$ in a similar momentum range as that of the kaon (2 $\sim$ 3 GeV). The results of π^+ (B - field) and π^- (A - field) are shown in Fig. 5.15. Note that pions at zero p_t in y = 3.0 - 3.7 have momentum

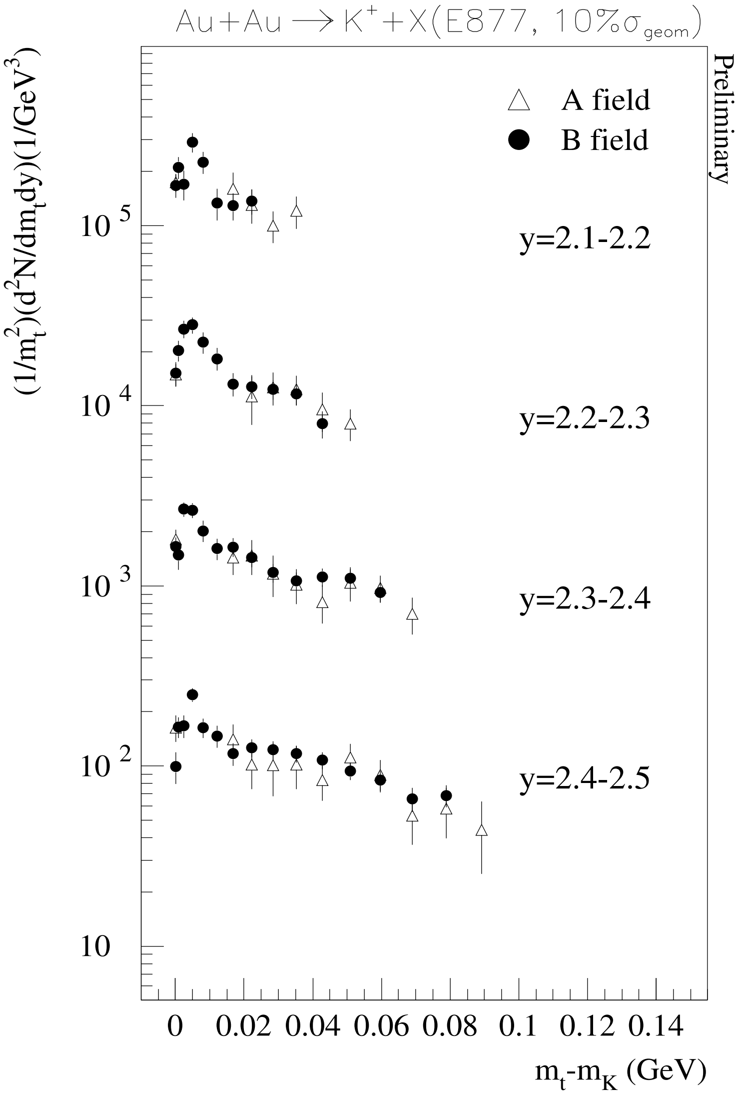

Figure 5.11: Boltzmann thermal spectra of K^+ from ^{197}Au + Au collisions. The errors are statistical only.

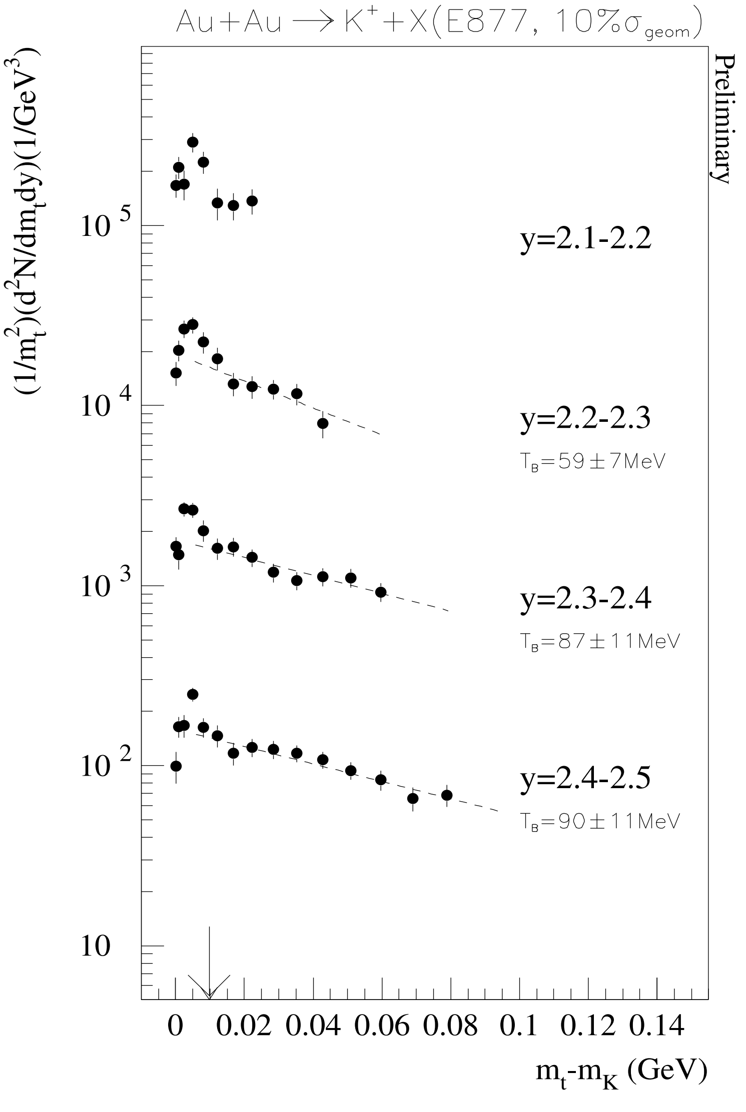

Figure 5.12: Boltzmann thermal spectra of K^+ with fitting for $p_t \geq 0.1$ GeV as indicated by an arrow.

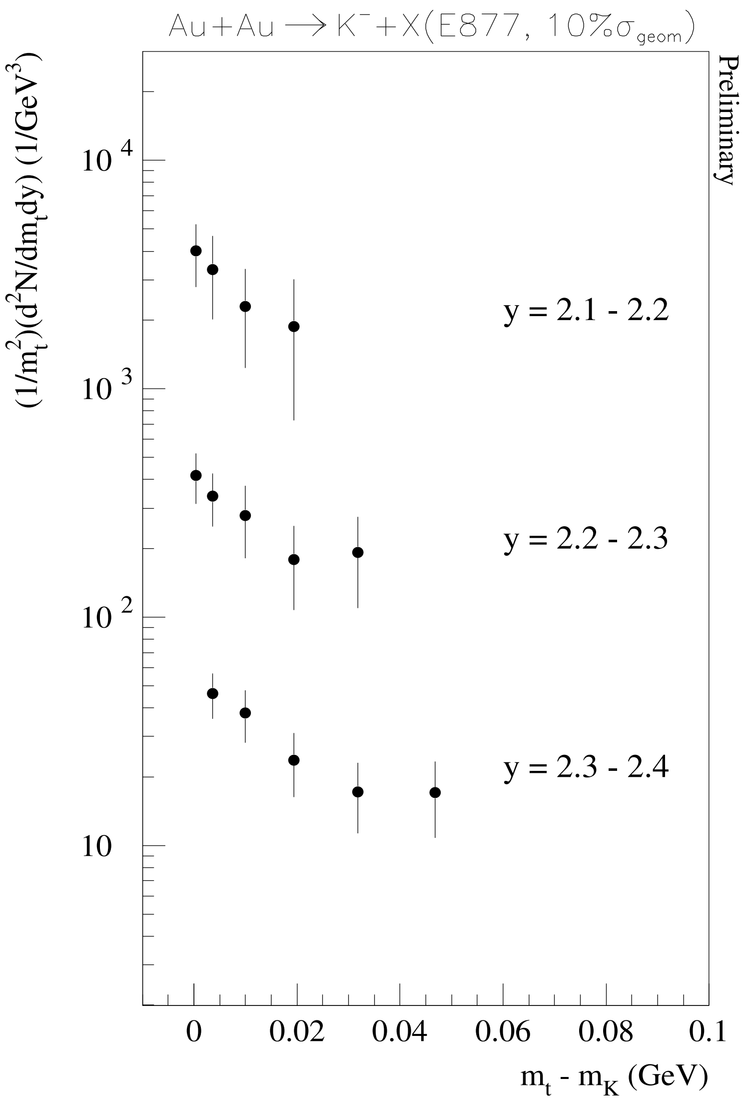

Figure 5.13: Boltzmann thermal spectra of K^- from ^{197}Au + Au collisions. The errors are statistical only.

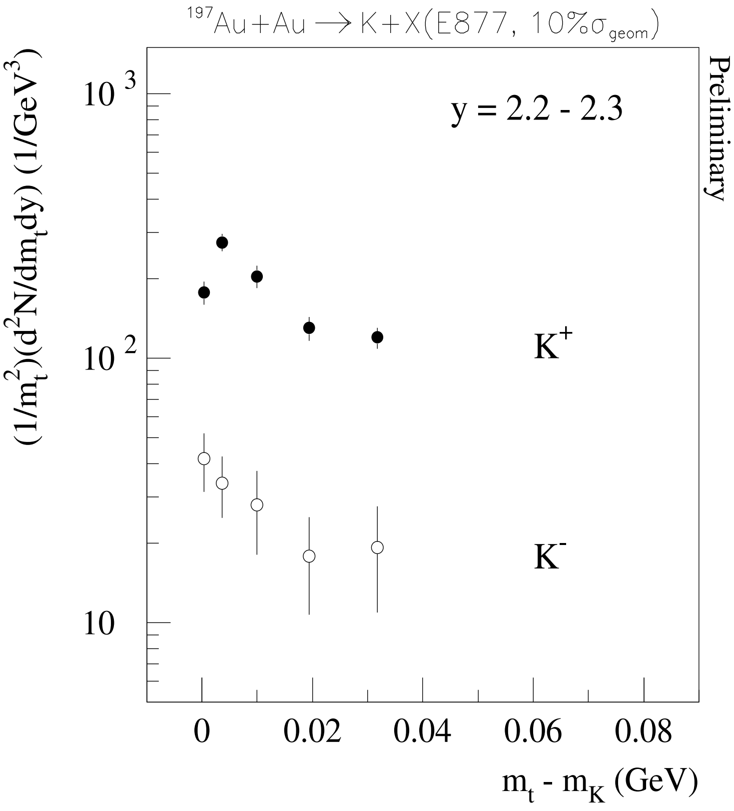

Figure 5.14: The comparison of K^+ spectrum with K^- for y = 2.2 - 2.3. The K^+ spectra were binned in equal steps as the K^- spectra for this comparison.

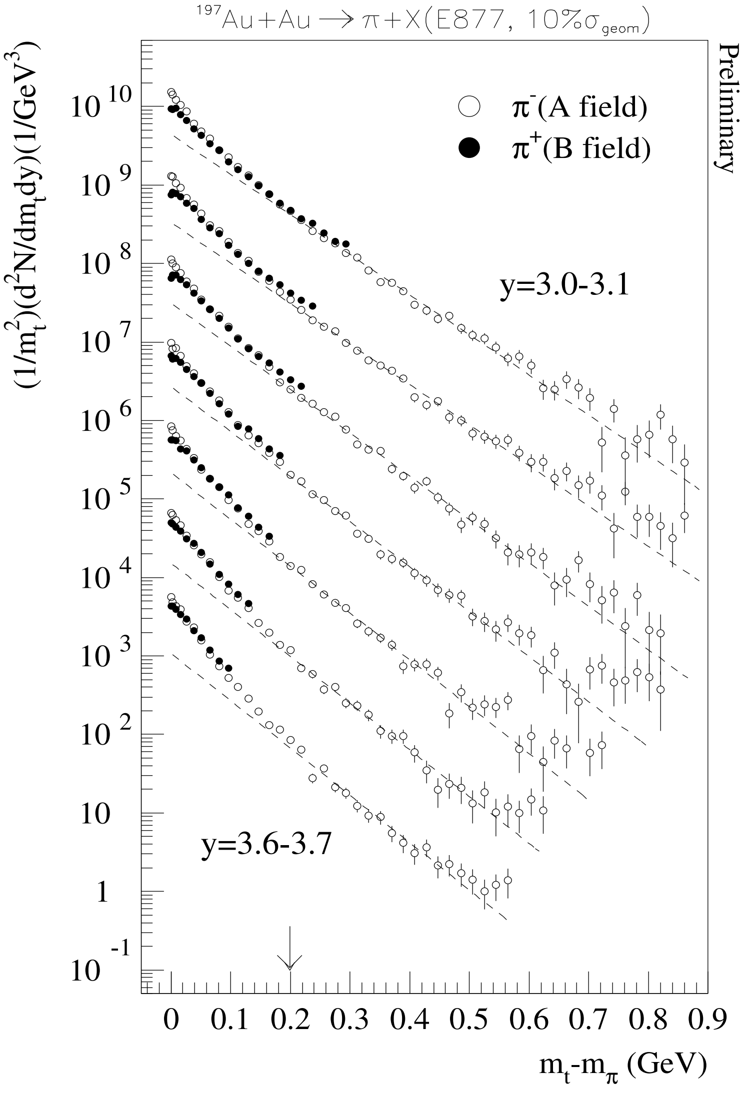

Figure 5.15: The π^- spectra (A - field) compared with π^+ (B - field). The errors are statistical only. The dashed lines are the Boltzmann fits to π^- data for $m_t - m_\pi \geq 0.2$ GeV as indicated by an arrow.

of close to that of the above discussed kaons. The dashed lines in the figure represent the Boltzmann thermal fits to π^- spectra for $m_t - m_\pi \geq 0.2$ GeV. The Boltzmann temperature parameters range from 85 MeV in $y = 3.0$ - 3.1 to 72 MeV in $y = 3.6$ - 3.7. The low p_t enhancement of both charge pions, above thermal distribution, are observed to be similar to the ^{28}Si induced collisions [35]. This effect may be explained by the resonance contents of the fireball, mainly $\Delta(1232)$, although the quantitative study is required later[3]. Moreover, we can clearly see that π^+ shows the depletion at zero p_t, while π^- shows a continuous rise toward zero p_t. Data from the other field setting confirm this phenomenon.

Considering that π^- in A - field and π^+ in B - field cover exactly the same phase space of the spectrometer, the major systematic uncertainty is from the background due to the misidentified tracks. By looking at the mass plot of each pion rapidity bin, we estimated about 8 % of systematic error for $p_t \leq 0.1$ GeV. Therefore the falloff at zero p_t may have a physics origin, e.g., Coulomb repulsion, etc. However, more detailed study is necessary, before any conclusion can be drawn.

5.2.3 Model Calculation

The kaon production as predicted by RQMD was studied for ^{197}Au + Au collisions at 10.8 A GeV. The result is for $b \leq 2$ fm, where b is the impact parameter. This condition is more central than 10% σ_{geom}. Figure 5.16 shows

[3] See appendix B.1 or Refs. [16, 17, 35].

the Boltzmann spectra of K^+ from the calculation. The dotted lines represent the fit functions for the relatively high tranverse momentum, $m_t - m_K \geq 0.1$ GeV as indicated by an arrow. RQMD does not show any feature of low p_t enhancement above a thermal shape. The Boltzmann temperature from the model ranged from 100 to 140 MeV (Fig. 5.17). Figure 5.18 shows the comparison of K^+ data[4] to the RQMD calculation in $2.2 \leq y \leq 2.4$.

[4]The K^+ data were normalized with a 70 % tracking efficiency and 80 % *mip* efficiency for the cut on TOFU pulse height.

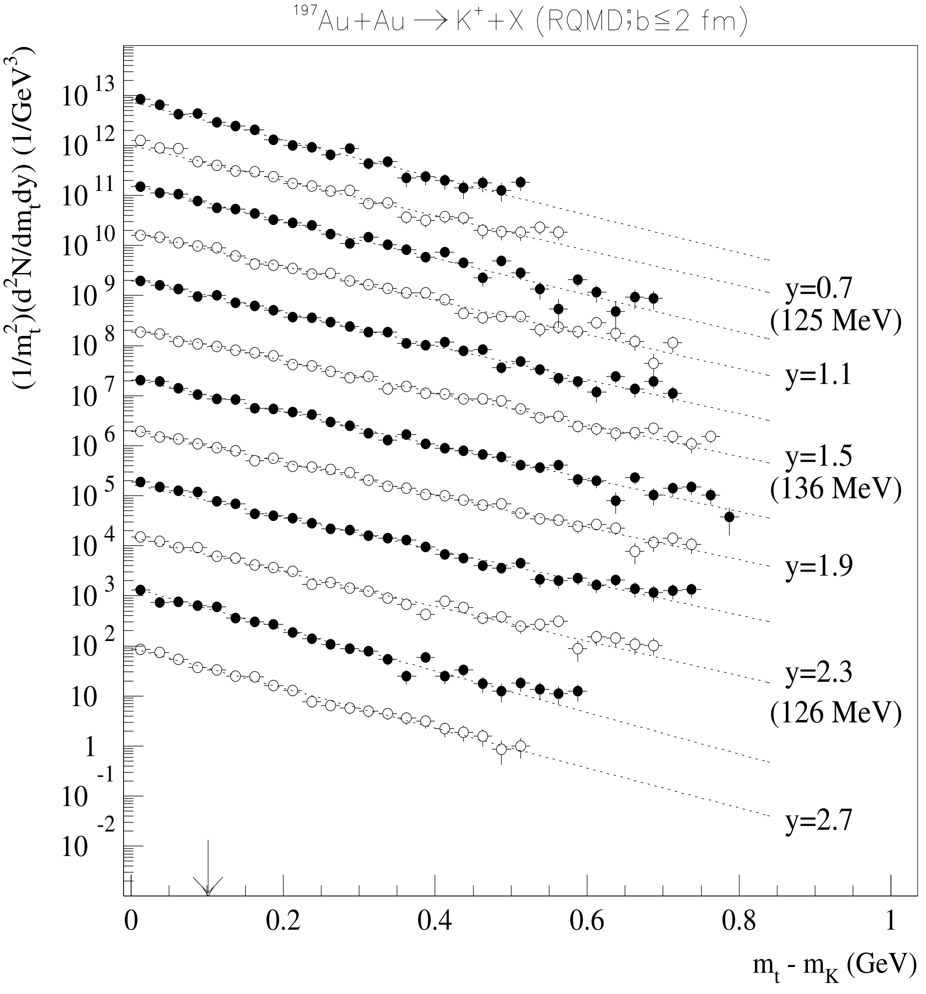

Figure 5.16: The RQMD calculation of K^+ in ^{197}Au + Au collisions. The dotted lines are the Boltzmann fits to the model calculation for $m_t - m_K \geq$ 0.1 GeV as indicated by an arrow.

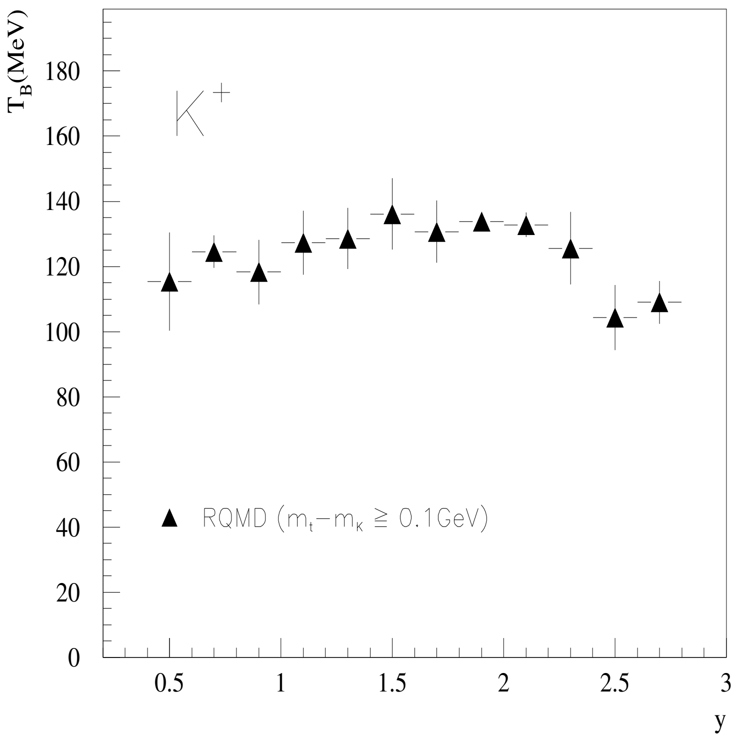

Figure 5.17: The temperature parameter extracted from K^+ spectra of RQMD.

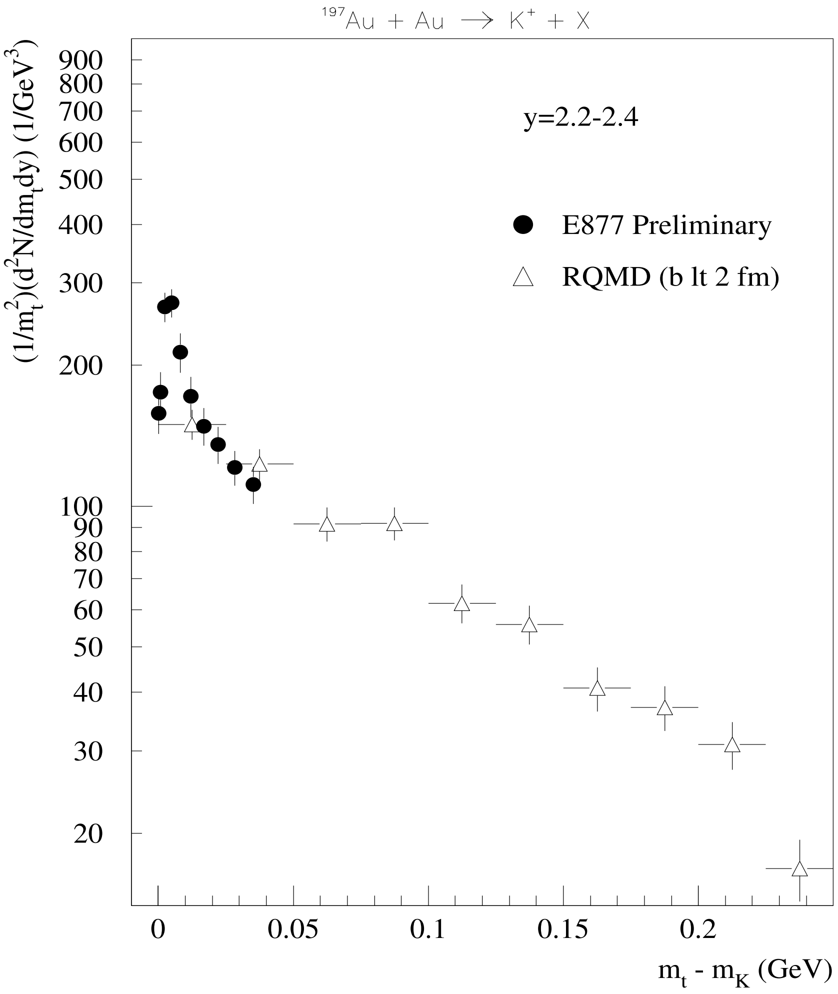

Figure 5.18: The comparison of K^+ data to RQMD in ^{197}Au + Au collisions.

Chapter 6

Conclusion

The E814/E877 collaboration at the Alternate Gradient Synchrotron at Brookhaven National Laboratory performed the experiments for measuring charged kaon production near zero p_t in the forward rapidity region utilizing the 14.6 A GeV ^{28}Si and 10.8 A GeV ^{197}Au beams.

The transverse momentum spectra of kaons for central ^{28}Si + Pb collisions show steep increases near zero p_t above the pure thermal Boltzmann distributions, albeit measured only with a small acceptance and low resolution time measurement. For ^{28}Si + Pb reactions, both charged kaons represent similar enhancement with the Boltzmann temperature less than 30 MeV. This result can be compared to 150 MeV measured by the E802/E859 collaboration at higher p_t.

The result of K^+ for ^{197}Au + Au collisions, taken with much higher resolution and over a larger acceptance in p_t, shows a steep increase near zero p_t, but a depletion at zero p_t. However K^- shows a continuous rise to zero p_t and no dip within the present statistical errors.

This low p_t enhancement of kaon spectra is very surprising and not at all explained with the current event generators, *i.e.*, ARC and RQMD, or our thermal model.

The difference between positive and negative charge kaon spectra at zero p_t may be due to Coulomb potential, although a detailed calculation for this effect would be complicated. The quantitative prediction may be related to the other parameters, *i.e.*, expansion velocity, etc. However our conjecture is supported by the pion spectra. A similar difference between π^+ and π^- was also shown by this experiment.

The presence of medium effects during the high compression phase of the collision may explain the low p_t enhancement of kaons. The thermal model including a very slow expansion velocity and mass reduction, due to the reduced vector potential, could explain the kaon spectrum for ^{28}Si + Pb interactions (see Appendix B.2).

Future analysis needs to concentrate on the centrality dependence of kaon spectra, as well as the development of the pattern recognition code to reduce wrongly reconstructed tracks. Moreover, it will be also interesting to study the correlation between the observed low p_t enhancement and reaction plane.

Bibliography

[1] A. Chodos, R. L. Jaffe, K. Johnson and C. B. Thorn, Phys. Rev. **D10**, 2599(1974).

[2] W. Weise, Quarks and Nuclei, International Review of Nuclear Physics-vol. 1 (World Scientific Publishing Company, 1984).

[3] D. H. Perkins, Introduction to High Energy Physics (3rd edition), (Addison - Wesley Publishing Company, Inc., 1987).

[4] E. V. Shuryak, Phys. Rep. **61**, 71(1980).

[5] H. Satz, Ann. Rev. Nucl. & Part. Sci. **35**, 245(1985).

[6] M. Jacob, The Quark Structure of Matter, World Scientific Lecture Note in Physics-vol. 50 (World Scientific Publishing Company, 1992).

[7] M. Cruetz, Quarks, Gluons and Lattices (Cambridge University Press, 1983).

[8] U. Heller and F. Kersch, Nucl. Phys. **B251**, 254(1985).

[9] T. Cerik, J. Engels and H. Satz, Nucl. Phys. **B256**, 670(1985).

[10] S. Gottlieb, W. Liu, D. Toussaint, R. L. Rewken and R. L. Sugar, Phys. Rev. **D35**, 3972(1987).

[11] F. R. Brown, F. P. Butler, H. Chen, N. H. Christ, Z. Dong, W. Schaffer, L. I. Unger and A. Vaccarino, Phys. Rev. Lett. **65**, 2491(1990).

[12] F. Halzen, Nucl. Phys. **A461**, 181c(1987).

[13] J. Barrette et al. , E814 Collaboration, Z. Phys. **C59**, 211(1993).

[14] J. Barrette et al. , E814 Collaboration, Phys. Rev. **C50**, 3047(1994).

[15] J. Dee, Ph. D. Thesis, State University of New York at Stony Brook, 1995.

[16] J. Stachel et al. , E814 Collaboration, Nucl. Phys. **A566**, 183c(1994).

[17] P. Braun-Munzinger, E814/877 Collaboration, Proc. NATO Advanced Study Institute on "Hot and Dense Nuclear Matter", Bodrum, Turkey, Oct. 1993, W. Greiner, H. Stöcker and A. Gallmann, eds. (Plenum, New York, 1994) p. 419.

[18] G. Bertsch, B. Mueller, J. Negele, J. Friar, F. Iachello, S Koonin and V. Pandharipande, The summary of the nuclear theory town meeting at Argonne National Laboratory; nucl - th/ 9502035 (1995).

[19] G. E. Brown, Nucl. Phys. **A522**, 397c(1991).

[20] G. E. Brown, H. Müther and M. Prakash, Nucl. Phys. **A506**, 565(1990).

[21] G. E. Brown, C. M. Ko, Z. G. Wu and L. H. Xia, Phys. Rev. **C43**, 1881(1991).

[22] T. Hatsuda and T. Kunihiro, Phys. Lett **B185**, 304(1987).

[23] V. Bernard, U. Meissner and I. Zahed, Phys. Rev. Lett. **59**, 966(1987).

[24] X. S. Fang, C. M. Ko, G. E. Brown and V. Koch, Phys. Rev. **C47**, 1678(1993).

[25] R. Pisarski and F. Wilczek, Phys. Rev. **D29**, 338(1984).

[26] G. E. Brown, Phys. Rep. **163**, 167(1988).

[27] D. B. Kaplan and A. E. Nelson, Phys. Lett. **B175**, 57(1986).

[28] A. E. Nelson and D. B. Kaplan, Phys. Lett. **B192**, 193(1987).

[29] G. E. Brown, K. Kubodera and M. Rho, Phys. Lett. **B192**, 273(1987).

[30] K. S. Lee and U. Heinz, Z. Phys. **C43**, 425(1989).

[31] K. S. Lee, U. Heinz and E. Schnedermann, Z. Phys. **C48**, 525(1990).

[32] E. V. Shuryak, Phys. Rev. **D42**, 1764(1990).

[33] E. V. Shuryak, Nucl. Phys. **A533**, 761(1991).

[34] E. V. Shuryak and V. Thorsson, Nucl. Phys. **A536**, 739(1992).

[35] J. Barrette et al. , E814 Collaboration, Phys. Lett. **B**, (1995) in print.

[36] G. E. Brown, J. Stachel and G. M. Welke, Phys. Lett. **B253**, 19(1991).

[37] J. Sollfrank, P. Koch and U. Heinz, Z. Phys. **C52**, 593(1991).

[38] W. A. Love et al. , E810 Collaboration, Nucl. Phys. **A525**, 601c(1991).

[39] L. Waters, Ph. D. Thesis, State University of New York at Stony Brook, 1990.

[40] J. Barrette et al. , E814 Collaboration, Phys. Rev. **C46**, 312(1992).

[41] J. Simon-Gillo et al. , Nucl. Inst. Meth. **A309**, 427(1991).

[42] D. Fox et al. , Nucl. Inst. Meth. **A317**, 474(1992).

[43] R. Debbe et al. , IEEE Trans. Nucl. Sci. **37**, 88(1990).

[44] J. Fischer et al. , IEEE Trans. Nucl. Sci. **37**, 82(1990).

[45] S. V. Greene, Ph. D. Thesis, Yale University, 1992.

[46] M. Fatyga, D. Makowiecki and W. J. Llope, Nucl. Inst. Meth. **A284**, 323(1989).

[47] P. Braun-Munzinger, B. Hong, Y. Kwon, S. Panitkin, J. P. Wessels and Y. Zhang, E877 Note #1, Jan. 1994.

[48] 1992 Research Instrumentation Catalog, LeCroy Corporation, 1991.

[49] G. David, private communication.

[50] A. Peisert and F. Sauli, preprint, CERN 84-08, 1984.

[51] R. Brun et al. , GEANT 3.11 User's Guide, CERN Data Handling Division Report No. DD/EE/84-1, Sept., 1987.

[52] CERN Computer Center Program Library User's Manual, 1989.

[53] J. Barrette et al. , E814 Collaboration, Phys. Rev. **C50**, 1077(1994).

[54] H. Sorge, R. Mattiello, A. Jahns, H. Stöcker and W. Greiner, Phys. Lett. **B271**, 37(1991).

[55] T. Sung, E859 Collaboration, Proceedings of HIPAGS 93', MITLNS-2158, 230(1993).

[56] P. Koch, B. Müller and J. Rafelski, Phys. Rep. **142**, 167(1986).

[57] H. Hamagaki et al. , E866 Collaboration, Nucl. Phys. **A566**, 27c(1994).

[58] H. Fesefeldt, Th. Hamacher and J. Schug, Nucl. Instrum. & Methods **A292**, 279(1990).

[59] A. Shor and R. Longacre, Phys. Lett. **B218**, 100(1989).

[60] P. Braun - Munzinger, J. Stachel, J. P. Wessels and N. Xu, Phys. Lett. **B344**, 43(1995).

[61] P. Braun-Munzinger, private communication.

[62] C. Parsons, E802 Collaboration, Proceedings of HIPAGS 93', MITLNS-2158, 72(1993).

[63] A. C. Saulys, E810 Collaboration, Proceedings of HIPAGS 93', MITLNS-2158, 196(1993).

[64] T. Schlagel, S. H. Kahana and Y. Pang, Phys. Rev. Lett. **69**, 3290(1992).

[65] V. Koch, preprint, SUNY - NTG 94 - 26; hep - ph/ 9405022 (1994).

[66] G. E. Brown and M. Rho, preprint, SUNY - NTG 94 - 44; hep - ph/ 9408223 (1994).

Appendix A

GEANT simulation of PCAL

Computer simulation of shower development by Monte - Carlo technique on the basis of event by event tracking in the PCAL of E814 was performed. The comparison of the simulation results to experimental data leads us to refine our understanding of PCAL performance in the GEANT frame. The angle dependence of shower leakage of electromagnetic and hadronic showers from PCAL was studied and compared to the result of fast Monte - Carlo (PROPHET) simulation.

A.1 Introduction

The Monte - Carlo simulation of shower development in PCAL, based on event by event tracking, was originally desired as a benchmark solution, because it is the most similar way to the real sampling calorimeter performance. Since we have several sets of experimental data for normal incident projectiles such as electrons, pions and protons, we can compare the results of

Monte - Carlo simulation to experimental ones regarding energy deposition. In addition to that it is also possible, in the simulation, to send particles with polar angle, which we can not do in the real experiment. From this kind of calculation we can study the shower leakage effects in great detail. One major effort may be put into finding energy correction factors including shower leakage effects. Once these factors are determined, we may in principle try to deduce the true physical quantities from the experimental data. However we can not avoid any model dependence for these sorts of study.

One problem of the Monte - Carlo simulation based on event by event tracking is that it is a very time consuming job. For this reason PROPHET, the fast Monte - Carlo simulation based on the shower parameterization, has been studied in parallel. Although the present PROPHET calculation gives a reasonable agreement with experimental data, the parameters of PROPHET should be adjusted further by simulation results, based on event by event tracking for the projectiles on a slant. This is another purpose of this study.

Our Monte - Carlo study is in the GEANT [51] frame. All of the physics processes for the shower development are based on EGS4 [51] for electromagnetic interactions and GHEISHA [58] for hadronic interactions.

The remaining of this appendix will be the following. Section 2 shows the comparison of the simulation results with secondary beam (SEB) experimental data for electromagnetic and hadronic showers in PCAL. This is only the case for normally incident projectiles on the calorimeter. The optimization of tracking thresholds for saving computing time is also explained there. Section 3 has the effects of shower leakage. When the several incident particles were sent into the calorimeter with some polar angle, there must be a significant shower leakage at outer towers, especially for hadronic showers. The details of them and comparison with PROPHET are explained. Section 4 shows the connection with the real physics event generator, HIJET with rescattering. Conclusion follows in section 5.

A.2 Understanding of Calorimeter Response

By sending several particles at different energies into the tower normally, we can compare our results with the data analysis of SEB runs. And the comparison with the results of the PROPHET calculation is also interesting.

A.2.1 Electromagnetic Showers

We used electrons to simulate the electromagnetic showers in the participant calorimeter. Electrons at several different beam energies were sent into PCAL normally. We calibrated the calorimeter with 5.65 GeV electrons. As a result, we determined the sampling fraction as 2.70 % which is a little lower than the 2.76 % from the analysis of two SEB runs, March 89 and April 90 [41]. According to the above reference, the sampling fraction also varies with beam energy. We can however ignore this effect, since the variation is negligible.

For the study of electromagnetic showers we considered the plate to plate fluctuation of the response for each scintillator. Because the size of an electromagnetic shower is small, all the properties, like energy deposition and energy resolution etc. , are very sensitive to this fluctuation. For example, the total energy deposition of 5.65 GeV electrons in different towers along x axis shows a large fluctuation due to the large plate to plate response of the EM sectors (Fig. A.1). Data as well as calculation show that tower (3,16), (5,16) and (7,16) respond reasonably, but others return rather lower energy deposition. Therefore we have to keep this in mind, especially for electromagnetic showers later.

The signal linearity due to electrons with the beam energy in tower (5,16), the most reliable tower as can be seen by Fig. A.1, is shown in Fig. A.2. Because there were no shower leakages for electromagnetic showers even for 14.6 GeV e^-, we expected a perfect linear relation. But the simulation results were lower than the linear line for relatively high energies above 10 GeV. We inferred that this was an effect from the poor scintillator responses of neighbor towers of (5,16). The fraction of the energy deposited in each module looks very reasonable. Table A.1 summarizes the comparison of the present simulation with available experimental data and PROPHET [41, 42].

A.2.2 Hadronic Showers

We also acquired reasonable total energy depositions for hadrons. The responses of calorimeter for pions and protons on tower (5,16) are shown in Figs. A.3 and A.4 respectively. Fig. A.3 represents the simulation for a π^- projectile, except for 1.56 and 2.46 GeV which are for π^+. For low energy pions the calculation showed about the total beam energy. But for the beam energies above 10 GeV, the calculation returned an energy much

p_{beam} (GeV)	Module	Exp. (%)	PROPHET (%)	Present (%)
1.56	EM1	90.		89.1
	EM2			10.6
	HD1			0.3
2.46	EM1	88.		86.7
	EM2			12.6
	HD1			0.7
4.00	EM1			85.8
	EM2			13.2
	HD1			1.0
5.65	EM1	84.	88.71	80.3
	EM2		11.38	18.6
	HD1		0.3	1.1
10.0	EM1			80.4
	EM2			18.1
	HD1			1.5
14.6	EM1			77.3
	EM2			20.9
	HD1			1.8

Table A.1: The energy deposition (in %) of each module for e^- at the different beam momenta.

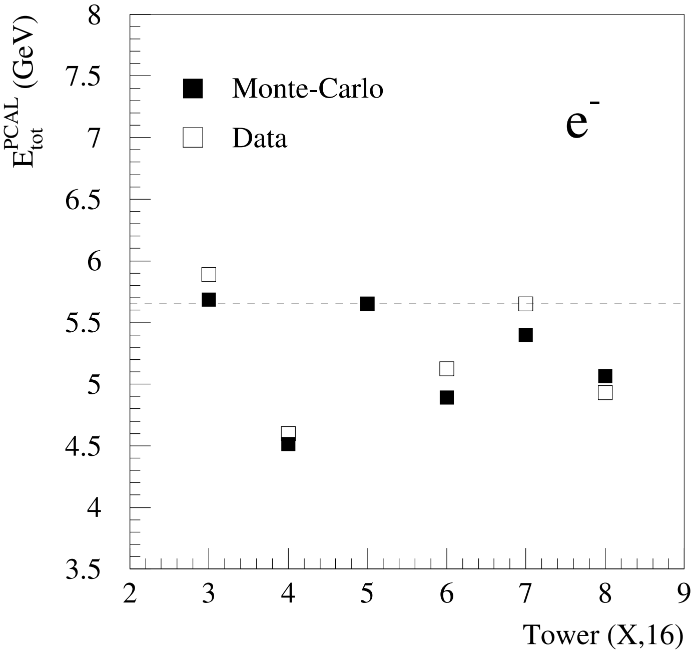

Figure A.1: Tower to tower variation of total energy deposition for 5.65 GeV e^-.

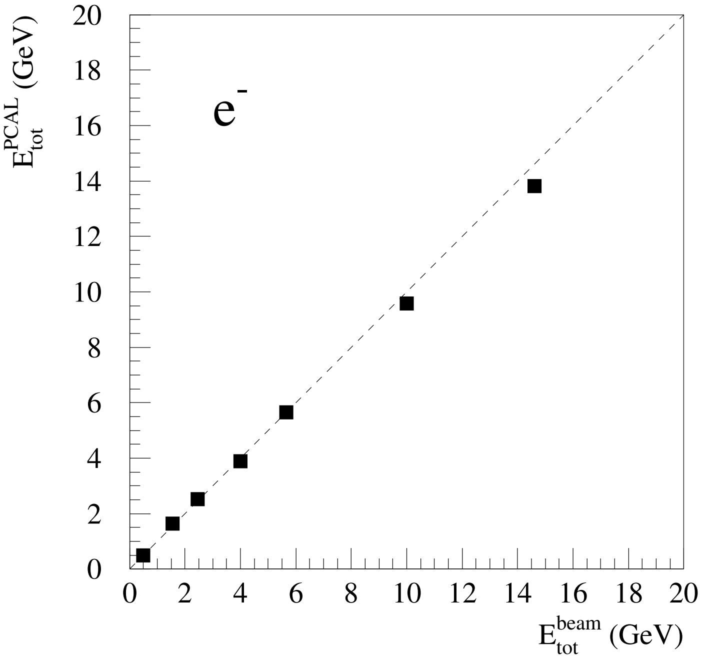

Figure A.2: The Monte - Carlo results of total energy deposition for e^- at the different beam energies.

lower than that of the incident one. We understand that this effect does not have the same origin as electrons, since hadronic showers are rather insensitive to the plate to plate fluctuation of EM modules. This effect can be caused by shower leakage. The lateral and longitudinal shower dimensions become larger for higher beam energies so that we can not avoid a significant amount of energy leaking out from the calorimeter. Fig. A.4 is the total energy from the calorimeter as a function of the kinetic energy of proton projectile. In the case of a proton projectile, we expect to acquire only the kinetic part of the beam energy. But we always get more than the kinetic energy of the projectile, considering shower leakage at high energies, in both experiment and simulation. The fractional energy deposition of each module for hadrons at several beam momenta are summarized in Table A.2 for pions, and A.3 for protons with available experimental data.

Another important term of calorimeter response is the e/π ratio. Fig. A.5 shows calculated e/π ratio's for two different towers, (5,16) and (4,4). For tower (5,16), which is an almost perfect tower, e/π was greater than one even for energies above 10 GeV. We deduced shower leakage as the major reason of this high e/π. In order to involve more shower components for hadrons, we tried tower (4,4). But we did not observe much difference between the two towers. For low energy particles e/π is in general less than one, because the probability that charged hadrons lose their energy by binding energy loss increases rapidly. But we could not see this effect from the simulation. At 0.5 GeV this ratio is 1 for (5,16) and 1.04 for (4,4).

p_{beam}	Module	Experiment	Present
	EM1	0.443 ± 0.010	0.427 ± 0.023
1.56	EM2	0.330 ± 0.008	0.277 ± 0.016
	HD1	0.619 ± 0.014	0.500 ± 0.026
	HD2	0.018 ± 0.001	0.052 ± 0.008
	total	1.360 ± 0.013	1.256 ± 0.033
	EM1	0.532 ± 0.026	0.536 ± 0.030
2.46	EM2	0.421 ± 0.017	0.480 ± 0.025
	HD1	1.066 ± 0.037	0.876 ± 0.038
	HD2	0.206 ± 0.019	0.119 ± 0.014
	total	2.186 ± 0.032	2.011 ± 0.043
	EM1		0.790 ± 0.046
4.00	EM2		0.753 ± 0.040
	HD1		1.373 ± 0.050
	HD2		0.432 ± 0.033
	total	4.420	3.348 ± 0.057
	EM1	0.858 ± 0.012	1.072 ± 0.061
5.65	EM2	1.011 ± 0.012	1.105 ± 0.053
	HD1	2.488 ± 0.019	2.356 ± 0.079
	HD2	0.694 ± 0.012	0.642 ± 0.047
	total	4.978 ± 0.013	5.175 ± 0.070
	EM1		1.277 ± 0.056
10.0	EM2		1.796 ± 0.079
	HD1		4.054 ± 0.119
	HD2		1.294 ± 0.085
	total	10.510	8.421 ± 0.090
	EM1		1.552 ± 0.106
14.6	EM2		2.087 ± 0.110
	HD1		6.530 ± 0.170
	HD2		2.128 ± 0.128
	total	14.05	12.297 ± 0.122

Table A.2: The energy deposition of each module for π^- at the different beam momenta. All units are in GeV.

p_{beam}	Module	Experiment	Present
4.00 ($E_{kin} = 3.17$)	EM1		0.858 ± 0.053
	EM2		0.659 ± 0.040
	HD1		1.521 ± 0.059
	HD2		0.478 ± 0.040
	total	3.396	3.516 ± 0.072
10.0 ($E_{kin} = 9.11$)	EM1		1.065 ± 0.067
	EM2		1.476 ± 0.070
	HD1		4.472 ± 0.109
	HD2		1.881 ± 0.093
	total	9.328	8.844 ± 0.106
14.6 ($E_{kin} = 13.69$)	EM1		1.391 ± 0.094
	EM2		2.139 ± 0.100
	HD1		6.229 ± 0.159
	HD2		2.780 ± 0.124
	total	12.640	12.539 ± 0.146

Table A.3: The energy deposition of each module for proton at different beam momenta. All units are in GeV.

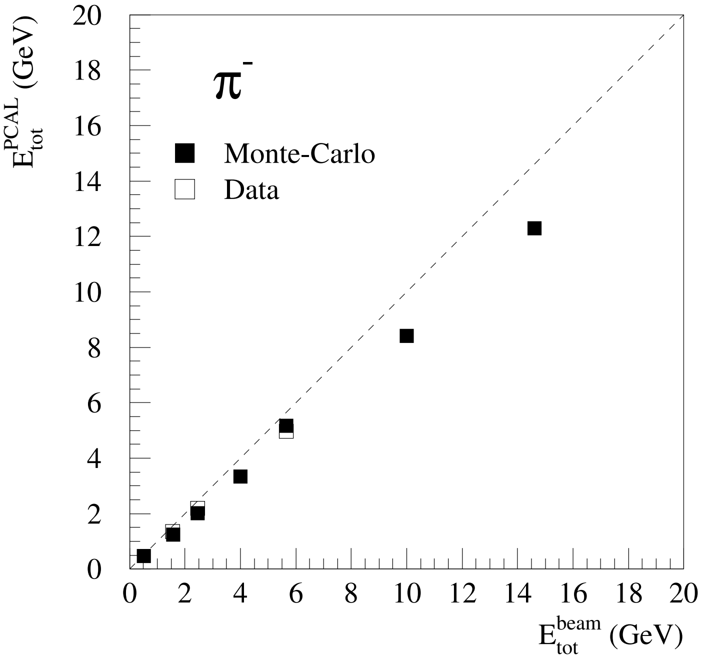

Figure A.3: The Monte - Carlo results of total energy deposition for π^- at the different beam energies.

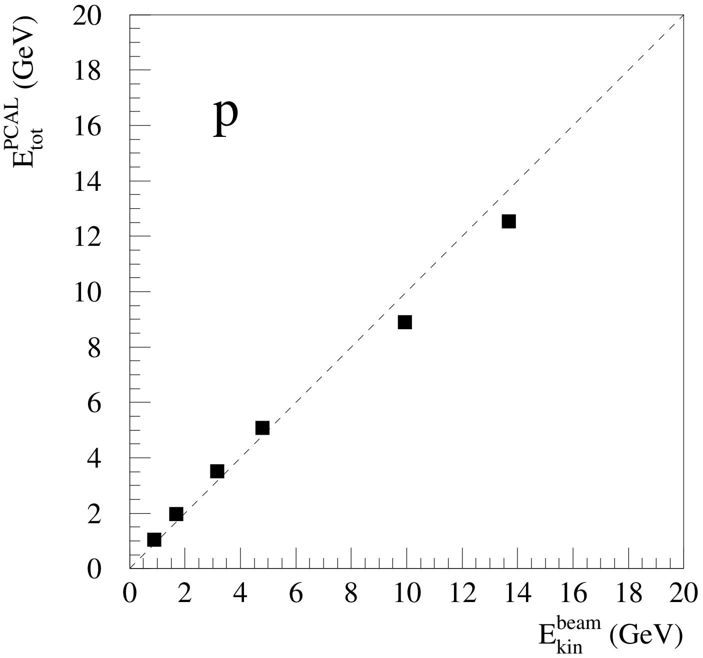

Figure A.4: The Monte - Carlo results of total energy deposition for protons at the different beam energies.

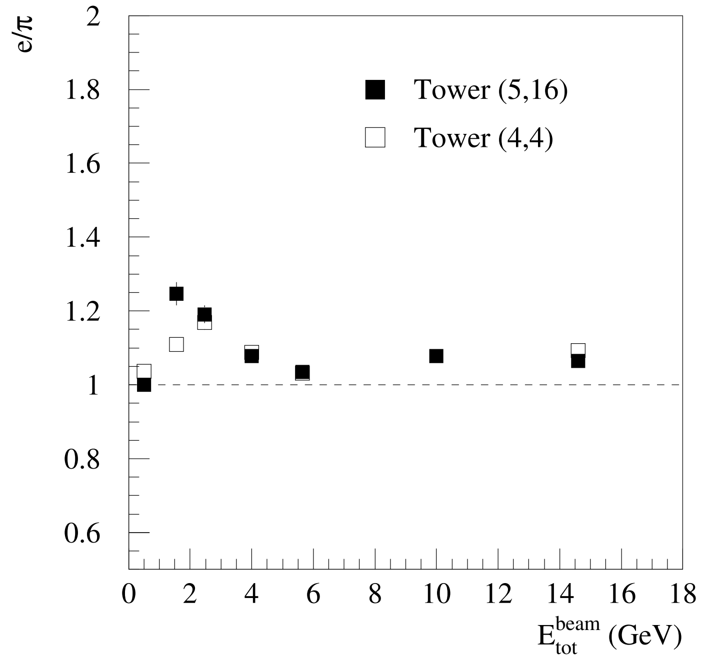

Figure A.5: The e/π at several beam energies on towers (5,16) and (4,4).

p^e_{beam} (GeV)	Without	With	Data
1.56		0.25	0.25
2.46		0.24	0.25
5.65	0.20	0.24	0.25
$p^\pi_{beam}(GeV)$			
1.56		0.56	0.46
2.46		0.57	0.43
5.65	0.55	0.56	0.58

Table A.4: Energy Resolution (C) for e^- and π^- at several beam momenta. "Without" means without and "With" means with considering the plate to plate fluctuation of EM1 and EM2.

A.2.3 Energy Resolution

Energy resolution is the most important issue of calorimeter performance. The energy resolution of PCAL was investigated by Monte-Carlo simulation. We define the energy resolution, C, as

$$\frac{\sigma}{E^{beam}_{tot}} = \frac{C}{\sqrt{E^{MC}_{tot}}} \tag{A.1}$$

where σ is the root mean squre (RMS) of the energy spectrum, E^{beam}_{tot} is the total beam energy and E^{MC}_{tot} is the total energy measured by simulation. With a 500 event basis we reproduced almost the same energy resolution as the experiment for e^- projectile. Considering the plate to plate response of EM1 and EM2 only, we saw that the energy resolution for electrons increases from 20% to 24% which is very close to the data, 25%. For pions, the simulation returned 56% energy resolution for $\pi^\pm$, which is close to the 58 % for 5.65 GeV π^-. Table A.4 shows the summary of the energy resolution studies.

A.2.4 Optimization of Tracking Threshold

We tested our GEANT program based on event by event tracking, with several tracking thresholds, to look at how much energy loss can be caused by increasing the tracking threshold. For electrons with several beam energies we increased tracking thresholds of electrmagnetic shower components from 20 KeV to 6 MeV. As we increased it from 20 KeV to 1 MeV, we did not lose any fraction of the total energy deposition in PCAL. As a result of increasing the threshold, we could finish the calculation using only 68 % of CPU time. However as the tracking threshold became higher than 1 MeV, we started to lose some total energy deposited in PCAL. For example, we lost 2 % for 5 MeV and 6 % for 6 MeV tracking threshold for 5.65 GeV e^-, although we could complete the calculations with 39 % and 34 % of CPU time. Increasing the tracking thresholds of the hadronic shower components from 50 KeV to 5 MeV for 5.65 GeV π^-, we could finish the calculation using only 46 % of CPU time without missing any total energy deposition. But for a 7 MeV threshold, we started to lose about 6 % of the total energy.

Consequently, the present tracking thresholds of electromagnetic and hadronic shower components are 1 MeV and 5 MeV respectively. As a reference, the default values for them in GEANT 3.13 are 1 MeV and 10 MeV.

A.3 Angle Dependence of Shower Leakage

From the configuration of PCAL we can imagine that some shower components originated from electrons, hadrons and baryons resulting from heavy ion collision escape the calorimeter without depositing their whole energy, particularly for large polar angles. We looked at those effects for several shower components at the different beam energies and at different θ's. Because the real experiment can not be done to answer this question, simulation results will be the only solutions for comparison with PROPHET.

A.3.1 Electromagnetic Showers

Fig. A.6 shows the total energy deposition of electrons as a function of incident angle for three different beam momenta. In this figure, the dashed line with filled squares represents the calculation along the x axis and the dotted line with filled triangles does the same along the y axis. The PROPHET result along the x axis is represented by the dashed dotted line with open squares. Since the size of electromagnetic showers is small, the total energy deposition of electrons is very sensitive to the plate to plate fluctuation. Moreover the fluctuation of EM1 dominantly effects the energy deposition. According to Fig. A.1, total energy deposition along the x axis can be reduced by more than 30 % due to plate to plate fluctuation. Therefore we can hardly distinguish shower leakage from plate to plate fluctuation for large θ towers. On the other hand, towers along the y axis look more stable. We see shower leakage at the outmost tower very clearly. As we increase the beam momenta from 2.46 GeV to 10 GeV, the fraction of energy leaking out of the calorimeter increases from about 13 to 16 % in the outmost tower.

We also calculated the transverse energies at different θ's and at the different beam momenta. The true transverse energy of incident particle is defined by

$$E_t^{true} = E_{tot}^{beam} \sin\theta_{Inc} \tag{A.2}$$

where E_{tot}^{beam} is total beam energy and θ_{Inc} is the polar angle of the projectile, while the transverse energy calculated by Monte - Carlo simulation is defined by

$$E_t^{MC} = \sum_{i=1}^{512} E_i^{dep} \sin\theta_i \tag{A.3}$$

where i is tower index from 1 to 512, E_i^{dep} is the energy deposited in the ith tower and θ_i is the corresponding angle of the ith tower (θ_i is polar angle between center line and the line connecting target and the center of volume for the ith tower). The true E_t and measured E_t by Monte - Carlo simulation of electrons at several different momenta are shown in Fig. A.7. The solid line represents true transverse energy. The remaining notations are exactly the same as before. At the very small angles the transverse energy by GEANT and the GHEISHA simulation exceeds the true one because of the lateral spread of showers. Although projectile was incident on the calorimeter normally, the detectors will measure some transverse energy. However it looks as if PROPHET does not produce this phenomenon.

Fig. A.8 show the correction factors for transverse energy, which is the ratio, α, of the mean transverse energy measured by Monte - Carlo to the true transverse energy from Fig. A.7;

$$\alpha \equiv \frac{\langle E_t^{MC} \rangle}{E_t^{true}}. \tag{A.4}$$

The α is expected to be one for most of the incident angles, except for small angles lower than 6° and the outmost tower, if the calorimeter is perfect.

A.3.2 Hadronic Showers

We need a more complicated interpretation of the shower leakage for hadrons, because the shower size of hadrons in the calorimeter is much bigger than that of electrons. Fig. A.9 shows the total energy depositions of π^- at five different beam momenta as a function of incident angle. Shower leakage starts from inner towers compared to the electron beam. In most of the θ range, PROPHET gave more total energy deposition than GHEISHA for 2.46 GeV. As the beam momentum increased from 5.65 GeV to 14.6 GeV, the difference of total energy deposition became less and they were almost identical for 14.6 GeV in the mid θ range. However the PROPHET results were always less than the GHEISHA results for very small θ's.

Using the same definitions of E_t^{true} and E_t^{MC}, we calculated the true and measured transverse energies for pions at different θ's (see Fig. A.10). We saw again the phenomenon that measured E_t by simulation exceeds E_t^{true} for small angles similar to electrons. The ratio, α, for π^- is in Fig. A.11.

We calculated the same physical quantities for protons. For protons we anticipated that we would get only kinetic energy instead of total energy. The angle dependence of total energy deposition for protons is shown in Fig. A.4. We know that the total energy deposition is larger than only the kinetic part from the Fig. A.4. The difference in total energy deposition between

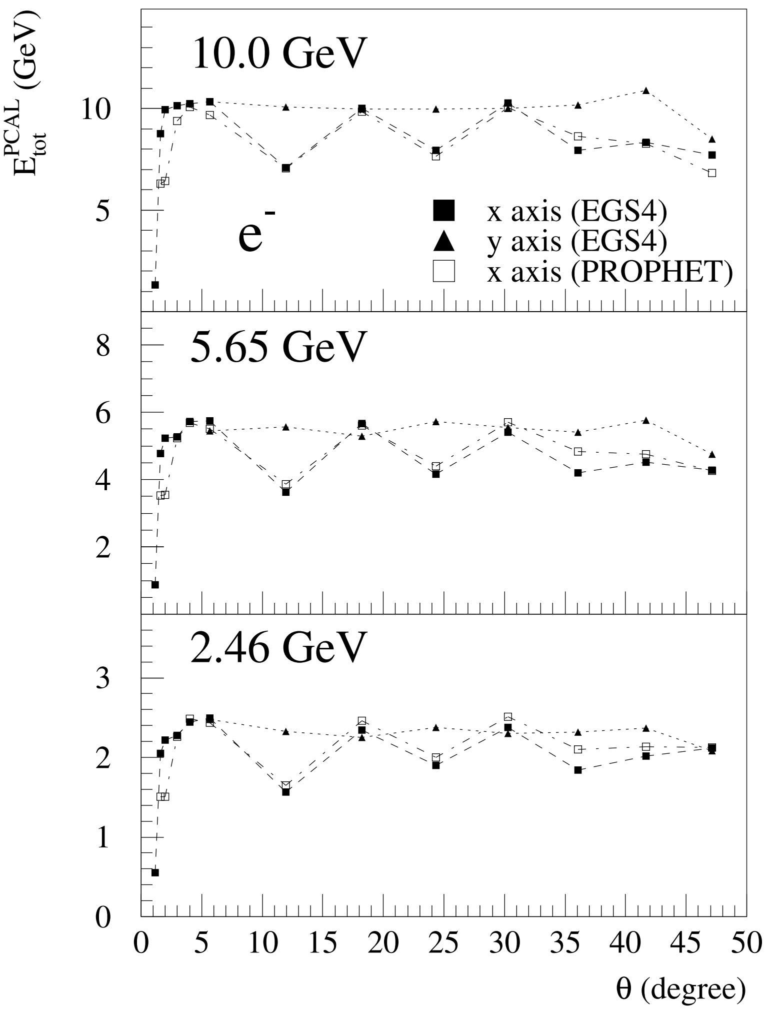

Figure A.6: The incident angle dependence of total energy deposition for e^-. The dashed line with filled square is along x axis and the dot line with filled triangle is along y axis by GHEISHA simulation. The dashed dot line with open square is along x axis by PROPHET simulation.

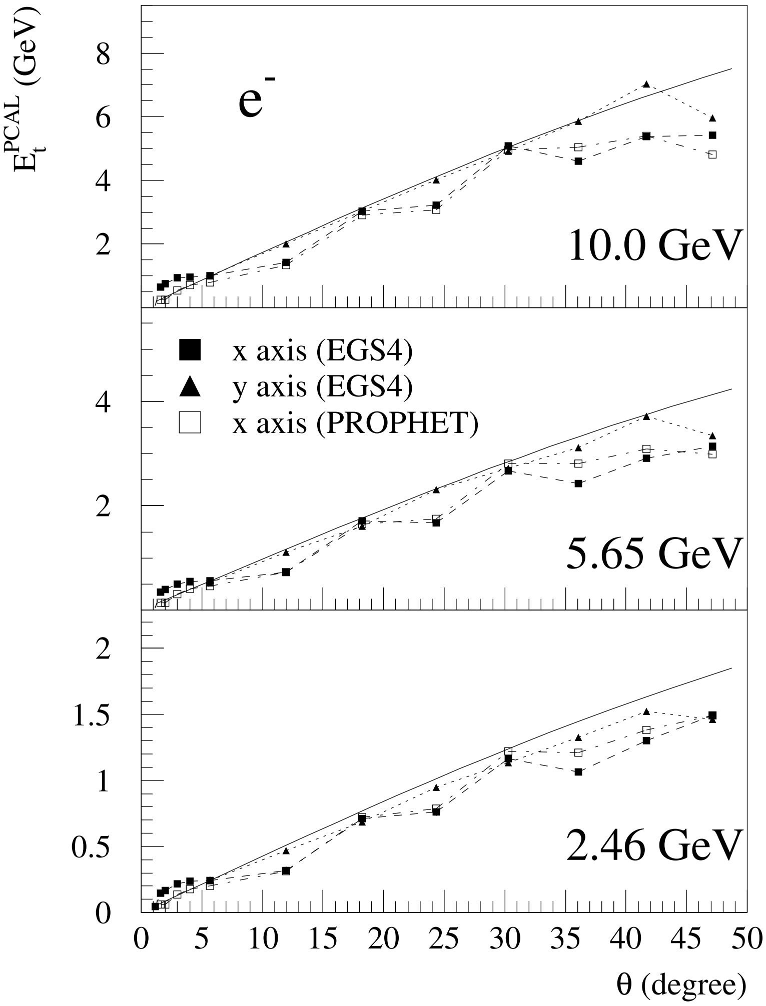

Figure A.7: The incident angle dependence of transverse energy for e^-. The solid line represents the true transverse energy.

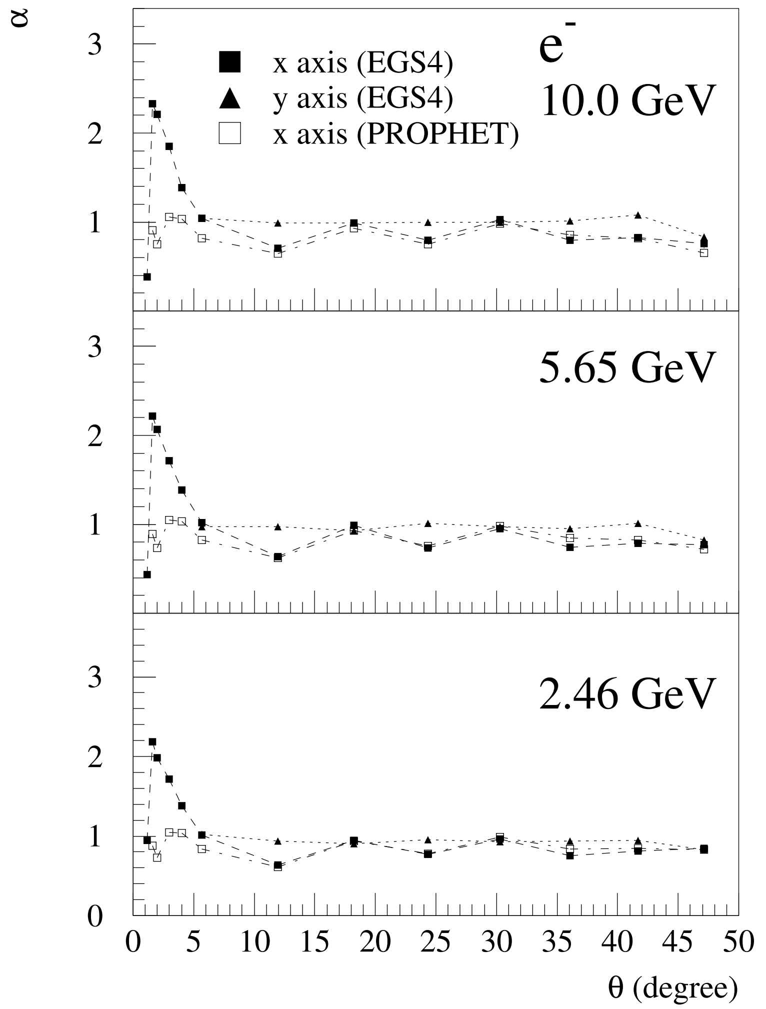

Figure A.8: The incident angle dependence of α for e^-.

GHEISHA and PROPHET is much larger than that for pions. For the same reason the difference between E_t^{MC} by GHEISHA and PROPHET was much larger than that of pions (Fig. A.13). Here we used the previous definitions except that E_{tot}^{beam} is replaced by the kinetic energy of proton. Fig. A.14 show α for proton.

A.4 Energy Conservation

We checked the energy conservation using the physics event generator, HIJET with rescattering [59]. We first defined several extra volumes surrounding the target and PCAL, in order to check that we might obtain the whole kinetic energy of projectile nucleus. For 14.6 A GeV ^{28}Si beam, the total kinetic energy of each projectile nucleus is 383.38 GeV. Some results of total energy for Pb target for various centralities are shown in Table A.5, where E_{tot}^{PCAL} is total energy from the PCAL by simulation, E_{leak}^{PCAL} is total energy leakage from PCAL through the side walls as well as back wall, E^{hole} is the energy emerging through the hole of PCAL without being obstructed by the calorimeter, E^{other} is the energy found in the remaining region and $E_{tot}^{SUM} = E_{tot}^{PCAL} + E_{leak}^{PCAL} + E^{hole} + E^{other}$. E_{tot}^{SUM} was close to the value that it should be for very central and very peripheral collisions. But in the case of mid cetrality, the total sum of the energy was higher than the kinetic energy of the projectile nucleus.

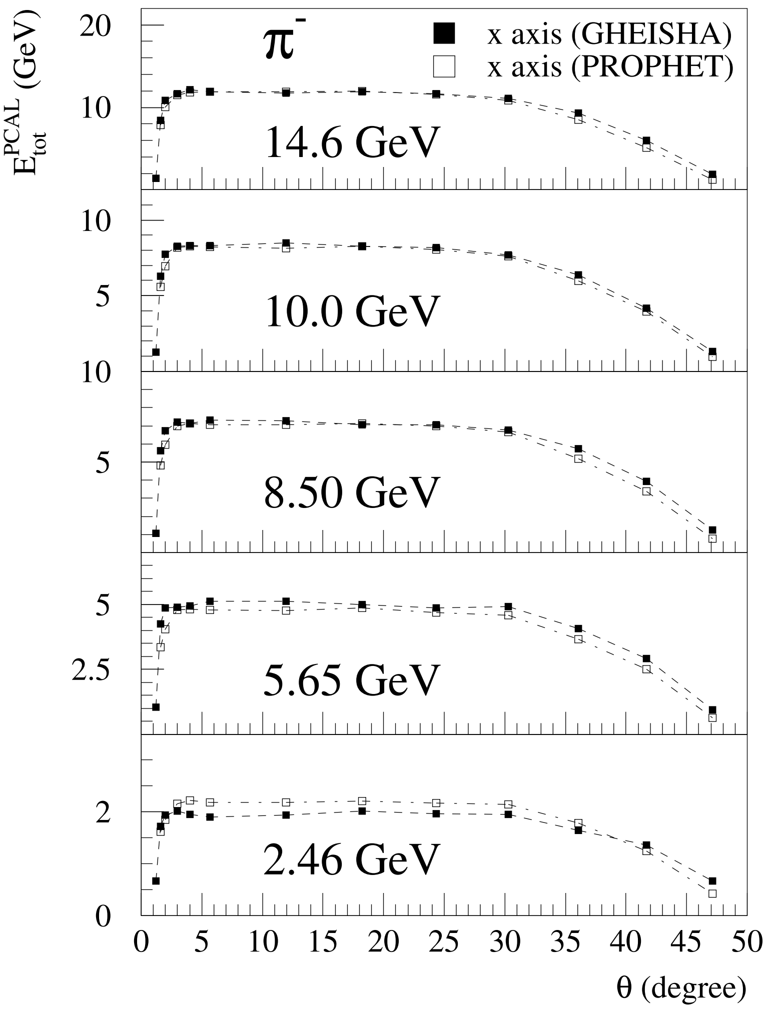

Figure A.9: The incident angle dependence of total energy deposition for π^-.

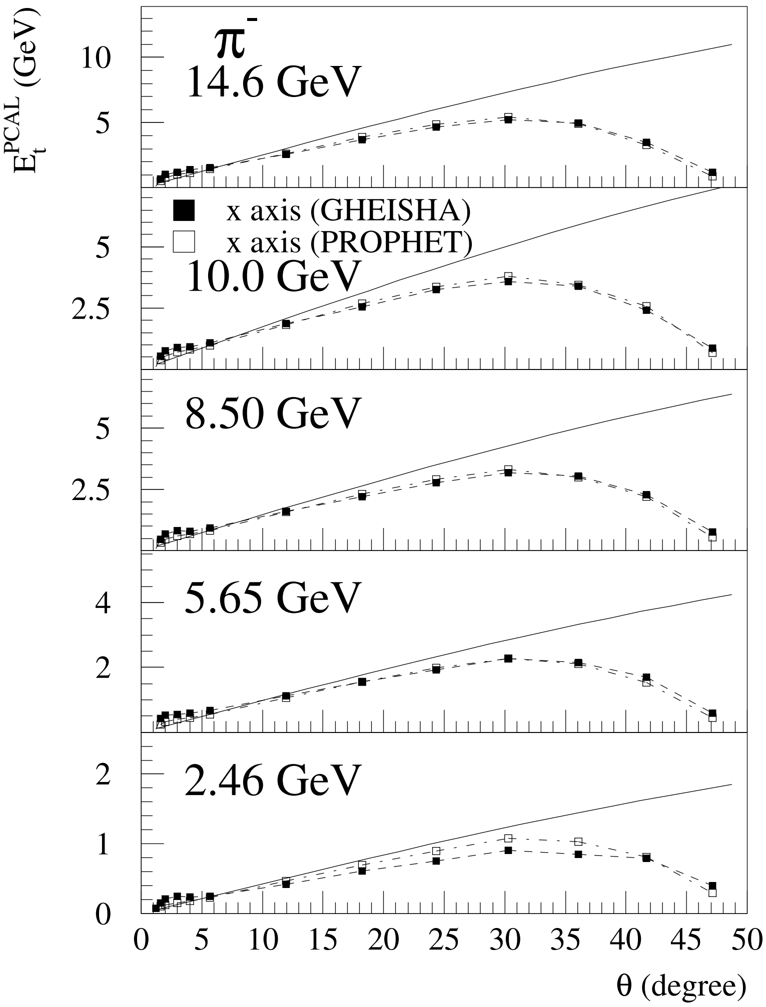

Figure A.10: The incident angle dependence of transverse energy for π^-.

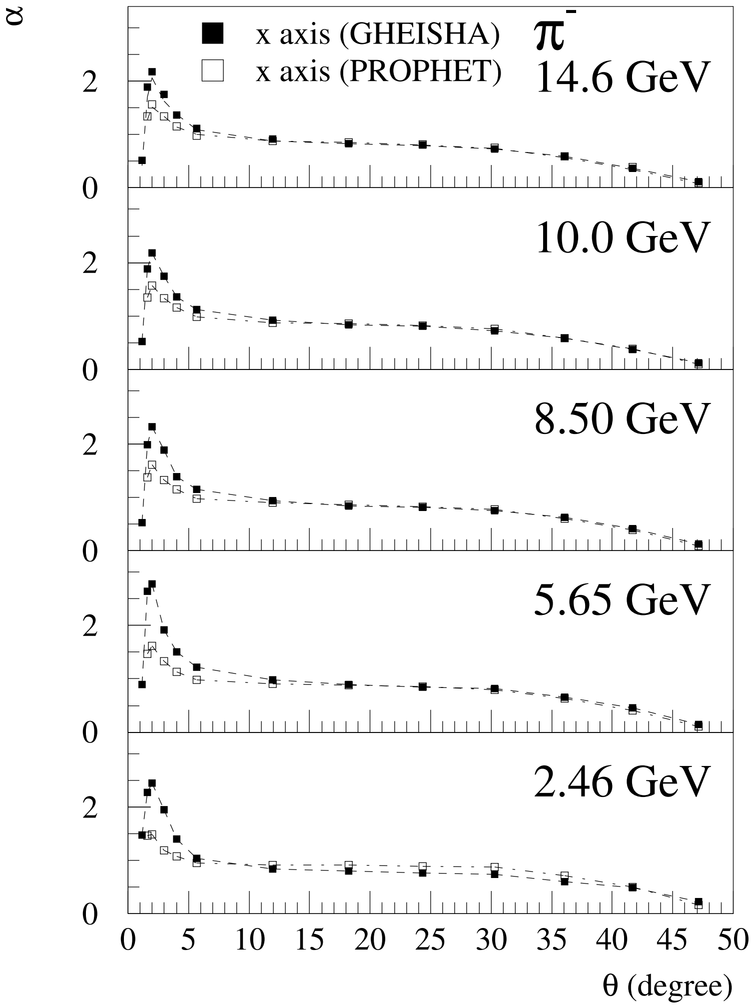

Figure A.11: The incident angle dependence of α for π^-.

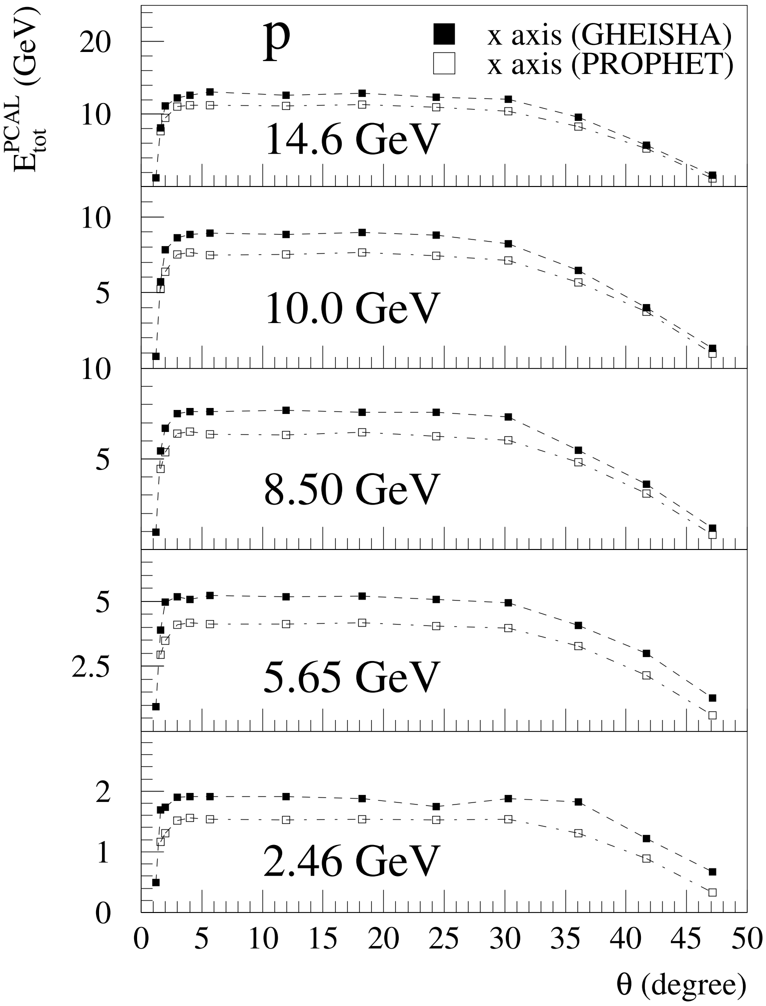

Figure A.12: The incident angle dependence of total energy deposition for protons.

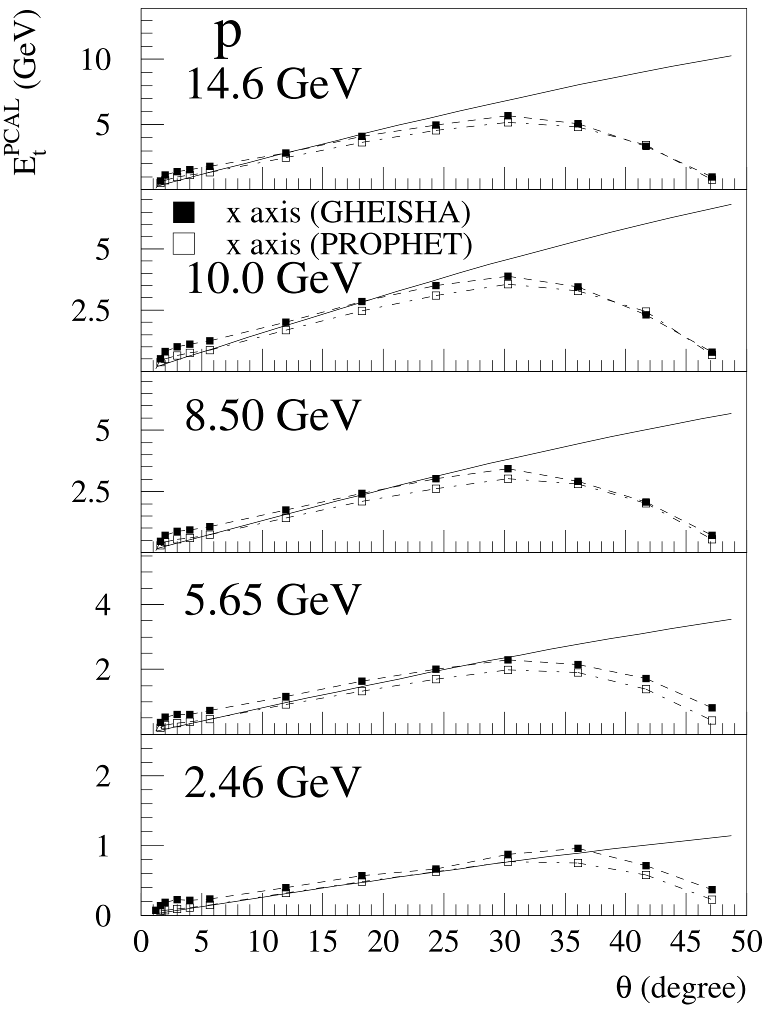

Figure A.13: The incident angle dependence of transverse energy for protons.

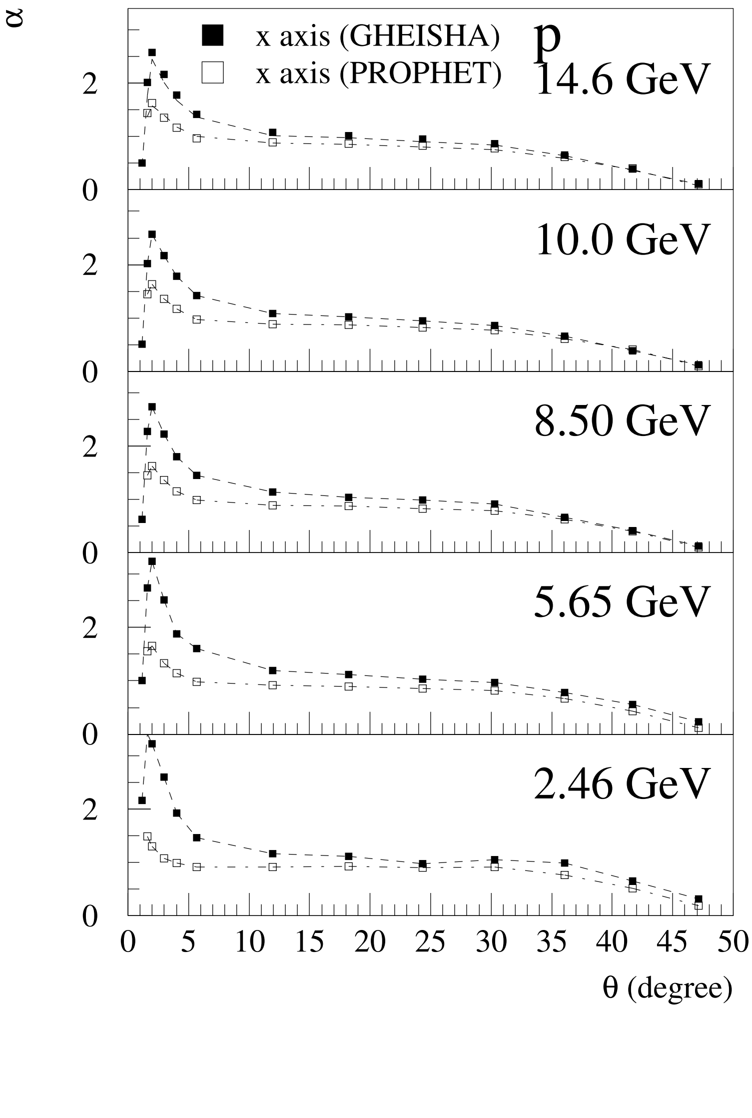

Figure A.14: The incident angle dependence of α for protons.

E_{tot}^{PCAL}	E_{leak}^{PCAL}	E^{hole}	E^{other}	E_{tot}^{SUM}
315.7203	27.4465	2.3970	39.8470	385.4108
315.7045	22.3540	1.3250	44.9645	384.3480
268.0420	74.2375	44.5870	12.1340	399.0005
216.4789	28.8275	119.2980	17.1250	381.7294
205.3446	46.2865	119.7980	12.9520	384.3811
176.1659	55.6105	146.3020	12.1690	390.2474

Table A.5: A few examples of total energy for ^{28}Si + Pb collisions by HIJET event generator with rescattering. The beam momentum of ^{28}Si was 14.6 A GeV. The top row is more central and the bottom row is more peripheral collision. All units are in GeV.

A.5 Conclusion

All the geometrical details of PCAL are in the GEANT frame. The GEOM package simulates the shower development in the calorimeter reasonably. This was confirmed by comparing our simulation results based on EGS4 and GHEISHA with SEB experimental data. The signal linearities for electron and pion projectiles look reasonable. However for proton projectiles we always obtained energy deposition more than the kinetic part of incident proton in our energy range of interest. The e/π was greater than 1 above 5 GeV total beam energies. And we could not get e/π less than one for energy below 1 GeV.

The angle dependence of shower leakage effects was studied. For electromagnetic showers it was hard to see shower leakage at the outer tower, because the plate to plate fluctuation was too big along the x axis. But towers along the y axis were more stable so that shower leakage at the outmost tower was clear. The shower leakage for hadrons starts at smaller θ; from the 5th or 6th tower in our energy range. The simulated transverse energy exceeded true transverse energy at small incident angles for both electromagnetic and hadronic showers. The angle dependences of total and transverse energy depositions by GHEISHA well agree in shape with those of PROPHET except at angles below 10°.

Appendix B

Thermal Model

B.1 Introduction

Presently there are quite convincing experimental data and interpretation from the E814 collaboration concerning thermal equlibration in relativistic heavy ion collisions at the AGS [16, 17, 35]. All of the measured particle yields at AGS energy are reasonably reproduced, using appropriate baryonic and strangeness chemical potentials and temperature. We can determine the particle ratios including all resonances, once assuming the equilibration of the system. The population probability of resonances enables us to calculate the resonance contribution to the particle spectra.

In this appendix, we estimate the population of resonances, which may affect the pion and kaon spectra, based on the restrictions in the experimental pattern recognition software. The rapidity dependence and the relative behavior in p_t spectra of resonance decays are also presented.

B.2 Resonance Decay

B.2.1 Pion

There have been attempts to explain the low p_t enhancement of the pion spectra in 14.6 A GeV ^{28}Si + Pb collisions with the decay of $\Delta(1232)$ (just Δ hereafter) resonance in Refs. [16, 17, 35, 60]. Although the thermal model with Δ was effective to describe the overall shape, several resonances were included to provide a complete description due to resonance decay. The population probability was calculated by

$$\rho_i^0 \equiv \frac{R_i^{BR} \cdot g_i}{2\pi^2} \int \frac{p^2 dp}{exp((E_i - \mu_b B_i - \mu_S S_i)/T_B) \pm 1}, \tag{B.1}$$

where R_i^{BR} and g_i are the branching ratio and the spin - isospin degeneracy of particle i, E_i, B_i and S_i are its total energy in the local restframe, baryon number and strangeness, and μ_b and μ_S are the baryon and strangeness chemical potential. Here the positive sign in the denominator of the integrant is for fermions and negative sign is for bosons. We have used 0.54 and 0.135 GeV for μ_b and μ_S respectively[1], and 0.14 GeV for T_B following the Ref. [60]. The π^- densities from the decay of the presently considered resonances at freeze - out,

$$\rho_i = R_i^{\pi^-} \cdot \rho_i^0, \tag{B.2}$$

are summarized in Table B.1. Here $R_i^{\pi^-}$ is the probability to decay into π^-, which was estimated by applying the isospin Clebsch - Gordan coefficients to

[1]The strangeness chemical potential was determined to satisfy the strangeness balance [61].

Particle	$R_i^{\pi^-}$	R_i^{BR}(Channel)	$g_i(J \times I)$	$\rho_i(\mathrm{fm}^{-3})(\rho_i/\rho_\pi)$
π	0.33	—	3(1×3)	0.0324(1.000)
η	1.00	$0.24(\pi^+\pi^-\pi^0)$	1(1×1)	$1.29 \times 10^{-3}(0.0398)$
η'	1.00	$0.44(\pi^+\pi^-\eta)$	1(1×1)	$2.47 \times 10^{-4}(7.62 \times 10^{-3})$
ρ	0.67	$1.00(\pi\pi)$	9(3×3)	$9.87 \times 10^{-3}(0.305)$
ω	1.00	$0.89(\pi^+\pi^-\pi^0)$	3(3×1)	$4.08 \times 10^{-3}(0.126)$
Δ	0.33	$0.99(N\pi)$	16(4×4)	0.0274(0.844)
$\Lambda(1405)$	0.33	$1.00(\Sigma\pi)$	2(2×1)	$4.46 \times 10^{-4}(0.0138)$
$\Lambda(1520)$	0.33	$0.42(\Sigma\pi)$	4(4×1)	$1.87 \times 10^{-4}(5.78 \times 10^{-3})$
$\Sigma(1385)$	0.33	$0.88(\Lambda\pi)$	12(4×3)	$2.73 \times 10^{-3}(0.0842)$
$\Sigma(1385)$	0.33	$0.12(\Sigma\pi)$	12(4×3)	$3.73 \times 10^{-4}(0.0115)$
$\Xi(1530)$	0.33	$1.00(\Xi\pi)$	8(4×2)	$3.15 \times 10^{-4}(9.73 \times 10^{-3})$
$\Lambda(1116)$	1.00	$0.64(p\pi^-)$	2(2×1)	$5.09 \times 10^{-3}(0.157)$

Table B.1: The summary of the population probability of various resonances from the thermal model for π^-. J means spin and I means isospin degeneracy.

the possible decay channels (Table B.2).

We considered the mesonic and baryonic resonances only for masses less than 1.0 and 1.6 GeV respectively. For thermal pions, a gaussian distribution in rapidity centered at 1.25 (y_{cm}) with σ_y of 1.0 and rapidity dependent temperature measured by the E802 around mid rapidity [62] and by the E814 at forward rapidity [35] were used[2] (see Fig. B.1). For the mesonic resonances, the same rapidity and transverse momentum distributions as thermal pions were used, while the rapidity distribution from RQMD [54] with the E814 proton temperature was used for Δ and other baryonic resonances [14, 15, 63]. I have excluded the low lying states of Λ, Σ and Ξ, since their decay lengths ($c\tau$)

[2]Even though the fit of the experimental p_t spectra may be affected by resonance decays as to be shown later, we just took the measured temperature parameters.

Decay Channel	$R_i^{\pi^-}$
$\rho^+ \to \pi^+ + \pi^0$ $\rho^0 \to \pi^+ + \pi^-$ $\rho^- \to \pi^- + \pi^0$	$\frac{1}{3} + \frac{1}{3} = \frac{2}{3}$
$\Delta^{++} \to p + \pi^+$ $\Delta^+ \to \frac{2}{3}(p + \pi^0) + \frac{1}{3}(n + \pi^+)$ $\Delta^0 \to \frac{1}{3}(p + \pi^-) + \frac{2}{3}(n + \pi^0)$ $\Delta^- \to n + \pi^-$	$\frac{1}{4} \times \frac{1}{3} + \frac{1}{4} = \frac{1}{3}$
$\Lambda(1405) \to \frac{1}{3}(\Sigma^+ + \pi^-) + \frac{1}{3}(\Sigma^0 + \pi^0) + \frac{1}{3}(\Sigma^- + \pi^+)$	$\frac{1}{3}$
$\Sigma^+(1385) \to \Lambda + \pi^+$ $\Sigma^0(1385) \to \Lambda + \pi^0$ $\Sigma^-(1385) \to \Lambda + \pi^-$	$\frac{1}{3}$
$\Sigma^+(1385) \to \frac{1}{2}(\Sigma^+ + \pi^0) + \frac{1}{2}(\Sigma^0 + \pi^+)$ $\Sigma^0(1385) \to \frac{1}{2}(\Sigma^+ + \pi^-) + \frac{1}{2}(\Sigma^- + \pi^+)$ $\Sigma^-(1385) \to \frac{1}{2}(\Sigma^0 + \pi^-) + \frac{1}{2}(\Sigma^- + \pi^0)$	$\frac{1}{3} \times \frac{1}{2} + \frac{1}{3} \times \frac{1}{2} = \frac{1}{3}$
$\Xi^0(1530) \to \frac{1}{3}(\Xi^0 + \pi^0) + \frac{2}{3}(\Xi^- + \pi^+)$ $\Xi^-(1530) \to \frac{2}{3}(\Xi^0 + \pi^-) + \frac{1}{3}(\Xi^- + \pi^0)$	$\frac{1}{2} \times \frac{2}{3} = \frac{1}{3}$

Table B.2: The branching ratio to π^-, $R_i^{\pi^-}$, from various decay channels.

are rather large, e.g., $c\tau_\Lambda$ = 7.89 cm, $c\tau_{\Sigma^{+(-)}}$ = 2.395 (4.434) cm and $c\tau_{\Xi^{0(-)}}$ = 8.69 (4.91) cm. The track recostruction software of E814 for the 1991 and 1992 runs requires that all identified particles are from the target[3].

The rapidity distribution of pions from baryonic (Δ) and mesonic (ρ) resonances are shown in Fig. B.2 with their primary inputs. The widening of the rapidity distribution of the daughter pion compared to the input is apparent. The rapidity dependence of the p_t spectra of two (Δ) and three (ω) body decay channels are shown in Fig. B.3. There we show that the temperature of the daughter pion is lower for higher rapidity. The Boltzmann temperatures of daughter pions are 25 and 49 MeV at y = 4.1 compared to 60 and 95 MeV at y = 1.5 for Δ and ω decays respectively for $m_t - m_\pi \geq$ 0.15 GeV. The total π^- spectra in the mid and forward rapidities are shown in Figs. B.4 and B.5 with the contributions from each decay processes. At mid rapidity the enhancement due to three body decay is expected near zero p_t, while the pions from two body decay behave in opposite direction. On the other hand, the low p_t enhancements from two and three body decays are very similar in forward rapidity. We can also expect the gradual flattening of the spectra at high p_t because of ρ decay, which has relatively larger decay momentum (358 MeV). The comparison of the model calculation with E814

[3]There are some probabilities for those relatively long lived resonances to be reconstructed correctly or wrongly, because of the tracking chamber resolutions. This effect needs to be studied in the future. However, the effect is small and we barely see the difference, although we include 100 % of thermal Λs in our model (the bottom raw of Table B.1.

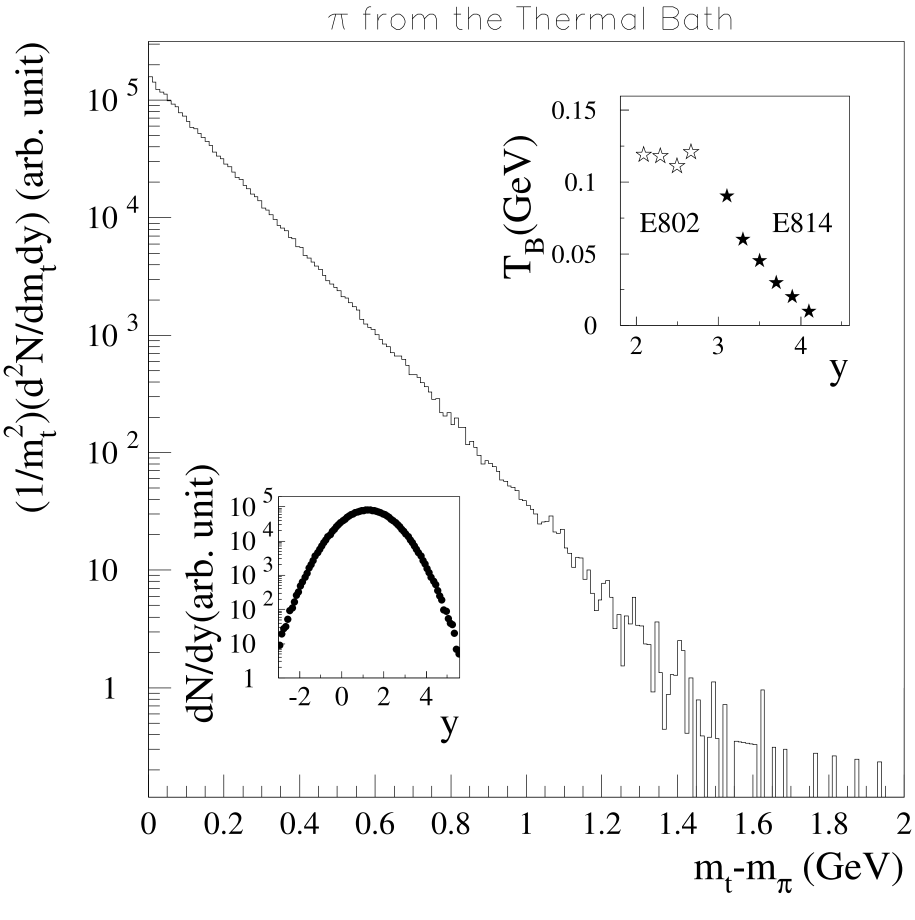

Figure B.1: The input spectrum of thermal pions. The inserts show the rapidity distribution and rapidity dependent Boltzmann temperature.

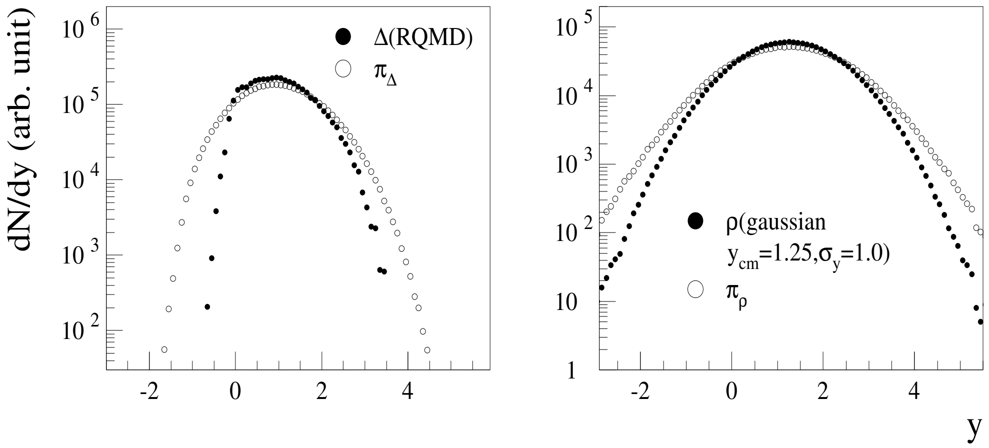

Figure B.2: The pion rapidity spectra from baryonic (Δ) and mesonic (ρ) resonances. Solid circle, resonances; open circle, daughter pions.

data is represented in Fig. B.6.

B.2.2 Kaon

The resonance contribution to kaon spectra from K^* and ϕ decays was also studied. The result of calculated population probability is summarized in Table B.3, where the decay branching ratio ($R_i^{K^\pm}$) of K^* was estimated by applying the isospin Clebsch - Gordan coefficients. We now have to consider different charges separately, since the chemical potentials ($\mu_b B_i - \mu_S S_i$) of positive and negative kaons are different. For the thermal spectra of K^+ and $K^{*+,0}$ (K^-, K^{*-}, $\overline{K^{*0}}$ and ϕ), a gaussian distribution in rapidity centered at 1.25 (1.6) with $\sigma_y = 1.0$ and the measured K^+ (K^-) temperature parameter by the

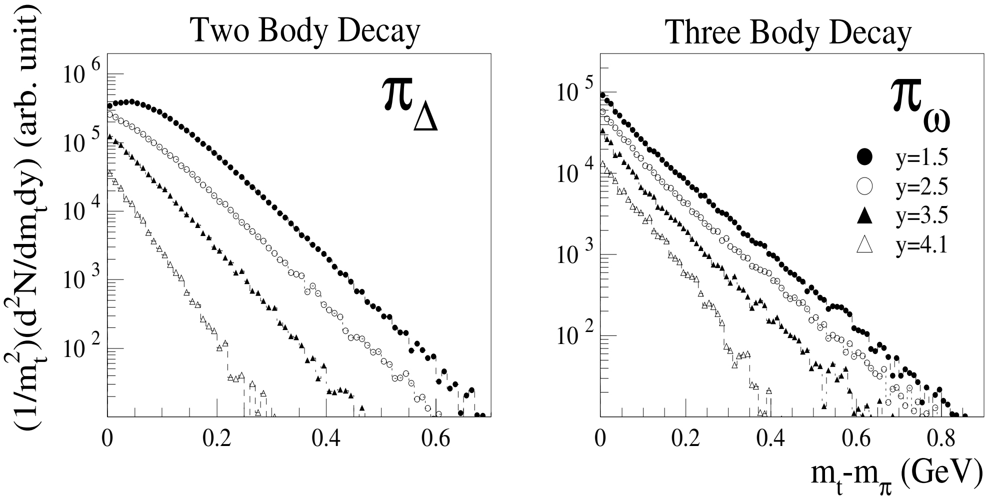

Figure B.3: The rapidity dependence of pion spectra from resonance decay.

E859 collaboration was used [55][4]. The rapidity dependence of the temperature parameter for the decay kaons are shown in Fig. B.7. The temperature of daughter kaon is not much different from that of primary resonances, and the rapidity dependence is weaker. The Boltzmann temperatures of kaons from K^{*+} decay are about 134 MeV and 101 MeV at $y = 1.6$ and 3.0 respectively. The sum of thermal and all decay contributions to K^+ spectra at $y = 2.3$, which are in E814 acceptance, are shown in Fig. B.8. The enhancement of kaons by resonance decays was too weak to explain the data at low p_t.

We also have studied the contribution of K^* to kaon p_t spectra in RQMD quantitatively. Table B.4 shows the result. The total number of $K^{*\pm,0}$ and $\overline{K^{*0}}$ are very high, because they include all theoretical excited states, which do not exist as free particles. To estimate the number of a specific resonance state, we

[4]The E859 data reasonably agree with the cascade models, RQMD [54] and ARC [64].

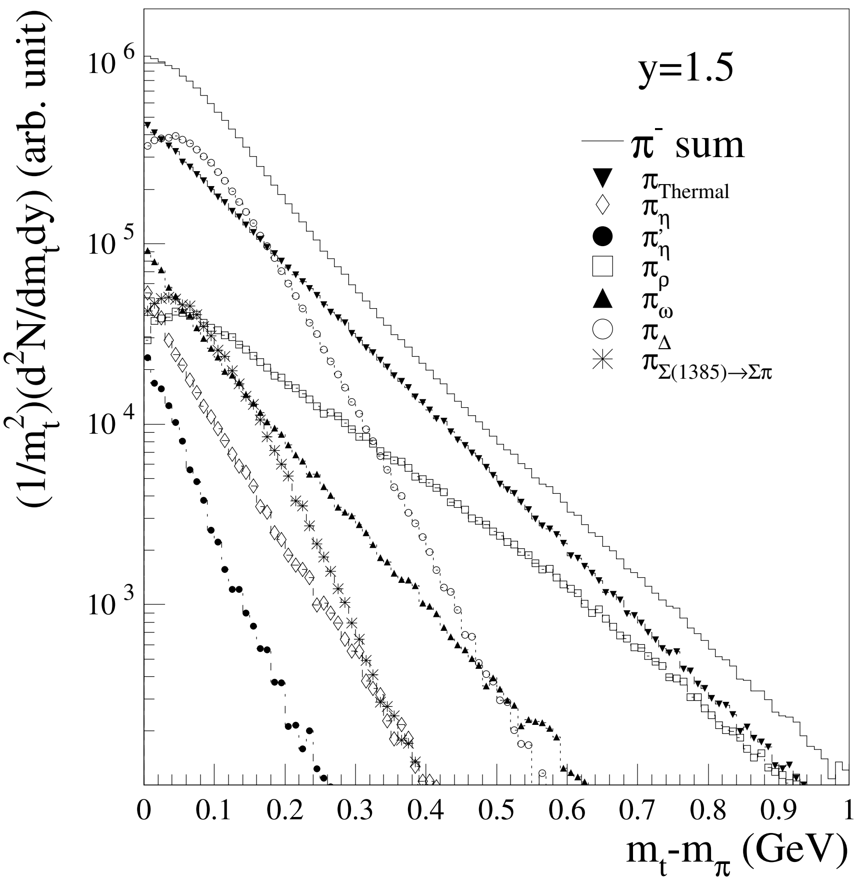

Figure B.4: The total π^- spectra near mid rapidity with resonances. The contributions by $\Lambda(1405)$, $\Lambda(1520)$, $\Sigma(1385) \rightarrow \Lambda\pi$ and $\Xi(1530)$ are very similar to that of η'.

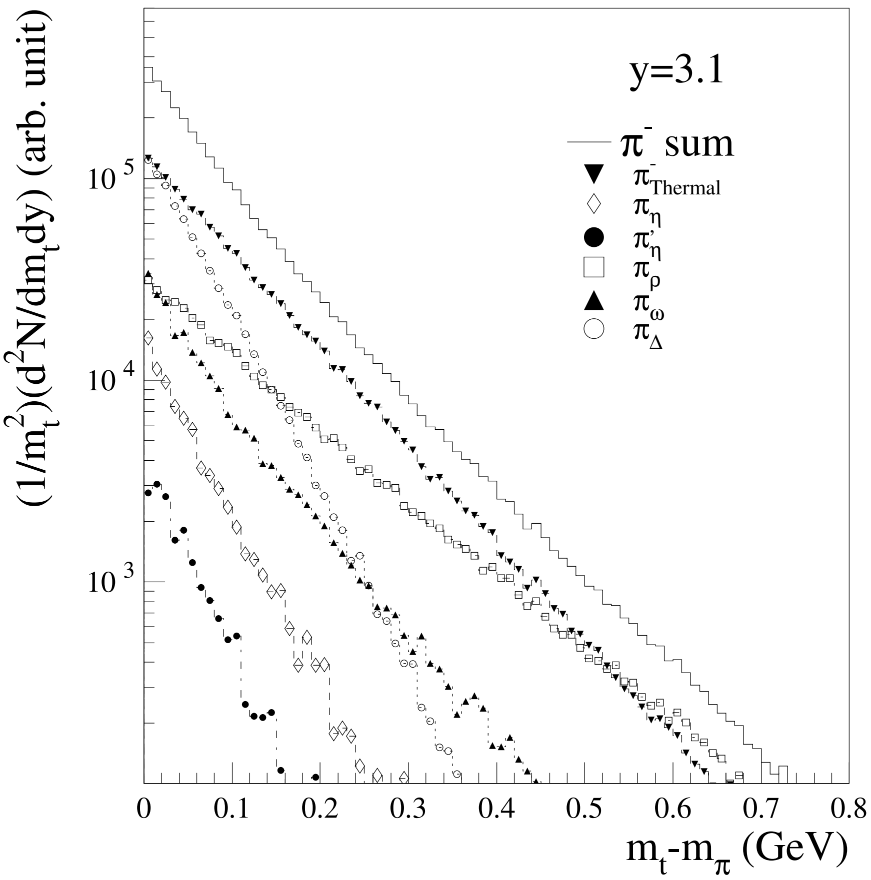

Figure B.5: The total π^- spectra at forward rapidity with resonances. The contribution by $\Sigma(1385) \rightarrow \Sigma\pi$ is very close to that of η and those by $\Lambda(1405)$, $\Lambda(1520)$, $\Sigma(1385) \rightarrow \Lambda\pi$ and $\Xi(1530)$ are very similar to that of η'.

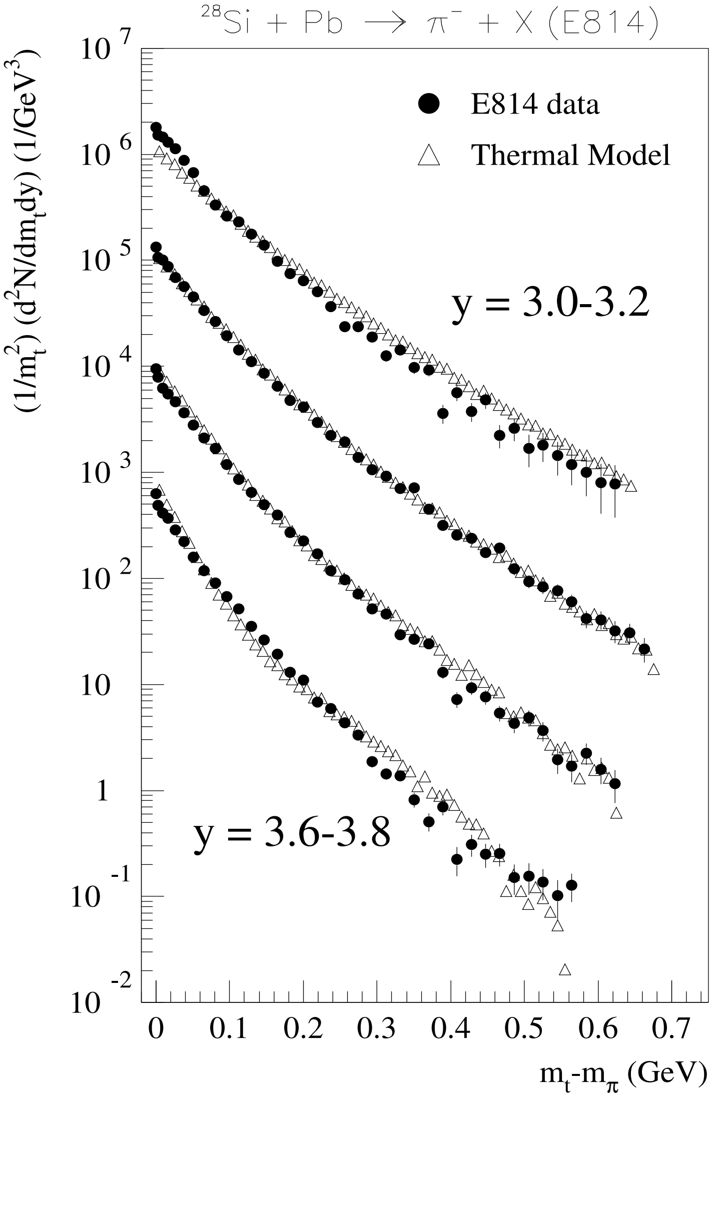

Figure B.6: The comparison of thermal model calculation of π^- for 14.6 A GeV ^{28}Si + Pb reactions with E814 data.

Particle	$R_i^{K^\pm}$(Ch.)	R_i^{BR}(Ch.)	$g_i(J)$	ρ_i(fm^{-3})	$\rho_i/\rho_{K^+}(\rho_{K^-})$
K^+	1	—	1	0.0189	1.000
K^-	1	—	1	2.70×10^{-3}	(1.000)
K^{*+}	$0.33(K^+\pi^0)$	$1.0(K\pi)$	3	2.16×10^{-3}	0.114
K^{*-}	$0.33(K^-\pi^0)$	$1.0(K\pi)$	3	3.14×10^{-4}	(0.116)
K^{*0}	$0.67(K^+\pi^-)$	$1.0(K\pi)$	3	4.23×10^{-3}	0.224
$\overline{K^{*0}}$	$0.67(K^-\pi^+)$	$1.0(K\pi)$	3	6.13×10^{-4}	(0.227)
ϕ	1.0	$0.49(K^+K^-)$	3	5.78×10^{-4}	0.0306(0.214)

Table B.3: The summary of the population probability of various resonances from the thermal model for $K^\pm$.

restricted the mass range, e.g., 892 $\pm$ 2 MeV for K^{*+}, etc. Considering only $K^*(892)$ resonance (or discarding all other higher mass resonances), RQMD has much less yield than a thermal model prediction. This may be related to the degree of chemical and thermal equilbration of the model. Thermal model calculation is compared with E814 data near zero p_t for ^{28}Si + Pb collisions in Fig. B.9. The model calculation has been plotted with the same bin size as E814 experimetal data. We could not reproduce the sharp increase of kaon spectra toward zero p_t with a pure thermal model.

B.2.3 Conclusion

The resonance decay contribution to the pion and kaon spectra for 14.6 A GeV ^{28}Si + Pb collisions at AGS energy was studied. We determined the population of the mesonic and baryonic resonances from the pure thermal model. Including the two and three body decays, the low p_t enhancement of pion specra was reasonably reproduced. On the other hand, the resonance

Ratio	Every Interaction	Last Interaction
$K^{*+}(\text{total})/K^+$	0.326	0.195
$K^{*+}(892)/K^+$	0.025	0.019
$K^{*0}(\text{total})/K^+$	0.718	0.476
$K^{*0}(892)/K^+$	0.058	0.046
$K^{*-}(\text{total})/K^-$	0.191	0.152
$K^{*-}(892)/K^-$	$0.011^\dagger$	$0.011^\dagger$
$\overline{K^{*0}}(\text{total})/K^-$	0.302	0.273
$\overline{K^{*0}}(892)/K^-$	$0.011^\dagger$	$0.011^\dagger$

Table B.4: The estimated K^* population from RQMD (†: only 1 event). The total numbers include all theoretical excited states, which do not exist as free particles.

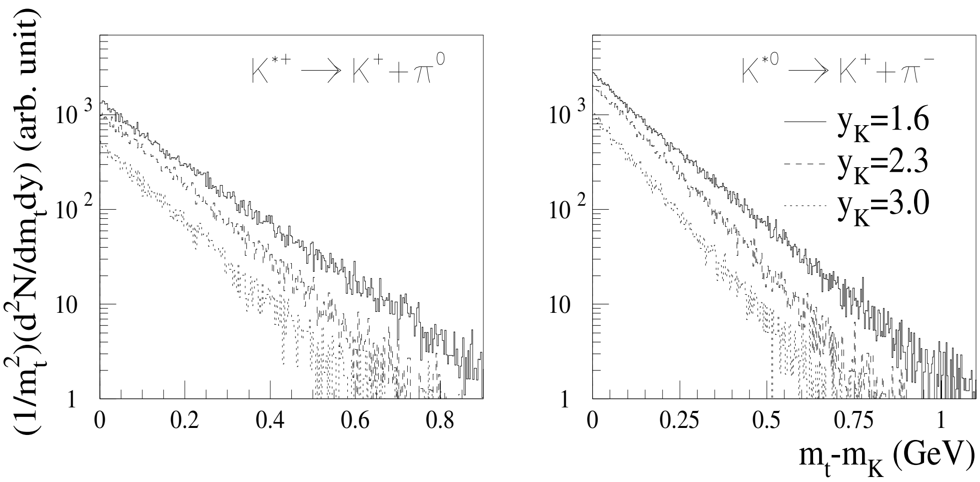

Figure B.7: The rapidity dependence of kaon spectra from resonance decay.

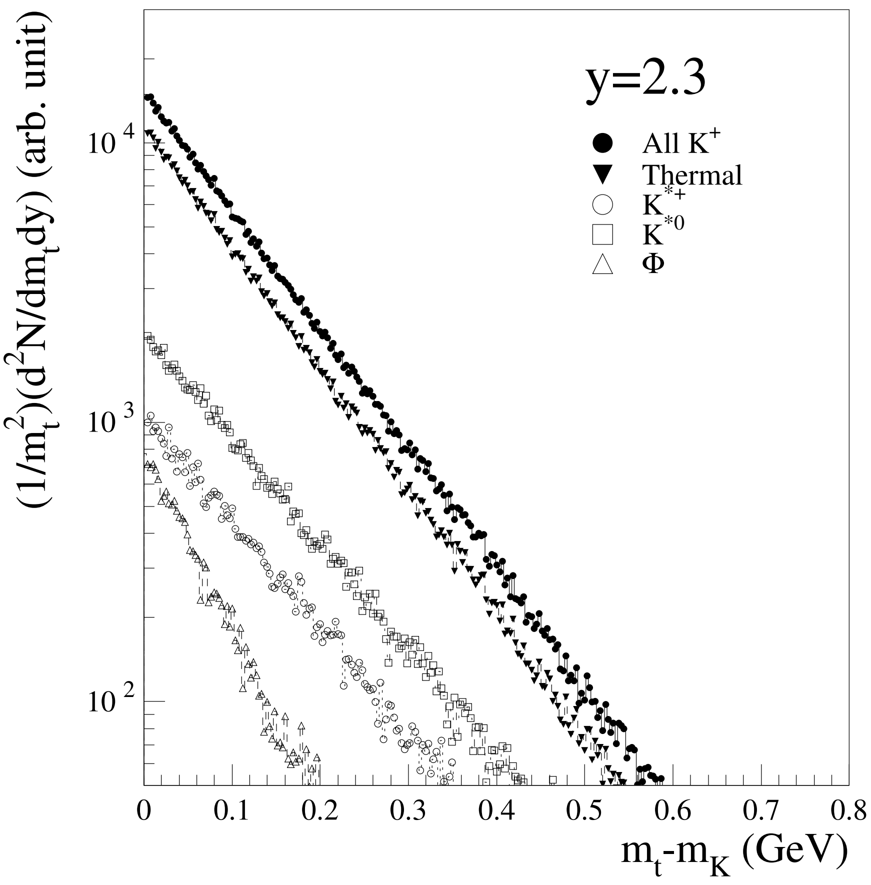

Figure B.8: The total K^+ spectrum at $y = 2.3$ with resonance decay contributions.

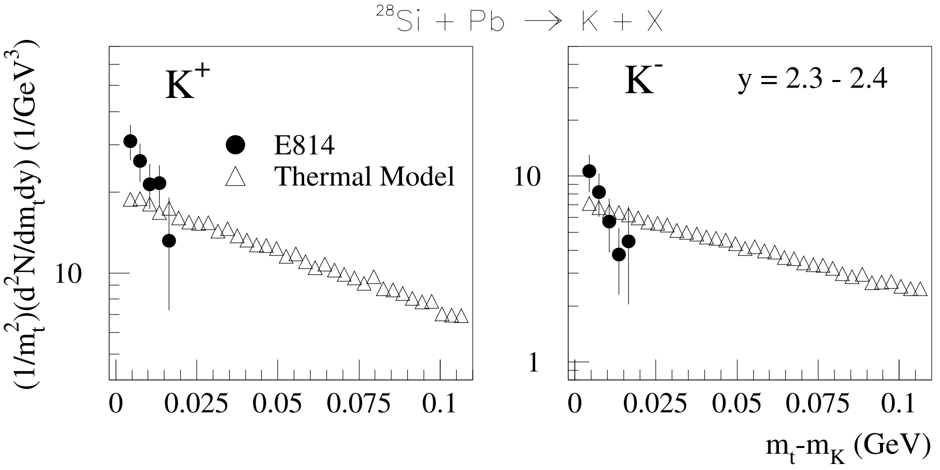

Figure B.9: The thermal model result of kaons with resonance decay compared with E814 data.

decay of K^* was rather unimportant so that it could not explain the cold kaon spectra from E814 at zero p_t at all. Although the kaons from ϕ decay can contribute at zero p_t, the population probability from the pure thermal model was too small to explain the data.

B.3 Adiabatic Expansion and Mass Reduction

A theoretical interpretation of cool temperatures for low p_t kaons employing very slow expansion velocity and mass drop in medium [65, 66] may shed some light on the understanding of the underlying physics.

A phase with high energy density but low pressure, due to the expected chiral symmetry restoration transition, would result in adiabatic slow expansion of the fireball at AGS energies. The cascade model simulating the behavior of an ideal gas and a relatively large expansion velocity essentially can not predict the feature of low p_t enhancement. On the other hand the mass reduction of particles due to the reduced repulsive vector potential is another ingredient of the model to reproduce experimental data at low p_t. Lattice calculations show the vector coupling constant (g_V with $V = \rho$ and ω, etc.), which is responsible for the low energy KN repulsive interaction, should be reduced above the critical temperature and thus the attractive potential due to the scalar field is dominant in our case. The mass drop in high density nuclear medium is reflected in the formula:

$$m_K(\rho) = m_K - U_0 \frac{\rho}{\rho_0} \tag{B.3}$$

where U_0 is the depth of attractive potential.

According to the above model, the slope at low transverse mass strongly depends on the expansion time, or expansion velocity, *i.e.*, the longer the expansion time the smaller the slope parameter as expected by the adiabatic expansion. However the depth of the potential hardly effects the slope parameter at low p_t, but rather controls the amount of soft particles, or the turning point of spectrum.

Figure B.10 shows the comparison of model calculation of K^+ production with E814 data for ^{28}Si + Pb collisions, where the calculation used the input parameters as R (radius of the fireball) = 3.5 fm, β_e (expansion velocity) = 0.15 and U_0 = 50 MeV. The model could reproduce the experimental feature

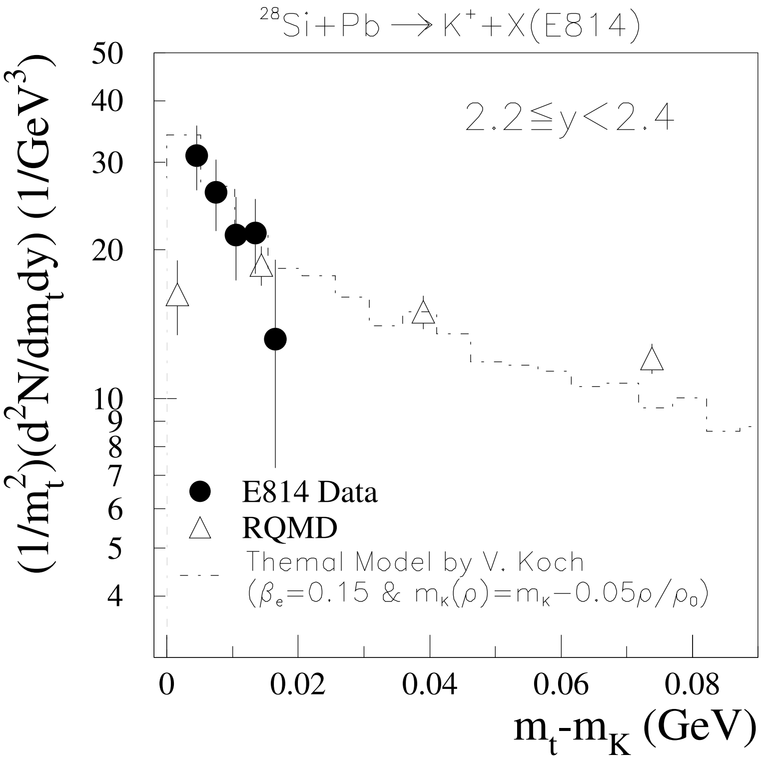

Figure B.10: The thermal model calculation (^{28}Si + Au), including slow expansion and mass drop, is compared to E814 ^{28}Si + Pb data at low p_t.

of low p_t enhancement.